ABSTRACT

Title of dissertation: RADIATIVE B MESON DECAY AS A PROBE OF PHYSICS BEYOND THE STANDARD MODEL: Time-dependent CP violation in $B^0 \to K_S^0\pi^0\gamma$ and the $B \to \phi K\gamma$ branching fraction

Joseph Marion Tuggle IV
Doctor of Philosophy, 2009

Dissertation directed by: Professor Abolhassan Jawahery
Department of Physics

I present measurements of radiative B meson decays to the final states $K_S^0\pi^0\gamma$ and $K\phi\gamma$ based on data collected at the $\Upsilon(4S)$ resonance with the *BABAR* detector at the PEP-II e^+e^- collider at SLAC. In a data sample of 467 million $B\overline{B}$ pairs, the time-dependent CP asymmetry in $B^0 \to K_S^0\pi^0\gamma$ decays is measured in two regions of K_S^0-π^0 invariant mass. In the K^* region, $0.8 < m(K_S^0\pi^0) < 1.0\,\mathrm{GeV}/c^2$, we find $S_{K^*\gamma} = -0.03 \pm 0.29 \pm 0.03$ and $C_{K^*\gamma} = -0.14 \pm 0.16 \pm 0.03$; in the range $1.1 < m(K_S^0\pi^0) < 1.8\,\mathrm{GeV}/c^2$, we find $S_{K_S^0\pi^0\gamma} = -0.78 \pm 0.59 \pm 0.09$ and $C_{K_S^0\pi^0\gamma} = -0.36 \pm 0.33 \pm 0.04$. With a sample of 228 million $B\overline{B}$ pairs we measure the branching fraction $\mathcal{B}(B^+ \to K^+\phi\gamma) = (3.5 \pm 0.6 \pm 0.4) \times 10^{-6}$ and set the limit $\mathcal{B}(B^0 \to K^0\phi\gamma) < 2.7 \times 10^{-6}$ at 90% confidence level. The direct CP asymmetry in $B^+ \to K^+\phi\gamma$ is found to be $A_{CP} = (-26 \pm 14 \pm 5)\%$. In each case the uncertainties are statistical and systematic, respectively.

RADIATIVE B MESON DECAY AS A PROBE OF PHYSICS BEYOND THE STANDARD MODEL: Time-dependent CP violation in $B^0 \to K_S^0 \pi^0 \gamma$ and the $B \to \phi K \gamma$ branching fraction

by

Joseph Marion Tuggle IV

Dissertation submitted to the Faculty of the Graduate School of the
University of Maryland, College Park in partial fulfillment
of the requirements for the degree of
Doctor of Philosophy
2009

Advisory Committee:
Professor Abolhassan Jawahery, Chair/Advisor
Professor Alice Mignery
Professor Rabindra Mohapatra
Professor Douglas Roberts
Professor Gregory Sullivan

© Copyright by
Joseph Marion Tuggle IV
2009

Acknowledgements

Doctoral work is not done in a vacuum. Especially in experimental high energy physics, it takes a community to train a new scientist. First and foremost, I want to thank my advisor, Hassan Jawahery, for the opportunity to come to SLAC and work here in person, surrounded by the expertise that has shaped my growth. Prof. Jawahery's guidance has been essential to my progress as a physicist. Thanks are also due to Sally Megonigal and Jane Hessing at the University of Maryland for all their work coordinating logistical issues from nearly 3,000 miles away.

My thanks to the Maryland SLAC postdoc crew: Chunhui Chen, Wouter Hulsbergen, Gabriele Simi, and I'll count Dmytro Kovalskyi here as well (he was *almost* a postdoc by the time I arrived). These guys, especially Gabriele, led me through the details of how to do an analysis.

Giovanni Calderini, Doug Roberts, and Chunhui Chen oversaw my time as on-call expert for the silicon vertex tracker. I gained invaluable hands-on experience in managing a live detector component under very high expectations of uptime as *BABAR* ran in factory mode.

Thanks to those who slogged through the trenches with me: Jake Anderson, Bryan Fulsom, Jim Hirschauer, Tae Min Hong, Karsten Köneke, Chung-Khim Lae, Tim Piatenko, Andy Ruland, Chris Schilling, Steve Sekula, and Minliang Zhao. Well, technically, Steve had already slogged through his own trenches but he came back to ours to offer moral and scientific support.

I appreciate the opportunity given to me by the *BABAR* collaboration, who

allowed me to become a member, to use the data, and to really feel like I own a stake in this enterprise.

And of course, thanks to my wife, Olivia, who has been with me almost since the start of my graduate career. I wouldn't have gotten this far without her constant support. Finally, thanks to my family. They always encouraged me to do what I love, and made sure I had the chance.

Table of Contents

List of Tables vii

List of Figures viii

1 Introduction 1

2 Theoretical Background 4
- 2.1 Electroweak Symmetry Breaking . . . 7
  - 2.1.1 Fermion Masses . . . 9
- 2.2 The CKM Matrix . . . 11
- 2.3 Neutral Meson Mixing . . . 13
- 2.4 The $b \to s\gamma$ Decay as a Probe of New Physics . . . 15
  - 2.4.1 Standard Model Predictions and Observations . . . 15
    - 2.4.1.1 Exclusive Decays . . . 17
    - 2.4.1.2 Photon Polarization . . . 18
  - 2.4.2 New Physics Possibilities . . . 20

3 The *BABAR* Detector 23
- 3.1 Physics at an Asymmetric-Energy Collider . . . 24
- 3.2 Tracking Charged Particles . . . 25
  - 3.2.1 Silicon Vertex Tracker . . . 25
  - 3.2.2 Drift Chamber . . . 29
- 3.3 Particle Identification . . . 33
- 3.4 Calorimetry . . . 37
- 3.5 Muon Detection . . . 41
- 3.6 Triggering . . . 46
  - 3.6.1 Level 1 . . . 47
  - 3.6.2 Level 3 . . . 49

4 Offline Analysis Framework 51
- 4.1 Event Reconstruction . . . 51
  - 4.1.1 Track Reconstruction . . . 52
  - 4.1.2 Particle Identification . . . 59
  - 4.1.3 Neutral Reconstruction . . . 62
- 4.2 B Tagging . . . 64
- 4.3 B Counting . . . 67
- 4.4 Simulation . . . 69

5 Analysis Overview 70
- 5.1 Building Candidates . . . 70
  - 5.1.1 Decay Chain Fitting . . . 70
- 5.2 Separating Signal From Background . . . 71
  - 5.2.1 B Kinematic Variables . . . 71

5.2.2 Angular Distributions . . . 73
5.2.3 Event Shape Variables . . . 74
5.2.4 Low-Level Event Selection . . . 76
5.3 Maximum Likelihood Fitting . . . 77
5.3.1 Conditional Observables . . . 78

6 Time-Dependent *CP* Violation 79
6.1 Mathematical Formalism . . . 79
6.2 Experimental Effects . . . 81
6.3 Measuring Δt . . . 83
6.3.1 Determination of Δz . . . 83

7 Study of $B^0 \to K_S^0 \pi^0 \gamma$ 86
7.1 Event Selection . . . 87
7.1.1 Preselection . . . 88
7.1.2 Final Selection . . . 90
7.1.3 Characterization of Backgrounds . . . 95
7.2 Determination of *CP* Asymmetries . . . 97
7.2.1 Separation of Signal and Background . . . 98
7.2.2 Fit to Δt Distribution . . . 99
7.2.3 Fit Validation . . . 99
7.3 Systematic Uncertainties . . . 102
7.3.1 Δt Determination . . . 103
7.3.1.1 Beamspot and SVT Alignment . . . 103
7.3.1.2 Resolution Function . . . 104
7.3.2 $B\overline{B}$ Background . . . 104
7.3.3 Fitting Procedure . . . 105
7.3.4 Tag-Side Interference . . . 106
7.3.5 Summary . . . 107
7.4 Results . . . 108

8 Study of $B \to K\phi\gamma$ 114
8.1 Event Selection . . . 115
8.1.1 Preselection . . . 115
8.1.2 Kaon Identification . . . 116
8.1.3 Final Selection . . . 118
8.1.4 Characterization of Backgrounds . . . 121
8.2 Determination of Signal and Background Yields . . . 121
8.2.1 Determination of Fixed Parameters . . . 123
8.2.2 Fit Validation . . . 123
8.3 Background Subtraction . . . 126
8.4 Systematic Uncertainties . . . 127
8.4.1 Signal Yields . . . 127
8.4.2 Selection Efficiencies . . . 128
8.4.3 Charge Asymmetry . . . 134

8.5 Results 134

9 Conclusions 139

Bibliography 143

List of Tables

3.1 Relative rates of different event types passing through the entire trigger system. 46

4.1 Tagging category definition and performance. See the text regarding the Lepton and Kaon 1 differences. 67

7.1 Number of MC events used to evaluate selection criteria for $B^0 \to K_S^0\pi^0\gamma$. The "generic" B decays do not include $b \to s\gamma$ processes. . . 88

7.2 Results of linear fits to measured versus generated S and C. 101

7.3 Expected amounts of $B\overline{B}$ background. 105

7.4 Contributions to the $B\overline{B}$ background uncertainty on S and C. . . . 105

7.5 Summary of systematic uncertainties for $B^0 \to K_S^0\pi^0\gamma$. 108

7.6 Fit results for the two $m(K_S^0\pi^0)$ regions. The SM expectations are given for S and C. Reported uncertainties are statistical and, when present, systematic. 108

7.7 Results of the procedure used to recreate the uncorrected value of $S_{K_S^0\pi^0\gamma}$ in data. Line zero is the result of the initial ensemble showing evidence of a bias. 110

8.1 Number of MC events used to evaluate selection criteria for $B \to K\phi\gamma$. 115

8.2 Additive systematic corrections in $B \to K\phi\gamma$. 128

8.3 Summary of the systematic efficiency corrections in $B \to K\phi\gamma$. . . . 133

8.4 Summary of the multiplicative systematic uncertainties in $B \to K\phi\gamma$. 133

List of Figures

2.1 The unitarity triangle related to CP violation in the B system, shown in the complex plane. 13

2.2 A leading order diagram contributing to B^0-$\overline{B}^0$ mixing. 13

2.3 A leading order Feynman diagram for $b \to s\gamma$ decay in the SM. 20

3.1 Transverse section of the SVT. 26

3.2 Longitudinal section of the SVT. 27

3.3 Transverse section of the first four superlayers of the DCH. 31

3.4 Drift time versus distance for tracks passing to the right and to the left of the sense wires in a single DCH layer. 32

3.5 Energy loss versus momentum as measured in the DCH. The curves are the Bethe-Bloch predictions. 33

3.6 On the left, a schematic of the DIRC, longitudinal cross section. On the right, a schematic of the bar boxes. 34

3.7 Efficiency of the various parts of the DIRC as a function of light wavelength. 36

3.8 Longitudinal section of the EMC. 38

3.9 Schematic of the EMC crystals. 39

3.10 Distribution of electrons' energy (E) to momentum (p) in a sample of $e^+e^- \to e^+e^-\gamma$ events. 42

3.11 Schematic of an RPC. 42

3.12 Schematic of the IFR layout. 44

3.13 IFR pion rejection rate (%) as a function of muon identification efficiency (%) for several periods of the IFR's lifetime. 45

4.1 Schematic of the data path from its origin in the *BABAR* detector at PEP-II interaction region 2 (IR2) as raw data (XTC format). It is stored on tape (HPSS) and also sent for offline prompt reconstruction (PR). Processed data are stored as ROOT files. 52

4.2 Difference between track parameters of two halves of cosmic ray muons, (a) Δd_0, (b) Δz_0, (c) $\Delta\phi_0$, (d) $\Delta \tan\lambda$. 54

4.3 Resolution of transverse momentum of cosmic ray muons as a function of transverse momentum. 55

4.4 DCH track reconstruction efficiency relative to the SVT for two operating voltages as a function of transverse momentum (a) and polar angle (b). 56

4.5 SVT low-momentum track reconstruction performance. The top plot (a) shows the soft pion momentum from $D^{*+} \to D^0\pi^+$ in $B\overline{B}$ data (after background subtraction) compared to $B\overline{B}$ Monte Carlo simulation. The bottom plot (b) shows the Monte Carlo reconstruction efficiency of the soft pion. 57

4.6 Plots for electron (left) and muon (right) efficiency and pion fake rate as functions of momentum (top) and polar angle (bottom). The left scales are the efficiency while the right scales give the fake rates. The electron plots are created using tight identification criteria, while the muon plots use loose criteria. 60

4.7 Charged kaon efficiency (top) and pion fake rate (bottom) as a function of momentum in $D^0 \to K^-\pi^+$ processes from D^* sample. 61

4.8 Diphoton invariant mass around the π^0 peak in $B\overline{B}$ events. 63

5.1 Comparison of $m_{\rm ES}$ (solid) and $(m_{\rm Miss} + m_B)/2$ (dashed) for $B \to K\phi\gamma$. The vertical scale is arbitrary, though both histograms are normlized to the same area. 73

5.2 Comparison of $m_{\rm ES}$ (solid) and $m_{\rm Miss}$ (dashed) for $B^0 \to K^0_S\pi^0\gamma$. The vertical scale is arbitrary, though both histograms are normalized to the same area. 74

5.3 Monte Carlo comparison of $|\cos(\theta^*_B)|$ for signal (solid blue) and continuum background (hatched red). The histograms are normalized to equal areas. 75

5.4 Monte Carlo comparison of L_2/L_0 for signal (solid blue) and continuum background (hatched red). The histograms are normalized to equal areas. 76

7.1 Schematic of the $B^0 \to K^0_S\pi^0\gamma$ decay topology near the beam spot (shaded area). 87

7.2 K_S^0 flight length significance in MC for signal and all background sources on the left, and with continuum removed on the right. The contributions on the right are, from the bottom up, generic B^0 decays, generic B^+, $B^+ \to X_s^+\gamma$, $B^0 \to X_s^0\gamma$, non-K^* cross feed, K^* cross feed, K^* signal, and non-K^* signal. The signal distributions are approximately flat and greater than zero, while background distributions peak at zero. The line marks the location of the cut. 91

7.3 π^0 energy [GeV] in MC for signal and all background sources on the left, and with continuum removed on the right. The contributions on the right are, from the bottom up, generic B^0 decays, generic B^+, $B^+ \to X_s^+\gamma$, $B^0 \to X_s^0\gamma$, non-K^* cross feed, K^* cross feed, K^* signal, and non-K^* signal. The line marks the location of the cut. 91

7.4 Signal and background histogram likelihood functions used for the π^0 veto of primary photons. 92

7.5 Signal and background likelihood ratio distributions of the π^0 test samples. 93

7.6 Offpeak data (points) compared to continuum MC (solid) for the π^0 likelihood ratio distributions, normalized to 1. 94

7.7 Δt uncertainty distribution for signal MC events in which both pion daughters of the K_S^0 have at least one ϕ and one z hit in the SVT (left) and events for which the pions are only detected in the DCH (right). 95

7.8 Pull distributions of 500 experiments in the K^* region (top) and the non-K^* region (bottom). A Gaussian fit is overlaid. 100

7.9 Measured S versus generated C for $B^0 \to K^{*0}\gamma$ on the left and $B^0 \to K_S^0\pi^0\gamma$ on the right. 101

7.10 Pull distributions of 250 experiments in the K^* region (top) and the non-K^* region (bottom). Signal is sampled from the MC distributions. 102

7.11 Signal-enhanced distributions for $m_{\rm ES}$ (top) and ΔE (bottom) for the K^* region (left) and the non-K^* region (right). We show the fit result (solid line) and PDFs for signal (long dashed), continuum (short dashed), and $B\overline{B}$ (dotted). 110

7.12 Background-subtracted distributions of Δt in the K^* region (left) and the non-K^* region (right), with $B_{\rm tag}$ tagged as B^0 (top) or $\overline{B}^0$ (center), and the asymmetry (bottom). The curves are the signal PDFs. 111

7.13 Results in the S-C plane showing the 1σ contour for the K^* region (left) and non-K^* region (right). The triangle marks $S = C = 0$, while the dashed circle indicates the physical boundary. 112

7.14 Background-subtracted distribution of $m(K_S^0\pi^0)$. 112

8.1 The probability that kaons, pions, and protons will pass the kaon PID selector described in the text. The angular range corresponds to the DIRC acceptance. 117

8.2 Monte Carlo distributions of the primary photon's CM energy in $B^+ \to K^+\phi\gamma$ (units of GeV). The blue and green histograms are background photons from the neutral and charged generic $B\overline{B}$ samples, respectively. Red is light continuum (u, d, s) and cyan is charm continuum. All backgrounds are scaled to $207\,\mathrm{fb}^{-1}$, while the solid-line histogram is signal MC with arbitrary normalization. 118

8.3 MC distributions of ϕ-K^+ invariant mass in $B^+ \to K^+\phi\gamma$ (units of GeV/c^2). Color coding and normalizations are the same as Fig. 8.2. . 120

8.4 Distribution of the discriminating variables used in the maximum likelihood fit for $B^0 \to K_S^0\phi\gamma$. The dots represent the distribution for signal MC events, and the line is the projection of the fitted PDF. . . 122

8.5 Fits to the $B^0 \to K^{*0}\gamma$ control sample, used to obtain the signal parametrization for $B \to K\phi\gamma$. The blue curve is the signal component, while the red is the background. 124

8.6 Comparison of the $m(\phi K)$ spectrum used in signal MC (solid) and an alternate spectrum as described in the text (dashed). Both histograms have been normalized to 1. 132

8.7 Missing mass (a) and reconstructed mass (b) fits for the charged mode and the neutral mode (c,d). The dotted curves show the background contribution while the solid curves show the sum of signal and background. 135

8.8 Scan of the likelihood as a function of the branching fraction for $B^0 \to K_S^0\phi\gamma$. The solid line is without systematic uncertainties. The dashed line includes them. 137

8.9 The background-subtracted and efficiency-corrected ϕ-K mass distributions (points with uncertainties) for the charged mode (a) and the neutral mode (b). The signal MC model for the mass spectrum is shown as a histogram without uncertainties and is normalized to the data histogram. 138

Chapter 1

Introduction

The $b \to s\gamma$ interaction encompasses a rich array of measurements in which our understanding of fundamental particle physics may be tested against experiment. The predictions for its overall decay rate, the rate asymmetry compared to $\bar{b} \to \bar{s}\gamma$, and the polarization of the photon all depend on whether the virtual particles involved in the process are only those of the standard model of particle physics, or if new particles also contribute. I explore this interaction in two exclusive decay modes using data collected by the *BABAR* detector at SLAC. In $B^0 \to K_S^0\pi^0\gamma$ decays, the photon polarization may be probed through a study of time-dependent *CP* violation. This measurement uses the final *BABAR* dataset, collected between 1999 and 2008. I also present the first *BABAR* measurements of the decay rate and charge asymmetry of $B^+ \to K^+\phi\gamma$, and set a limit on the rate of $B^0 \to K^0\phi\gamma$, using *BABAR* data collected through 2004.

The fundamental electromagnetic, weak, and strong interactions are described in the framework of quantum field theory. Each force is associated with a symmetry of the Lagrangian that encompasses the fundamental matter fields and describes their interactions. With the inclusion of a symmetry-breaking Higgs field, the standard model has withstood every experimental test to which it has been subjected over the past 40 years. One frequently-cited example is the high-precision agreement

between the predicted [1] and measured [2] electron anomalous magnetic moment.

However, despite the successes of the standard model, it has nothing to say about 95% of the energy density of the universe. Approximately 70% is attributed to dark energy driving the expansion of the universe, and 25% to dark matter, inferred from galactic rotation rates and gravitational lensing. The standard model does not incorporate gravity. It does not provide an explanation for why there are three generations of matter, nor why the various elementary particles have the masses they do, nor any reason behind the relative strengths of the interactions between the elementary particles. The linchpin holding together the standard model, the Higgs boson, has not yet been observed. Currently there is no experimental evidence indicating a path between the standard model and what may lie beyond it.

The spectrum of elementary particles has been explored at particle accelerators. Experiments performed at the Fermi National Accelerator Laboratory and the European Organization for Nuclear Research (CERN) have had the potential to observe new particles up to an energy scale of hundreds of GeV. If elementary particles outside the standard model exist, they could be found by new experiments at CERN's Large Hadron Collider. However, there is another way to detect the existence of new particles. The mere potential existence of elementary particles – virtual particles – can have an effect on processes in which they were neither in the initial nor final state. Virtual particles play a large part in the motivation for the measurements presented in this dissertation by allowing facilities such as the PEP-II collider at the SLAC to perform indirect searches for new physics.

The next chapter describes the theoretical background and motivation for

making these measurements. It is followed by a description of the *BABAR* detector, the analysis framework, and an overview of the elements common to both analyses. The details of the two measurements are then presented. Measurements of $b \to s\gamma$ decays offer some of the cleanest testing grounds of the standard model and its eventual successor.

Chapter 2

Theoretical Background

The standard model (SM) is a quantum field theory of quarks, leptons, and the interactions between them. The interactions correspond to the local gauge symmetry of the SM Lagrangian density under the combined group $SU(3)_{\text{color}} \otimes SU(2)_{\text{isospin}} \otimes U(1)_{\text{hypercharge}}$. The subgroups correspond to strong, weak, and electromagnetic forces, respectively. For each generator of the group, there is an associated vector gauge boson that mediates the interaction. The fundamental mathematical details of the interplay between the various fields were spelled out in the 1960's [3, 4, 5, 6].

The Lagrangian density for free, massless fermion fields is written

$$\mathcal{L}_0 = i\overline{\psi}_n \gamma^\mu \partial_\mu \psi_n, \tag{2.1}$$

where sums over repeated indices are assumed, and ψ_n represents the quark or lepton fields indexed by n. The interactions introduced by the various symmetry requirements add further terms to the Lagrangian. To account for the masses of the quarks, leptons, and weak gauge bosons, two scalar Higgs fields are posited. Their properties mask the overall group symmetry of the SM when a perturbative expansion is performed around the vacuum state. There are three known generations of fermions, distinguished only by their interactions with the Higgs sector.

The strong force is governed by the $SU(3)_{\text{color}}$ group. The eight group generators correspond to eight massless gluons, an octet of the color quantum number.

Each flavor of quark is a triplet of $SU(3)_{\text{color}}$, the three types designated red, green, and blue. Leptons are color singlets that do not participate in the strong interaction. Each gluon carries a color and an anti-color, and can therefore interact with other gluons as well as quarks. The $SU(3)$ interaction is represented by adding the following to $\mathcal{L}_0$:

$$\mathcal{L}_{SU(3)} = -g_s \overline{\psi}_n \gamma^\mu G^j_\mu T_j \psi_n - \frac{1}{4} G^{\mu\nu}_j G^j_{\mu\nu}, \tag{2.2}$$

where n runs only over the quarks, g_s is the $SU(3)$ coupling strength, T_j is the generator of $SU(3)$ given by the j'th index, G^j_μ is a gluon field, $G^j_{\mu\nu} = \partial_\mu G^j_\nu - \partial_\nu G^j_\mu + g_s f^j_{kl} G^k_\mu G^l_\nu$, and f^j_{kl} are the $SU(3)$ group structure constants.

The strong interaction potential leads to quark confinement in hadrons, and only composite color singlets have been observed. This part of the SM is called quantum chromodynamics (QCD), and its effects on the work of this dissertation are covered in Sec. 2.4.1.

The combined group $SU(2)_{\text{isospin}} \otimes U(1)_{\text{hypercharge}}$ represents the electroweak force. The triplet of gauge bosons corresponding to the generators of $SU(2)_{\text{isospin}}$ are designated W^+, W^0, and W^-. The $U(1)_{\text{hypercharge}}$ generator, B^0, is a singlet of both color and isospin. Because the W^0 and B^0 have the same quantum numbers, linear combinations of the two are observed as the physical Z^0 weak boson and the A^0 photon field, related by the weak mixing angle θ_W:

$$\begin{aligned} W^{0\mu} &= Z^\mu \cos\theta_W + A^\mu \sin\theta_W \\ B^\mu &= -Z^\mu \sin\theta_W + A^\mu \cos\theta_W. \end{aligned} \tag{2.3}$$

The $SU(2)_{\text{isospin}}$ interaction distinguishes between left- and right-chiral fermion

fields. This distinction is reflected in the $V-A$ (vector minus axial vector) structire of the weak interaction Lagrangian. The left-handed quarks are organized into weak isospin doublets

$$\begin{pmatrix} u \\ d \end{pmatrix}_L \begin{pmatrix} c \\ s \end{pmatrix}_L \begin{pmatrix} t \\ b \end{pmatrix}_L ,$$

while the right-handed ones are weak isospin singlets and do not participate in $SU(2)_{\text{isospin}}$ interactions. Similarly, the leptons are also grouped into left-handed isospin doublets

$$\begin{pmatrix} \nu_e \\ e \end{pmatrix}_L \begin{pmatrix} \nu_\mu \\ \mu \end{pmatrix}_L \begin{pmatrix} \nu_\tau \\ \tau \end{pmatrix}_L$$

and right-handed singlets. For antiparticles, the left-handed ones are in singlets, while the right-handed ones are in doublets[1].

The fermions' $U(1)$ hypercharge Y is related to the electric charge Q and the third isospin component I_3 by $Q = I_3 + Y$. The Lagrangian density for electroweak interactions is given by:

$$\mathcal{L}_{\text{EW}} = -\overline{\mathbf{\Psi}}^L_m \gamma^\mu \left[g W^j_\mu \tau_j/2 + g' Y_m B_\mu \right] \mathbf{\Psi}^L_m - g' Y_n \overline{\psi}^R_n \gamma^\mu B_\mu \psi^R_n - \frac{1}{4} W^{\mu\nu}_j W^j_{\mu\nu} - \frac{1}{4} B^{\mu\nu} B_{\mu\nu}, \tag{2.4}$$

where $\mathbf{\Psi}^L_m$ are the m left-handed fermion isospin doublets, ψ^R_n are the n right-handed fermion singlets, g and g' are the $SU(2)$ and $U(1)$ coupling strengths, τ_j are the Pauli spin matrices, $W^j_{\mu\nu} = \partial_\mu W^j_\nu - \partial_\nu W^j_\mu + g\varepsilon_{jkl} W^k_\mu W^l_\nu$, and $B_{\mu\nu} = \partial_\mu B_\nu - \partial_\nu B_\mu$. After substitution of Eq. 2.3 and defining the electromagnetic interaction Lagrangian to be $Q_n \overline{\psi}_n \gamma^\mu A_\mu \psi_n$, one obtains the relations $g \sin\theta_W = g' \cos\theta_W = e$, with e being

[1] Charge-conjugate states are implied throughout this thesis except where noted.

the charge of the positron.

The choice of different quantum numbers for right- and left-handed fermions, motivated by 50 years of experiments, breaks two possible discrete symmetries of the Lagrangian: charge-conjugation (C) and parity (P). The first swaps particles and antiparticles, while the second swaps right-handed particles for left-handed ones. However, the combined symmetry CP is still preserved in the Lagrangians given up to this point.

2.1 Electroweak Symmetry Breaking

A key feature of the SM is that the gauge symmetry of the Lagrangian density is masked by postulating that the minimum of the Higgs potential is not the vacuum state. Rather, the Higgs potential has a so-called vacuum expectation value.

The Higgs sector in the SM is composed of a weak isospin doublet of complex scalar fields $\mathbf{\Phi} = \begin{pmatrix} \phi^+ \\ \phi^0 \end{pmatrix}$. Adding the Higgs doublet to the Lagrangian requires the propagation and self-interaction terms:

$$\mathcal{L}_0^{\text{Higgs}} = [\partial^\mu \mathbf{\Phi}]^\dagger [\partial_\mu \mathbf{\Phi}] - \mu^2 \mathbf{\Phi}^\dagger \mathbf{\Phi} - \lambda [\mathbf{\Phi}^\dagger \mathbf{\Phi}]^2. \tag{2.5}$$

This is the first mass term ($-\mu^2 \mathbf{\Phi}^\dagger \mathbf{\Phi}$) that has been introduced into the Lagrangian density. It was not possible for the fermion or gauge boson fields, since that would break the invariance of the Lagrangian under its symmetry group. To break electroweak symmetry in a way consistent with observations, one assumes $\lambda > 0$ and $\mu^2 < 0$.

One can write the Higgs field in terms of four real scalar fields called η_1, η_2, η_3, and h: $\mathbf{\Phi}= \frac{1}{\sqrt{2}} \begin{pmatrix} \eta_1 + i\eta_2 \\ h + i\eta_3 \end{pmatrix}$. Because the Higgs doublet is symmetric under $SU(2)$, any isospin-up components can be transformed into isospin-down by an appropriate choice of gauge. Furthermore, because the isospin-down term is also symmetric under $U(1)$ hypercharge, any imaginary part of that component can be made real through a $U(1)$ transformation. This leaves only one physical Higgs field. To be consistent with observations, we take it to be h. This choice masks the overall symmetry of the Lagrangian, as the h field is not symmetric under $SU(2)$ isospin transformations.

As the Higgs potential has been defined, its minimum occurs at $\mathbf{\Phi}_0^\dagger \mathbf{\Phi}_0 = -\mu^2/2\lambda$. This minimum is a circle in the $|\phi_0^+|$-$|\phi_0^0|$ plane since $\mathbf{\Phi}_0^\dagger \mathbf{\Phi}_0 = |\phi_0^+|^2 + |\phi_0^0|^2$. A perturbative expansion is only valid at such a minimum, and the choice of h described above yields $\mathbf{\Phi}_0 = \begin{pmatrix} 0 \\ \sqrt{\frac{-\mu^2}{2\lambda}} \end{pmatrix}$. The vacuum expectation value is closely related to the value of the Higgs field at its minimum: $v \equiv \sqrt{-\mu^2/\lambda}$. The physical Higgs field is then $\mathbf{\Phi} = \frac{1}{\sqrt{2}} \begin{pmatrix} 0 \\ v + h \end{pmatrix}$. This parameterization of the Higgs sector is known as the unitary gauge. Plugging it into Eq. 2.5 gives the physical Higgs mass $m_H = v\sqrt{2\lambda}$.

The Higgs electroweak interaction is given by:

$$\mathcal{L}_{\text{EW}}^{\text{Higgs}} = \mathbf{\Phi}^\dagger \left[g(\tau_j W_\mu^j/2) + g' B_\mu/2 \right]^\dagger \left[g(\tau_j W_\mu^j/2) + g' B_\mu/2 \right] \mathbf{\Phi}. \tag{2.6}$$

After rewriting this in the unitary gauge one can isolate the now-apparent mass

terms for the electroweak gauge bosons by taking $\mathbf{\Phi} \to \mathbf{\Phi}_0$:

$$
\begin{aligned}
&\left|\left[g(\tau_j W^j_\mu/2) + g' Y B_\mu/2\right] \mathbf{\Phi}_0\right|^2 \\
&\quad = \frac{1}{8}\left|\begin{pmatrix} gW^0_\mu + g'B_\mu & g\sqrt{2}W^+_\mu \\ g\sqrt{2}W^-_\mu & -gW^0_\mu + g'B_\mu \end{pmatrix}\begin{pmatrix} 0 \\ v \end{pmatrix}\right|^2 \\
&\quad = \frac{1}{8}\left|\begin{pmatrix} g\sqrt{2}vW^+_\mu \\ v\left[-gW^0_\mu + g'B_\mu\right] \end{pmatrix}\right|^2 \\
&\quad = \frac{1}{4}g^2v^2(W^-)^\mu W^+_\mu + \frac{1}{8}g^2v^2W^{0\mu}W^0_\mu + \frac{1}{8}g'^2v^2B^\mu B_\mu - \frac{1}{4}gg'v^2B^\mu W^0_\mu. \qquad (2.7)
\end{aligned}
$$

The first term in the final line corresponds to the charged W mass: $M_W = \frac{1}{2}gv$. The remaining terms are associated with masses of the neutral electroweak bosons. Writing these in terms of Z^μ and A^μ, one finds that the terms involving $A^\mu A_\mu$ completely cancel, leaving the photon with zero mass. The remaining terms simplify to $\frac{1}{8}v^2(g^2+g'^2)Z^\mu Z_\mu$, yielding a Z^0 boson mass of $M_W/\cos\theta_W$. Given the measured values of these masses, the vacuum expectation value is 246 GeV and the weak mixing angle is given by $\sin^2\theta_W = 0.231$ [7].

2.1.1 Fermion Masses

The fermions acquire mass in the SM through their coupling to the Higgs doublet. The most general form of this coupling allowed within the SM structure is

$$
\mathcal{L}_{\text{HF}} = -\left[(Y_d)^{ij}\left(\overline{u}^i_L, \overline{d}^i_L\right)\begin{pmatrix} \phi^+ \\ \phi^0 \end{pmatrix} d^j_R + (Y_u)^{ij}\left(\overline{u}^i_L, \overline{d}^i_L\right)\begin{pmatrix} \overline{\phi}^0 \\ -\phi^- \end{pmatrix} u^j_R + \text{h.c.}\right], \qquad (2.8)
$$

where Y_d and Y_u are completely general complex matrices, the indices i and j indicate fermion generation, and u and d represent the up-type and down-type fermions. In the SM the Higgs does not couple between quarks and leptons, so the description here applies separately to those two sectors. Y_d and Y_u are not necessarily diagonal in the basis of fermion flavor, meaning that the mass eigenstates and the flavor eigenstates are in general different. These matrices can be diagonalized by two unitary transformations each:

$$\begin{aligned} Y_d &= V_d^L M_d (V_d^R)^\dagger \\ Y_u &= V_u^L M_u (V_u^R)^\dagger, \end{aligned} \tag{2.9}$$

where the M matrices are diagonal and non-negative, and the V matrices are unitary. If one redefines the fermion fields such that $u_{L(R)} \to V_u^{L(R)} u_{L(R)}$, and $d_{L(R)} \to V_d^{L(R)} d_{L(R)}$, Eq. 2.8 becomes

$$\mathcal{L}_{\mathrm{HF}} = -\left(M_d^i \frac{v+h}{\sqrt{2}} \overline{d}_i d_i + M_u^i \frac{v+h}{\sqrt{2}} \overline{u}_i u_i \right). \tag{2.10}$$

The terms proportional to v correspond to fermion mass terms, while those proportional to h correspond to fermion interactions with the physical scalar Higgs boson.

An important implication of the difference between mass eigenstates and flavor eigenstates is that the charged-current weak interactions are modified when written in the mass basis. One finds that the redefinition of the fermion fields leaves Eq. 2.4 invariant except for the terms that couple up-type fermions to down-type through

charged W interactions:

$$\frac{g}{\sqrt{2}}\left[\overline{u}_L^i\gamma^\mu W_\mu^+ d_L^i + \overline{d}_L^i\gamma^\mu W_\mu^- u_L^i\right] \rightarrow$$
$$\frac{g}{\sqrt{2}}\left[\overline{u}_L^i(V_u^L)_{ij}^\dagger\gamma^\mu W_\mu^+(V_d^L)_{jk}d_L^k + \overline{d}_L^i(V_d^L)_{ij}^\dagger\gamma^\mu W_\mu^-(V_u^L)_{jk}u_L^k\right]. \tag{2.11}$$

That is, all charged-current weak interactions among the quarks are modified by the unitary matrix $V_{\mathrm{CKM}} \equiv (V_u^L)^\dagger V_d^L$ named after Cabibbo, Kobayashi, and Maskawa. Cabibbo introduced the concept of mixing between quarks of two different generations [8], while Kobayashi and Maskawa [9] extended this to three quark generations. An analogous matrix applies to the lepton system, but is beyond the scope of this dissertation.

2.2 The CKM Matrix

One consequence of the unconstrained couplings between the Higgs and the fermions is that they can be complex, and therefore *CP* may not necessarily be a good symmetry of the Lagrangian. The information on the complex phases of the couplings is wrapped up in the CKM matrix. Because it is a unitary 3×3 matrix, it can be parameterized in terms of three angles, analogous to the angles in a three-dimensional rotation, and six complex phases. Five of these phases may be absorbed into redefinitions of the relative phases between the quark fields. This leaves one remaining phase, which implies *CP* violation if it is nonzero.

CP violation has indeed been measured both in kaon and B meson decays. To determine whether the CKM formalism sufficiently describes the observations, it is necessary to measure the values of as many matrix elements as possible. These come

from a variety of sources, including beta decay ($|V_{ud}|$), semileptonic meson decays ($|V_{us}|$, $|V_{cs}|$, $|V_{cb}|$, $|V_{ub}|$, $|V_{tb}|$), neutrino interactions with down quarks ($|V_{cd}|$), and loop-mediated processes like B^0 mixing and rare B and K decays ($|V_{ts}|$, $|V_{td}|$) [7]. Information from CP-violating asymmetries involves complex phases in the CKM matrix.

Due to the unitarity requirement, there are six sums of CKM matrix elements that add to zero. These may be represented as six triangles in the complex plane. Of particular interest to this work is the one associated with the B meson system:

$$V_{ud}V_{ub}^* + V_{cd}V_{cb}^* + V_{td}V_{tb}^* = 0. \tag{2.12}$$

To get a sense of the properties of this triangle it is useful to consider the Wolfenstein parameterization of the CKM matrix [10]:

$$V_{CKM} = \begin{pmatrix} 1-\frac{\lambda^2}{2} & \lambda & A\lambda^3(\rho - i\eta) \\ -\lambda & 1-\frac{\lambda^2}{2} & A\lambda^2 \\ A\lambda^3(1-\rho-i\eta) & -A\lambda^2 & 1 \end{pmatrix} + \mathcal{O}(\lambda^4), \tag{2.13}$$

where $\lambda = 0.22$, the sine of the Cabibbo angle, and A, ρ, and η are real numbers of order 1. From this definition, it is clear that the sides of the triangle represented by Eq. 2.12 are all of the same order of magnitude ($A\lambda^3$). This is in contrast to the other five triangles, in which one side dominates. After dividing each side by $V_{cd}V_{cb}^*$, Eq. 2.12 may be represented as in Fig. 2.1, which defines the angles α, β, and γ. This representation is referred to as the unitarity triangle for its importance in testing the CKM description of charged-current quark interactions.

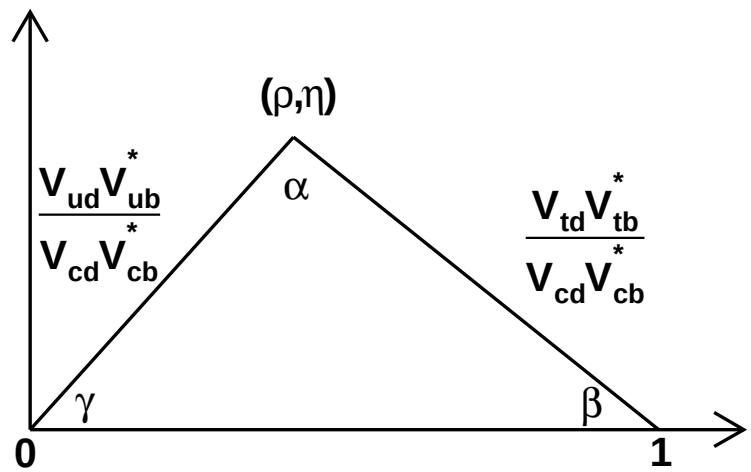

Figure 2.1: The unitarity triangle related to CP violation in the B system, shown in the complex plane.

2.3 Neutral Meson Mixing

A neutral meson composed of fermions from different generations is subject to a phenomenon known as mixing. This process, depicted for the B^0 system in Fig. 2.2, causes the meson to oscillate back and forth between its antiparticle and itself. I briefly describe the physics of mixing for a neutral meson M^0.

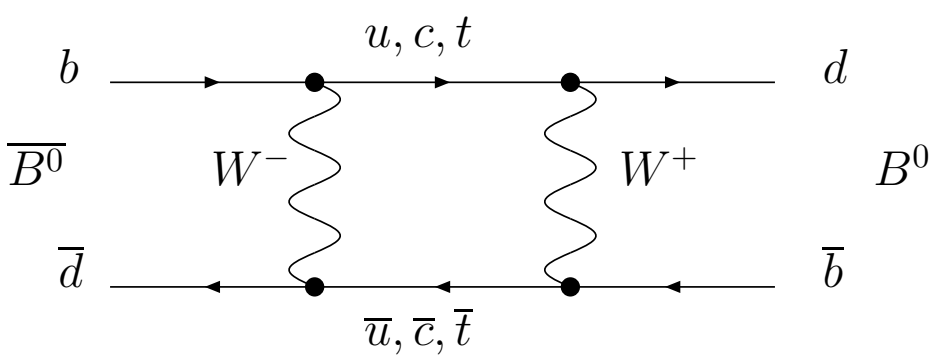

Figure 2.2: A leading order diagram contributing to B^0-$\overline{B}^0$ mixing.

I begin by defining the light $|M_L\rangle$ and heavy $|M_H\rangle$ mass eigenstates in terms of the flavor eigenstates:

$$|M_L\rangle = p|M^0\rangle + q|\overline{M^0}\rangle$$

$$|M_H\rangle = p|M^0\rangle - q|\overline{M^0}\rangle,$$

with complex numbers p and q such that $|p|^2 + |q|^2 = 1$. On timescales shorter than the M^0 lifetime, an arbitrary state with some admixture of flavor states will evolve according to the 2×2 Hamiltonian operator $H = M - \frac{i}{2}\Gamma$, defined in terms of Hermitian matrices M and Γ. Diagonalizing H gives the masses and widths of $|M_L\rangle$ and $|M_H\rangle$. I define $|M^0(t)\rangle \equiv e^{-iHt}|M^0\rangle$ as the state of a system which is completely $|M^0\rangle$ at time $t = 0$, and similarly $|\overline{M^0}(t)\rangle \equiv e^{-iHt}|\overline{M^0}\rangle$. These definitions yield the time-dependent states

$$\begin{aligned} |M^0(t)\rangle &= e^{-i\overline{m}t}e^{-\Gamma t/2}\left[\cos(\Delta m t/2)|M^0\rangle + \frac{q}{p}i\sin(\Delta m t/2)|\overline{M^0}\rangle\right] \\ |\overline{M^0}(t)\rangle &= e^{-i\overline{m}t}e^{-\Gamma t/2}\left[\cos(\Delta m t/2)|\overline{M^0}\rangle + \frac{p}{q}i\sin(\Delta m t/2)|M^0\rangle\right], \end{aligned} \tag{2.14}$$

where $\overline{m} \equiv \frac{1}{2}(m_H + m_L)$, $\Delta m \equiv m_H - m_L$, and I have assumed $\Gamma_H \approx \Gamma_L$. This assumption is appropriate for the B^0 system, and relevant for this work. However, it would not be appropriate for a description of D^0 or K^0 mixing. From Eq. 2.14 it is apparent that the mixing frequency is proportional to the mass difference between the heavy and light states. Any possible CP violation in the mixing process is contained in the values and phases of p and q. I return to B^0 mixing in Chapter 6, where it is exploited as a tool to search for physics beyond the SM.

2.4 The $b \to s\gamma$ Decay as a Probe of New Physics

There are no tree-level interactions in the SM that involve two quarks of the same charge but different flavors. Put another way, there are no flavor-changing neutral currents (FCNC) at tree level in the SM. At leading order, FCNC processes proceed through a loop involving a charged W and a quark. These processes are suppressed by at least a factor of the weak coupling coefficient, relative to other weak interactions that only require one vertex. Additionally, because weak interactions involve the nearly-diagonal CKM matrix, FCNCs are further suppressed by an off-diagonal element. Although these suppression factors make FCNC processes rare, they are sensitive to undiscovered particles that may replace the SM particles in the loop, and thereby lead to observations that are at odds with the SM predictions. Here I focus on a particular type of radiative FCNC decay: $b \to s\gamma$. The measurements one can make to search for new physics include the branching fraction, the charge asymmetry, and the photon polarization. The work in this thesis concerns the two exclusive decay modes $B^0 \to K_S^0\pi^0\gamma$ and $B \to K\phi\gamma$.

2.4.1 Standard Model Predictions and Observations

One of the calculational tools in quantum field theory is the operator product expansion (OPE). This is based on the assumption that the short-distance (high-energy), pointlike behavior of QCD can be factorized from its long-distance (low-energy) behavior. The effective Hamiltonian is written as the sum of a series of so-called Wilson coefficients $\mathcal{C}_i(\mu)$ multiplied by operators $\mathcal{O}_i(\mu)$. The $\mathcal{C}_i(\mu)$ charac-

terize the short-distance effects at the energy scale μ and are obtained by calculating the Feynman diagrams associated with those interactions using a perturbative expansion in k^2/M^2, where k is the typical momentum transfer for the propagator of a particle of mass $M > \mu$. This procedure is said to "integrate out" the particles of rest mass greater than μ. In B decays, this means integrating over the W, Z and t fields. The long-distance effects are characterized by the $\mathcal{O}_i(\mu)$ operators, which are usually written as effective interactions up to dimension six. For the $b \to s\gamma$ process, there are eight relevant operators [11, 12]. The most significant contributions are from the electromagnetic dipole operator $O_{7\gamma}$ and the color singlet current-current operator O_{2c}:

$$\begin{aligned} O_{7\gamma} &= \frac{e}{8\pi^2}\overline{s}\sigma^{\mu\nu}(m_s P_L + m_b P_R) b F_{\mu\nu} \\ O_{2c} &= (\overline{s}\gamma^\mu P_L c)(\overline{c}\gamma_\mu P_L b), \end{aligned} \tag{2.15}$$

where $P_L^R = (1 \pm \gamma^5)/2$. The contributions from the perturbative expansion at high energy are matched onto these operators to determine the Wilson coefficients.

At next-to-next-to-leading order in QCD corrections, the $b \to s\gamma$ branching fraction has been calculated to be $\mathcal{B}(b \to s\gamma) = (3.15 \pm 0.23) \times 10^{-4}$ for photon energy $E_\gamma > 1.6\,\text{GeV}$ in the B meson rest frame [13]. The Heavy Flavor Averaging Group [14] reports the experimental average to be $\mathcal{B}(b \to s\gamma) = (3.52 \pm 0.25) \times 10^{-4}$ based on results from *BABAR*, Belle and CLEO. The SM charge asymmetry is expected to be quite small at $A_{CP} = 0.006$ [15, 16]. Experimentally, the world average is $A_{CP} = 0.004 \pm 0.037$. For inclusive $b \to s\gamma$, the experimental results are consistent with SM expectations, constraining the range of parameters in extensions

to the SM.

2.4.1.1 Exclusive Decays

When dealing with specific exclusive decays, in which the products are strongly-bound states of quarks, the details of the nonperturbative QCD interactions become relevant and introduce significant uncertainty into the calculations. Although experimentally reconstructing exclusive decays is easier than searching for inclusive ones, the theoretical details relating to form factors and QCD effects make predictions more difficult. For $B^0 \to K^{*0}\gamma$, predictions of the branching fraction range from $(5.8 - 7.9) \times 10^{-5}$, with theoretical uncertainties of 30–50% [17, 18, 19, 20]. These analyses use a variety of methods based on the OPE, extended with approximations appropriate for certain regions of the kinematic space. For example, Ref. [17] works in limit that the final-state hadron's energy E is large compared to the strong-interaction energy scale Λ_{QCD}, allowing perturbative expansions in Λ_{QCD}/E. The situation is clearer on the experimental side, with the branching fraction measured as $\mathcal{B}(B^0 \to K^{*0}\gamma) = (4.01 \pm 0.20) \times 10^{-5}$ [7]. The charge asymmetry is expected to be of the same order of magnitude as the inclusive $b \to s\gamma$ case. The world average including neutral and charged B decays is $A_{CP}(B \to K^*\gamma) = -0.010 \pm 0.028$.

The theoretical situation for $B \to K\phi\gamma$ is not as clear. There are no calculations of its branching fraction, which is expected to be smaller than that of $B \to K^*\gamma$, nor of its charge asymmetry, which is also expected to be very small. An angular analysis of the final-state particles would provide another test of the SM

by studying CP-conserving forward-backward asymmetries that involve the photon polarization [21, 22]. However the decay is so rare that such an analysis would be statistically limited even with *BABAR*'s large data sample, and it is outside the scope of this work. The measurements presented here are of the branching fraction and charge asymmetry. These represent first step toward future measurements, which could include time-dependent CP violation in $B^0 \to K_S^0 \phi\gamma$ and the angular observables.

2.4.1.2 Photon Polarization

The SM makes a robust prediction regarding the photon polarization in $b \to s\gamma$ [23]. Because the weak interaction depends on the helicity of the particles involved, the SM predicts polarization of the photon depending on whether it came from a b or $\overline{b}$. The leading order term of the effective Hamiltonian for the process involves the operator $O_{7\gamma}$ (Eq. 2.15):

$$\mathcal{H}_{\text{eff}} = -\frac{G_F}{\sqrt{2}} V_{tb} V_{ts}^* \frac{e}{4\pi^2} \overline{s}\sigma^{\mu\nu}(m_s P_L + m_b P_R) b F_{\mu\nu} + \text{h.c.}, \tag{2.16}$$

Equation 2.16 represents the four processes $b_L \to s_R\gamma_R$, $b_R \to s_L\gamma_L$, $\overline{b}_R \to \overline{s}_L\gamma_L$, and $\overline{b}_L \to \overline{s}_R\gamma_R$. Because the weak interaction only involves left-handed quarks and right-handed antiquarks, in each case one of the quark lines must flip its helicity. This occurs at a rate proportional to the quark mass, leading to dominance of the processes $b_R \to s_L\gamma_L$ and $\overline{b}_L \to \overline{s}_R\gamma_R$. That is, in the SM, one expects a higher rate of $\overline{B}^0$ decays to left-polarized photons than right-polarized ones.

Although *BABAR* cannot detect photon polarization directly, Atwood, Gronau,

and Soni showed that it can be inferred in a time-dependent CP violation (TDCPV) measurement involving a final state accessible to both B^0 and $\overline{B}^0$ [23]. TDCPV relies on the interference between mixing and decay diagrams, and vanishes if this interference is not present. In the limit $\left(\frac{m_s}{m_b}\right) \to 0$, the photon helicity in $b \to s\gamma$ tags the B meson flavor, and therefore will not lead to this kind of interference. However, the small rate of "wrongly" polarized photons does allow for some interference at a rate proportional to m_s/m_b.

The most frequent, neutral, exclusive $b \to s\gamma$ decay is $B^0 \to K^{*0}\gamma$. One can investigate TDCPV in this decay using $K^{*0} \to K_S^0\pi^0$. SM predictions of S, the CP violation due to interference between mixing and decay, in this mode vary due to hadronic uncertainties. Taking just the $O_{7\gamma}$ contribution, one expects $S = -2\frac{m_s}{m_b}\sin(2\beta)$ [23]. Using $m_s = 0.095\,\mathrm{GeV}/c^2$, $m_b = 4.65\,\mathrm{GeV}/c^2$, and $\sin(2\beta) = 0.725$ this gives $S \approx -0.030$. A calculation in perturbative QCD with a model-dependent treatment of non-perturbative effects yields $S = -0.035 \pm 0.017$ [24]. Grinstein *et al.* [25, 26] call attention to the largest SM contribution to wrongly-polarized photons, which is the O_{2c} operator involving the charm quark (Eq. 2.15). By those authors' dimensional estimate, $|S|$ could be as large as 0.1, with large hadronic uncertainties coming mainly from soft gluon contributions. Although there is not a solid consensus, Ball and Zwicky [27] calculate the contribution from soft gluons using QCD sum rules [28] and find the corrections to be much smaller than the dimensional estimate, leading to the prediction $S = -0.022 \pm 0.015^{+0}_{-0.010}$. In summary, the value of S in the SM is expected to be under the 10% level, and any evidence to the contrary would point to a source beyond the SM.

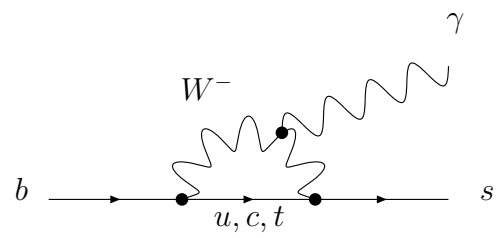

Figure 2.3: A leading order Feynman diagram for $b \to s\gamma$ decay in the SM.

2.4.2 New Physics Possibilities

The inclusive $b \to s\gamma$ branching fraction and direct CP asymmetry are dominated by SM processes, severely constraining any non-SM effects. However, even with these constraints, the photon polarization could still depart from the SM expectation.

One of the leading-order quark-level diagrams for $b \to s\gamma$ decay is shown in Fig. 2.3. In general, any right-handed fermion of mass m_f that replaces the internal quark line yields a contribution to right-polarized photons that carries a weight of m_f/m_b relative to the SM contribution. Essentially, this is a test of the $V - A$ structure of the weak interaction, deviations from which occur in several models of new physics.

The left-right symmetric model (LRSM) [29, 30, 31, 32] assumes an electroweak gauge structure of $SU(2)_{V-A} \otimes SU(2)_{V+A} \otimes U(1)$, first considered in [33]. This posits right-handed fermion doublets, and also new W_R gauge bosons (analogous to the W_L bosons in the SM that govern interactions of the left-handed doublets), whose interactions must be suppressed. This is accomplished by the Higgs mechanism, which forms mass eigenstates W_1 (light) and W_2 (heavy). To account for the pre-

dominance of $V-A$ at observable energies, W_1 must be mostly W_L. Mixing between the charged W bosons is governed by the angle ζ:

$$W_1^+ = W_L^+ \cos(\zeta) + W_R^+ e^{i\alpha} \sin(\zeta)$$
$$W_2^+ = -e^{i\alpha} W_L^+ \sin(\zeta) + W_R^+ \cos(\zeta), \tag{2.17}$$

where α is a possible CP-violating phase.

The effect of this model on $b \to s\gamma$ processes was examined in [34, 35, 36, 37, 38]. In principle, large contributions of $\mathcal{O}(m_t/m_b)$ could have affected $\mathcal{B}(b \to s\gamma)$ in this model due to W_L-W_R mixing and charged Higgs exchange. However, the first $B \to K^*\gamma$ results from CLEO [39] showed that any $V+A$ contributions had to be smaller than a few percent, while measurements of kaon mixing place a limit of $m_{W_2} < 1.6\,\mathrm{TeV}/c^2$ [40], and measurements of $|V_{us}|$ and $|V_{ud}|$, combined with a limit on $|V_{ub}|$, yield $\zeta < 0.005$ [41]. However, the authors of [23] find that even with the limit of $\zeta < 0.003$ and the above m_{W_2} limit, $S_{K^{*0}\gamma}$ could be as large as ± 0.46.

In supersymmetric (SUSY) models, where each SM particle has a partner of spin different by $\frac{1}{2}$, there are new diagrams that contribute alongside the SM ones. The example in Fig. 2.3 could be modified by replacing the internal lines with their superpartners or replacing the charged W with a charged Higgs. Whereas a more equal rate of right-to-left polarized photons would bring S closer to $-\sin(2\beta)$, new CP-violating phases due to SUSY interactions could induce larger changes. In general, flavor-changing processes and CP violation are not well-constrained by supersymmetric models, as they depend on the details of the symmetry breaking. For example, in generic SUSY with unconstrained squark mixing between the second

and third generations, S could be as large as 90% [42], even without significant deviations from the SM in the branching fraction or direct CP asymmetry. If such a large mixing-induced CP violation were to be observed, it would be an unambiguous signal for non-SM physics.

The study of $B^0 \to K_S^0 \pi^0 \gamma$ in this work uses the method suggested by Atwood *et al.* [23] to probe the photon polarization via time-dependent CP violation. The measurements of $B \to K\phi\gamma$ serve as a first step toward possible measurements in the future of angular distributions and time-dependent CP violation in $B^0 \to K_S^0 \phi\gamma$.

Chapter 3

The *BABAR* Detector

BABAR was built to study *CP* asymmetries in B mesons and to test whether the CKM picture of *CP* violation in the standard model (SM) accounts for observations in the laboratory. In part, this requires measuring the angles of the unitarity triangle as accurately as possible to determine whether they add up to 180°. Other *BABAR* goals include measuring the rates and properties of rare decays such as the ones considered in this thesis. A systematic study of many B decay modes to *CP* eigenstates is needed to determine the CKM angles through time-dependent CP violation (TDCPV). This requires accurate reconstruction of the proper lifetime difference between the two B mesons produced by $\Upsilon(4S)$ decays, and therefore precision determination of the spatial separation between the B decay vertices. For this reason, *BABAR* was built in conjunction with the asymmetric-energy PEP-II storage rings.

The *BABAR* detector is a magnetic spectrometer that consists of five subdetectors. The charged-particle tracking system is composed of a five-layer, double-sided silicon strip detector and a 40-layer drift chamber. A ring-imaging Cherenkov light detector determines particle velocities for particle identification. The electromagnetic calorimeter uses 6580 cesium iodide crystals to determine photon and electron energies. All of these subsystems are immersed in a 1.5 T magnetic field

produced by a superconducting solenoid. The steel magnetic flux return is instrumented with resistive plate chambers and limited streamer tubes to identify muons and neutral hadrons. I discuss each of these systems in more detail below. A full description may be found in Ref. [43].

3.1 Physics at an Asymmetric-Energy Collider

At PEP-II, electrons and positrons collide at a center-of-mass (CM) energy corresponding to the $\Upsilon(4S)$ resonance, which decays almost exclusively to $B\overline{B}$ meson pairs. At this energy of 10.58 GeV, the B mesons are produced nearly at rest, with momenta of about 340 MeV/c. The B flight lengths of are $\mathcal{O}(30\,\mu\text{m})$, which makes the distance between the B decay vertices too small to be measured with current technology. Therefore, the electron and positron beams collide at asymmetric energies to produce a moving $B\overline{B}$ system in the laboratory frame along the axis of the beams. The 9.0 GeV electrons on 3.1 GeV positrons yield a boost $\beta\gamma = 0.56$, and larger B decay separations along the z axis (e^- direction). In this configuration, the vertex separation Δz is $\mathcal{O}(250\,\mu\text{m})$.

The boost in the forward direction leads to a difference between the detector coverage in the laboratory frame and in the CM frame. Polar angles (measured from the $+z$ direction) between the two frames are related by

$$\cos\theta_{\text{Lab}} = \frac{\gamma\cos\theta_{\text{CM}} + \gamma\beta}{\sqrt{(\gamma\cos\theta_{\text{CM}} + \gamma\beta)^2 + \sin^2\theta_{\text{CM}}}}. \tag{3.1}$$

For example, a polar angle of 90° in the CM frame corresponds to about 60° in the laboratory. Therefore, the *BABAR* detector was designed with more sensitivity and

granularity in the forward direction.

3.2 Tracking Charged Particles

The *BABAR* tracking system is composed of a silicon vertex tracker (SVT) and a small-cell drift chamber (DCH). Measuring the trajectory of a charged particle in a magnetic field determines its momentum, charge, and distance of closest approach to the interaction point. Measurements of the ionization energy loss ($\mathrm{d}E/\mathrm{d}x$) provide information about the identity of the particle. The next two subsections describe how the SVT and DCH achieve these tasks.

3.2.1 Silicon Vertex Tracker

The SVT is the innermost subsystem of the *BABAR* detector, its first layer positioned just 4 mm outside the beam pipe and 32 mm away from the interaction point. It is responsible for precise spatial and angular measurements of charged-particle trajectories near the interaction point. These measurements are crucial in reconstructing B decay vertices. The angular resolution is also important in determining Cherenkov light angles produced in the particle identification system (Sec. 3.3). The SVT is the only part of the *BABAR* tracking system that can measure particles of transverse momentum less than 120 MeV/c, which do not reach the drift chamber. It measures $\mathrm{d}E/\mathrm{d}x$ though charge deposition in the silicon strips.

The SVT consists of five layers of double-sided, AC-coupled silicon strip detectors. The strips are p^+ and n^+ implants in an n-type substrate. The space between

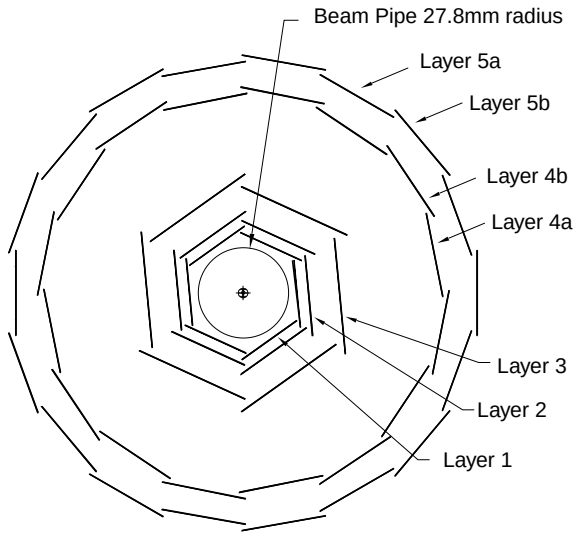

Figure 3.1: Transverse section of the SVT.

the strips varies from 50 μm to 210 μm, with over 150,000 readout channels in total. The modules are reverse-biased by 40 V to deplete the inner region of charge carriers.When a charged particle passes through, some of its energy is deposited in the form of electron-hole pairs created in the substrate.

Transverse and longitudinal cross sections of the SVT are shown in Figures 3.1 and 3.2. As depicted in the latter, the outer two layers use arch-shaped modules to provide more angular coverage. The modules range in size from $43 \times 42\,\mathrm{mm}^2$ to $68 \times 53\,\mathrm{mm}^2$, yielding a total active area of $0.96\,\mathrm{m}^2$ and covering 90% of the solid angle in the CM frame. The wafers are mounted on a carbon-fiber and Kevlar frame. Tracks pass through approximately 4% of a radiation length in the SVT. The data acquisition electronics on the SVT modules collectively generate about 350 W, which is dissipated through chilled water at 8° C.

Signals from the silicon strips are interpreted by the ATOM (A Time-Over-Threshold Machine) integrated circuit. The chips have 128 input channels that are

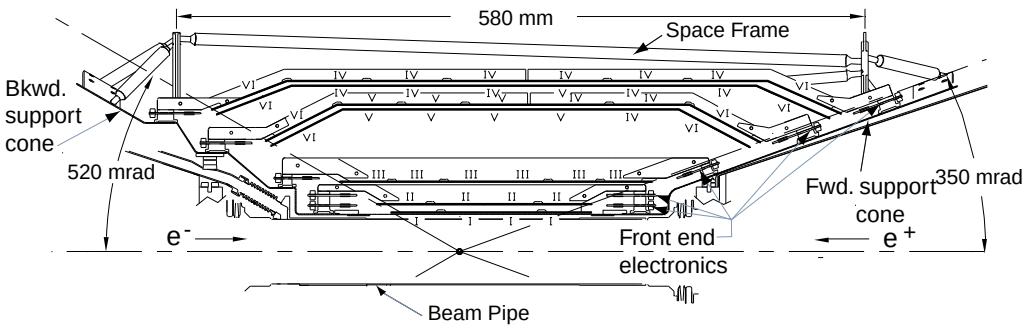

Figure 3.2: Longitudinal section of the SVT.

processed simultaneously, each corresponding to one silicon strip. Input data from the silicon strips are converted into output pulses whose width is logarithmically related to the collected charge. When the pulse amplitude reaches a certain threshold, a series of '1' bits are written into a 193-bit circular buffer for as long as the pulse remains above threshold, one bit for each 15-MHz clock tick. A portion of this information may be read out within a configurable window. The location of the first 1-bit in the window is encoded as a 5-bit time stamp, while the number of consecutive 1's is counted and stored as a 4-bit time-over-threshold (ToT) count. The combination of ToT and time stamp is a "hit", up to four of which can be stored in a buffer for readout by the data acquisition system.

The SVT is located in an environment of high radiation, and therefore has the unique ability to abort the stored beams in PEP-II. Radiation can cause errors in the SVT data by flipping random bits, triggering a software configuration loss of the ATOM chips, and degrading the silicon modules over time. Because the SVT is central to *BABAR*'s primary physics goals, it has been instrumented with a protection

system. This was accomplished using a silicon PIN diode system and, later on, an alternate system of synthetic diamonds. The PIN diodes are arranged in a pattern like the odd numbers of a clock around the beam pipe. There are six on the front end of the detector and six on the back end. These have been in use since the start of data-taking in 1999. However, over time the middle-plane diodes have degraded due to high radiation. In 2003 two polycrystalline chemical vapor deposition (pCVD) diamonds were installed in the middle plane on the backward side. These diodes and diamonds comprise the SVT radiation protection system (SVTRAD).

The SVTRAD system can abort the beams due to either an acute, fast increase in radiation, or a chronic, slow accumulation. The former case has two types. If the dose rate is greater than 400 Rad/s the beams will be dumped. Alternatively, they can be dumped if the radiation is greater than 1.25 Rad/s and integrates to 5 Rad under this condition. For comparison, during stable beams, the average dose rate is 15–25 mRad/s. The abort thresholds are relaxed while the SVT voltage is off during beam fills. The slow abort system will activate if the radiation level remains above 100 mRad/s for ten minutes, allowing time for the beam operators to stabilize the environment. After nine years of running, the most-irradiated diode — backward-west mid-plane — had absorbed approximately 4 MRad out of its 5 MRad budget.

When calibrations are requested, the ATOM chips inject different values of test charges to record the response in the silicon. Both the gain and electronic noise are recorded. Thresholds may be adjusted depending on the results of these calibrations.

The SVT alignment is determined in two stages: local and global. In both cases, $e^+e^- \rightarrow \mu^+\mu^-$ events and cosmic rays are used. The local alignment algorithm considers the relative positions and orientations of each silicon module, while the global alignment treats the SVT as a rigid body and adjusts its position and orientation relative to the *BABAR* coordinate system. For local alignment, track fits are performed without any information from the DCH. The residuals of the hits are combined with information from an optical survey of the SVT to create a χ^2 for each module, which is minimized with respect to its position and orientation. This procedure is typically only done in the event of a magnet quench or detector access. Global alignment uses the track fit results from the DCH as well and attempts to minimize the difference in track parameters between the SVT-only and DCH-only fits. This procedure is done approximately every hour during data taking and is therefore called the rolling calibration.

The three inner SVT layers each have a typical spatial resolution of $15\,\mu$m for normally-incident tracks.The resolution for the two outer layers is about $40\,\mu$m. The vertex resolution of a fully-reconstructed B meson is $70\,\mu$m, meeting the design goal. As of October 2007 the average efficiency for active modules was 92%.

3.2.2 Drift Chamber

The purpose of the DCH is to measure charged-particle trajectories and ionization energy loss. The trajectories are helices oriented along the the magnetic field lines, with the radius of curvature determined by the transverse momentum and the

dip angle by the ratio of transverse-to-longitudinal momentum.

The DCH is a cylindrical chamber built around the SVT, with an inner radius of 23.6 cm and an outer radius of 80.9 cm. The 1-mm-thick inner wall is made of beryllium while the outer wall is a 9-mm-thick shell of carbon fiber. The chamber is about 2.8 m long, with endplates of 24-mm-thick aluminum.

A mixture of helium and isobutane gas in a ratio of 80:20 fills the DCH and provides a medium for charged particles to ionize as they pass through. The ionization signals are amplified and detected by wires drawn between the endplates along the axial direction. Wires are grouped into cells, consisting of a tungsten-rhenium sense wire at high voltage surrounded by six grounded aluminum field wires. Each cell has a transverse size of approximately $12 \times 19\,\mathrm{mm}^2$. Initially, the sense wire was held at 1960 V. This voltage and gas configuration provides a gain of 50,000. The operating voltage was lowered to 1930 V in 2001 to reduce discharges, then raised to 1945 V in 2007 to compensate for aging of the sense wires.

The 7104 cells are arranged into 40 layers. Every 4 layers of cells are grouped together into a superlayer. To determine longitudinal positions in the DCH, the wires in alternate superlayers are angled either along the axis (A), at $-$(52-76) mrad (U), or at +45-69 mrad (V) in a pattern of AUVAUVAUVA. Aluminum guard wires at 340 V are located at the superlayer boundaries to ensure that the gain in the boundary cells is close to the gain in the inner cells. Clearing wires at 825 V, also of aluminum, are located at the innermost and outermost layers to collect charges from photon conversions in the DCH wall material. A schematic of the first four superlayers is given in Fig. 3.3. The total material traversed by normally-incident

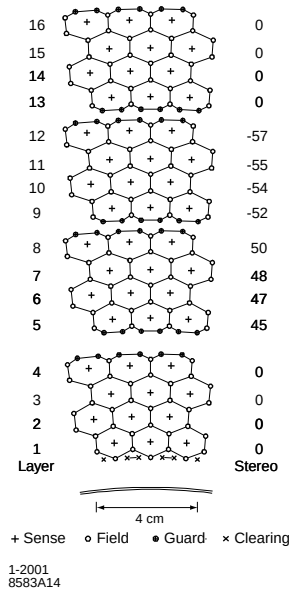

Figure 3.3: Transverse section of the first four superlayers of the DCH.

tracks is about 1% of a radiation length, the gas and wires making up 0.2%.

The DCH data acquisition electronics are located on the rear endplate of the chamber. Signals from the sense wires are delivered to the amplifier/digitizer boards and sampled at 15 MHz. The timing of a hit is determined with a phase-locked digital delay vernier, leading to a resolution of 1 ns on the leading edge of the signal. This information is processed with a time-to-digital converter (TDC) and stored as 4 bits. The deposited charge is sampled at 15 MHz with an analog-to-digital converter (ADC) and stored as 6 bits. Output signals are stored in a buffer for 12.9 μs. Upon request, the data acquisition system reads out 2.2 μs of data.

The data acquisition electronics produce calibration pulses in order to determine corrections and thresholds individually for each channel. To improve track reconstruction, a time-to-distance calibration is performed using samples of dilepton events. For each signal, a drift time is measured relative to the event-start time

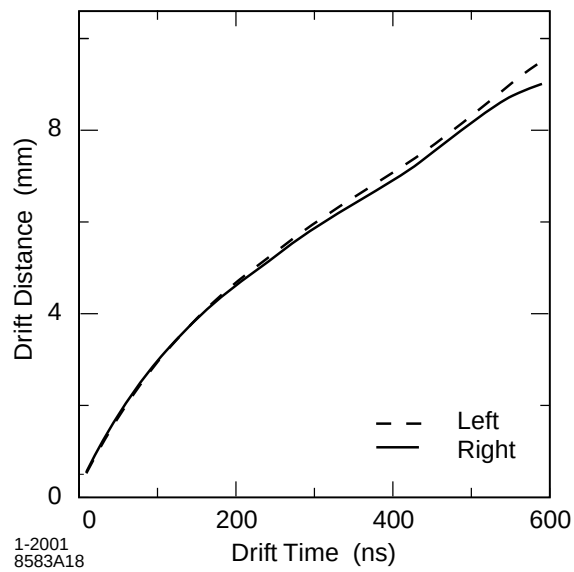

Figure 3.4: Drift time versus distance for tracks passing to the right and to the left of the sense wires in a single DCH layer.

t_0, determined by the trigger system (Sec. 3.6). The distance corresponding to the drift time is defined as the distance of closest approach between the wire and a fit to the track excluding the hit from the wire under consideration. Drift times and distances are averaged over all wires in a layer and the corresponding drift distance versus time relation is fit with a sixth-order polynomial, an example of which is given in Fig. 3.4. Corrections are made depending on the track's entrance angle to each cell. Tracks passing to the right and to the left of the sense wires are treated separately. The position resolution ranges from about $100\,\mu$m at $5\,$mm from the sense wire to $400\,\mu$m at $10\,$mm.

Each individual hit provides a measurement of $\mathrm{d}E/\mathrm{d}x$ based on the collected charge. The charge measurements are corrected based on gas gain calibrations, changes in gas temperature and pressure, signal saturation, non-linearities in $\mathrm{d}E/\mathrm{d}x$

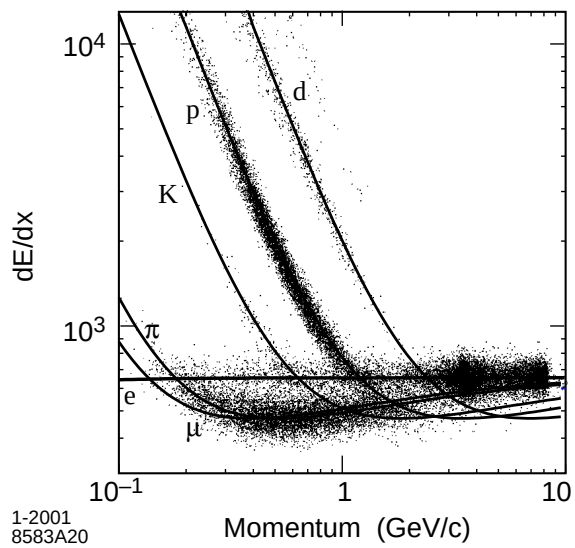

Figure 3.5: Energy loss versus momentum as measured in the DCH. The curves are the Bethe-Bloch predictions.

at large dip angles, and track entrance angle. The most probable $\mathrm{d}E/\mathrm{d}x$ for an entire track of up to 40 hits is calculated as the truncated mean of the lowest 80% of the individual $\mathrm{d}E/\mathrm{d}x$ measurements, determined from charge collected over a period of $1.8\,\mu$s. The typical $\mathrm{d}E/\mathrm{d}x$ resolution is approximately 7.5%. A plot of $\mathrm{d}E/\mathrm{d}x$ versus momentum for several types of charged particles is shown in Fig. 3.5, along with the predicted Bethe-Bloch curves. The differences between the particle types allow the DCH to perform particle identification at low momenta.

3.3 Particle Identification

The DCH and the Detector of Internally Reflected Cherenkov light (DIRC) are complementary for the purpose of particle identification. Distinguishing between charged pions and kaons is essential for B^0 flavor tagging as well as for reconstructing

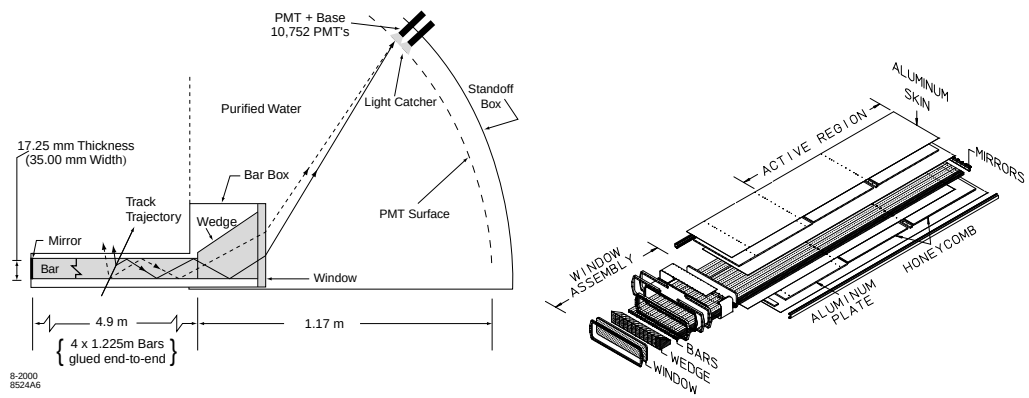

Figure 3.6: On the left, a schematic of the DIRC, longitudinal cross section. On the right, a schematic of the bar boxes.

rare B decays. Whereas the DCH's ability to distinguish the two falls quickly for momenta above $700\,\mathrm{MeV}/c$, the information from the DIRC becomes relevant for momenta in this range.

The DIRC is a new device for imaging rings of Cherenkov light produced in quartz bars. Instead of detecting the light near where it is produced, the DIRC transports the light through total internal reflection inside quartz bars located just outside the DCH, to be imaged in a standoff box on the backward end of the *BABAR* detector. The DIRC is based around the fundamental relation governing the emission of radiation by a charged particle traveling faster than the speed of light in a medium: $\cos\theta_c = 1/(n\beta)$, where θ_c is the Cherenkov angle, defined as the angle between the emitted photons and the direction of the track for a particle in a medium with index of refraction n. Because angles do not change upon reflection from a flat surface, the information of θ_c can be transported outside the *BABAR* barrel and detected elsewhere.

A schematic of the DIRC is shown in Fig. 3.6 (left). After the light is transported through the bars of fused, synthetic silica ($n = 1.473$) it passes through a wedge and into a standoff box full of $6\,\mathrm{m}^3$ of purified water ($n = 1.346$) instrumented with photomultiplier tubes (PMTs) along the far surface. Mirrors on the front ends of the bars reflect light back toward the PMTs. The wedge preserves photons that would otherwise be reflected at the silica-water boundary, and also allows a reduction in the size of the PMT array by ensuring that the photons are predominantly reflected away from the beamline upon leaving the bar box. The 4.9-m-long bars are each formed from four pieces that are 1.225 m long by 17 mm tall by 35 mm wide. A 9.1-mm-long wedge is attached to the end of each bar. The wedges' height ranges from 2.7 mm to 7.9 mm. Twelve bars, separated by 150 μm air gaps, are put together into a hermetically sealed bar box as seen in Fig. 3.6 (right). At the wedge end a 1-cm-thick fused silica window serves as the interface and seal to the water. In total, twelve bar boxes are placed around *BABAR*'s barrel, occupying 8 cm of radial space and 17% of a radiation length for normal tracks.

The light detection system consists of 10,752 PMTs of 2.9 cm diameter, arranged into 12 sectors. The operating voltage is 1.14 kV. A light catcher cone attached to the end of each PMT collects photons that might otherwise miss the active area. The quantum efficiency of the PMTs peaks at approximately 25% for 380-nm-light. A summary of the efficiencies of the various parts of the DIRC system is given in Fig. 3.7.

The DIRC data acquisition system is mounted outside the standoff box. Photon arrival times at the PMTs can be measured to a precision of 1.5 ns. Signals

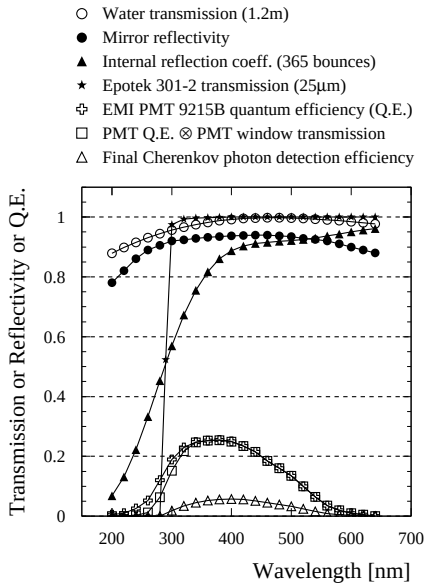

Figure 3.7: Efficiency of the various parts of the DIRC as a function of light wavelength.

from 64 PMTs are processed through a DIRC front-end board containing an 8-bit ADC to measure pulse height and four 16-channel TDCs to digitize photon arrival times. Events are pipelined to take into account the trigger latency. Upon receipt of a trigger, 600 ns of TDC data are read out. The pulse heights are useful for calibration of the PMT voltage, but are not necessary for data acquisition.

Calibrations use a light pulser system comprised of 12 LEDs mounted on the inner surface of the standoff box across from the PMTs. Pulses of 1 ns duration are used to measure arrival times in the PMTs. A typical calibration uses 65,000 pulses, which determine the arrival times to within 100 ps. PMT gains are measured by the ADC readout of the pulses. Collision data are also used to determine a global time delay. A set of 100,000 tracks are fit to the distribution of uncalibrated time

minus the expected arrival time for each PMT.

The DIRC performance is measured using samples of dimuon events and $D^0 \to K^-\pi^+$ events. In the former, the Cherenkov angle is found to be measured with a precision of 10.2 mrad and a time resolution of 1.7 ns. In the latter sample, kaons and pions can be distinguished at the 4.2σ level at momenta of $3\,\mathrm{GeV}/c$.

3.4 Calorimetry

All of the detector components discussed up to this point are used to measure properties of charged particles. The electromagnetic calorimeter (EMC) serves to measure photon energies, as well as to discriminate between electrons and other charged tracks. It is composed of 6580 thallium-doped cesium iodide crystals, which produce scintillation light in proportion to the energy of photons passing through them. The EMC is crucial to both of the analyses in this work, as it measures the energy of the emitted photon in $b \to s\gamma$ decays. Its electron discrimination is also critical for B flavor tagging.

At energies above 10 MeV, as photons and electrons pass through material, the dominant causes of energy loss are pair production and bremsstrahlung radiation, respectively. In certain materials, like cesium-iodide, these two effects can be exploited to produce a cascade of photons, which ends once the particle energies fall below a critical point (about 10.2 MeV for CsI). The addition of 0.1% thallium increases the light yield by an order of magnitude, and lengthens the emitted wavelength to better match the efficiency of the photodiodes used to detect the signals.

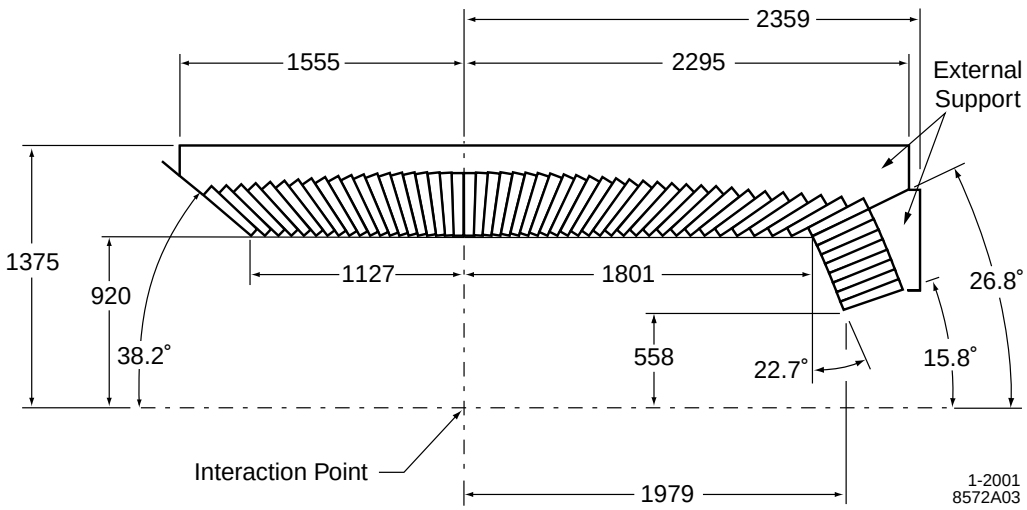

Figure 3.8: Longitudinal section of the EMC.

The EMC is composed of a barrel section with 48 rings of 120 crystals each, starting at an inner radius of 92 cm (Fig. 3.8). Due to the asymmetric collisions, most of the particles travel in the forward direction, so an EMC endcap of 8 rings, each with 80–120 crystals, covers polar angles down to 15.8°. The crystals themselves are tapered to allow dense packing, and are arranged in a projective geometry such that the crystal faces are oriented toward the interaction point. To reduce the number of particles that miss the crystals by traveling between them, the crystals are slightly non-projective with respect to the polar angle by 15–45 mrad. They remain fully projective in the azimuthal direction. Typical crystal faces are $4.7 \times 4.7\,\mathrm{cm}^2$ in the front and $6.1 \times 6.0\,\mathrm{cm}^2$ in the back, with lengths ranging from 29.6 cm (16.0 radiation lengths) in the backward direction to 32.4 cm (17.5 radiation lengths) in the forward direction.

Scintillation light is detected by two silicon photodiodes at the back of each crystal. These operate at 50 V with a quantum efficiency of 85% for the light pro-

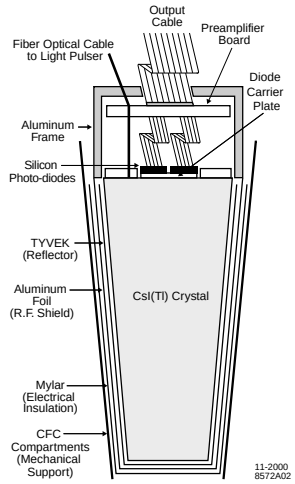

Figure 3.9: Schematic of the EMC crystals.

duced by the crystals: an average of 7300 photoelectrons per MeV at 565 nm. As shown in Fig. 3.9, each crystal is wrapped in several layers designed to keep light in the crystal, and to shield it from external electromagnetic fields; these wrappings have a total thickness of about 370 μm.

The EMC electronics systems are composed of 80 mini-crates, located along the outer rings of the barrel, and 20 mini-crates devoted to the endcap. Each photodiode on the crystals is connected to a preamplifier, which can optionally provide 32× amplification. Signals from both photodiodes are sent to a custom circuit for 10-bit digitization and optional amplification. The total amplification depends on the energy range: 256× for 0–50 MeV, 32× for 50–400 MeV, 4× for 0.4–3.2 GeV, and 1× for 3.2–13.0 GeV. Digitized events are placed in a pipeline, of which $\pm 1\,\mu$s is read out upon request.

There are two main types of calibrations: individual crystal energy calibration and cluster calibration, which takes into account energy loss and absorption.

Both types have different schemes for low and high energies. The low-energy crystal calibration involves irradiating Fluorinert to produce 6.13-MeV photons via $^{19}\mathrm{F} + \mathrm{n} \rightarrow {}^{16}\mathrm{N} + \alpha$, $^{16}\mathrm{N} \rightarrow {}^{16}\mathrm{O}^* + \beta$, $^{16}\mathrm{O}^* \rightarrow {}^{16}\mathrm{O} + \gamma$. The irradiated fluid is pumped through channels that run in front of the crystal faces so that the response in each crystal can be measured. At higher energies (3–9 GeV), samples of Bhabha (e^+e^-) scattering are used to relate the expected energy (based on polar angle) to the detector response. The calibration constrains the measured energy to match the prediction from the GEANT detector simulation (Sec. 4.4). Logarithmic interpolation is used in between the high and low energy ranges. The cluster calibration uses π^0 decays for energies less than 800 MeV by requiring the measured diphoton invariant mass to equal the π^0 mass. For higher energies so-called radiative Bhabha ($e^+e^- \rightarrow e^+e^-\gamma$) events are used, in which the photon energy can be determined from the initial e^+e^- system and the final-state e^+e^- momenta determined by tracking.

The calibrations just discussed are used to determine energy resolution. At the lowest energy, the resolution is $\sigma_{\mathrm{E}}/E = 5.0 \pm 1.8\%$, while at high energy (determined by Bhabha events) it is $1.9 \pm 0.07\%$. At intermediate energies, the resolution is determined using π^0, η, and $\chi_{\mathrm{c1}} \rightarrow J/\psi\,\gamma$ decays. The following empirical relation is found:

$$\sigma_E/E = \frac{(2.32 \pm 0.30)\%}{\sqrt[4]{E(\,\mathrm{GeV})}} \oplus (1.85 \pm 0.12)\%,$$

where the first term is due to fluctuations in the number of photons produced and the second is an irreducible uncertainty due to light absorption, leakage, and calibration

uncertainties. The angular resolutions are found to be equal for the polar and azimuthal directions, as measured with π^0 and η decays to photons of approximately equal energy. Empirically,

$$\sigma_\theta = \sigma_\phi = \left(\frac{(3.87 \pm 0.07)}{\sqrt{E(\,\mathrm{GeV})}} \oplus (0.00 \pm 0.04) \right) \mathrm{mrad}.$$

The π^0 mass is measured with a resolution of $6.9\,\mathrm{MeV}/c^2$ for $B\overline{B}$ events.

Electrons are identified by the ratio of their energy, measured in the EMC, to momentum, measured in the tracking system (Fig. 3.10). The performance of this variable is evaluated using radiative Bhabha events and $e^+e^- \to e^+e^-e^+e^-$, while the probability to identify a pion as an electron is measured using $K_S^0 \to \pi^+\pi^-$ and three-prong τ decays. For a tight set of selection criteria in the momentum range between 0.5 and 2 GeV/c, the electron efficiency is 94.8% with a pion misidentification rate of 0.3%.

3.5 Muon Detection

The outermost subsystem of *BABAR* serves to contain the magnetic flux produced by the 1.5-T superconducting solenoid, while acting as a detection system for muons and neutral hadrons. It consists of steel interleaved with detectors. Originally the detectors were resistive plate chambers (RPCs); in 2004 and 2006 the barrel part of the system was upgraded to limited streamer tubes (LSTs).

Both RPCs and LSTs operate on the basis of charged particles ionizing a gas and creating a discharge (streamer) as they pass through the high voltage of a module. The range of the discharge is limited by electric insulators so that the

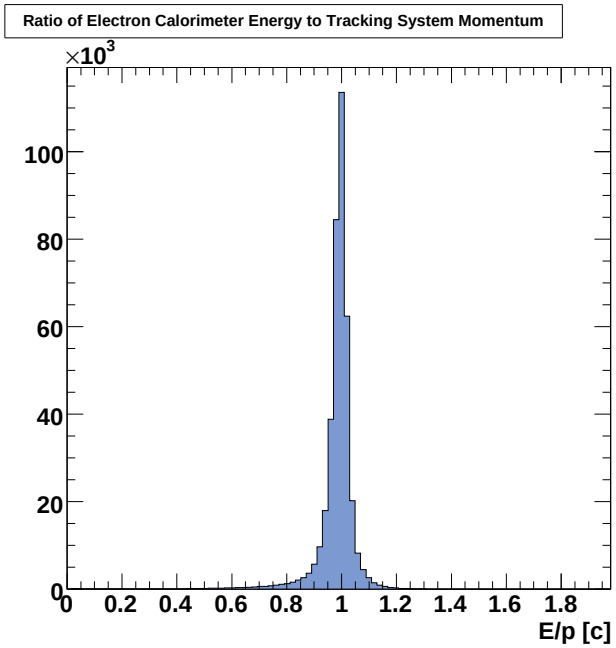

Figure 3.10: Distribution of electrons' energy (E) to momentum (p) in a sample of $e^+e^- \rightarrow e^+e^-\gamma$ events.

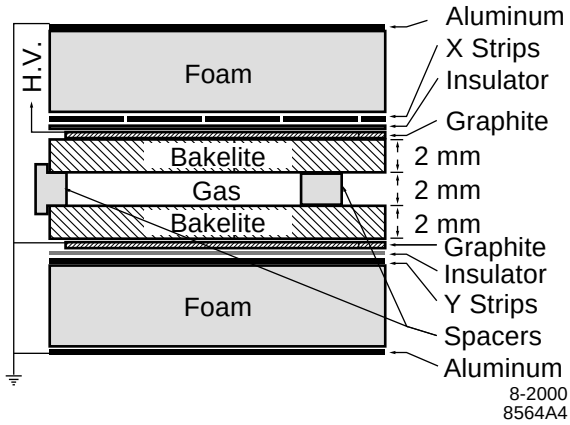

Figure 3.11: Schematic of an RPC.

field is effectively shut off in a small part of the detector, allowing for low deadtime with a large particle flux. The *BABAR* RPCs are composed of "sandwiches" of Bakelite and graphite, with a 2-mm-gap in between containing a mixture of 56.7% argon, 38.8% freon, and 4.5% isobutane. A schematic is given in Fig. 3.11. Two-dimensional readout is accomplished with orthogonal aluminum strips on either side of the module, with signals picked up through capacitive coupling.

LSTs are tubes of polyvinyl chloride, with a cross section of $15 \times 17\,\mathrm{mm}^2$ and a length of 38 cm. Four tubes are connected end-to-end and then placed in groups of 7 or 8 to make a module. The inner surface of the ube is coated with graphite to act as a cathode, while a central 100-μm-thick anode wire supplies high voltage. The tube is filled with 89% carbon dioxide, 8% isobutane, and 3% argon. Two-dimensional readout is given by the index of the anode wire and by capacitively-coupled aluminum strips running along the bottom of the tubes, perpendicular to the wires. In both the original and upgraded systems, the total active area of the detector is of order $2000\,\mathrm{m}^2$

An overview of the IFR layout is given in Fig. 3.12. It consists of a barrel component, segmented into six ϕ regions and three z regions, and two endcaps, segmented into east and west sides with six vertical regions. The IFR is composed of 870 tons of low-carbon steel. The steel is radially segmented, with the feature that the segmentation width varies as one moves outward from the interaction point. The innermost steel segments are 2 cm thick, increasing to 10 cm for the outermost ones. This was done as Monte Carlo studies indicated that it would improve muon and K_L^0 identification. The barrel IFR originally had a total of 19 layers interleaved

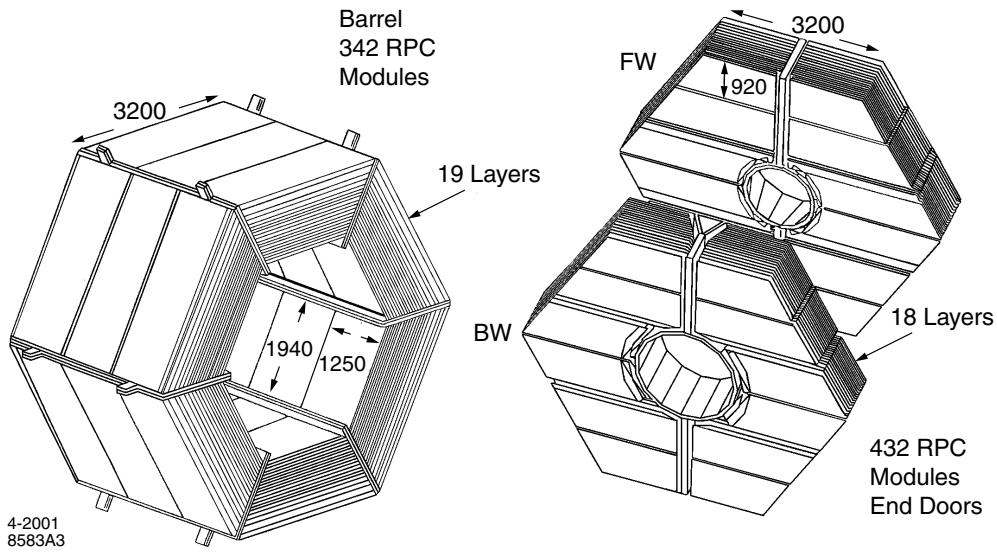

Figure 3.12: Schematic of the IFR layout.

with RPCs, and the endcaps had 18 layers each, leaving 65 cm and 60 cm of steel in the barrel and endcaps, respectively.

The RPC modules have an area of up to $3 \times 1\,\mathrm{m}^2$; two or three modules may be joined together to make larger chambers. Readout strip widths range from 19.7-32.8 mm in the barrel. The modules are typically held at a potential of 7600 V. Due to problems in the curing process of the linseed oil used to smooth out the Bakelite surfaces, many RPC modules degraded during the first several years of running. This led to increased noise in the modules and reduced performance. All of the barrel RPCs were replaced with LSTs to mitigate this problem. In the process, six layers were filled with brass in order to increase the thickness and improve pion rejection without changing the magnetic properties of the IFR. The LST modules have readout strip widths of 35 mm. The modules are held at an operating voltage of 5500 V.

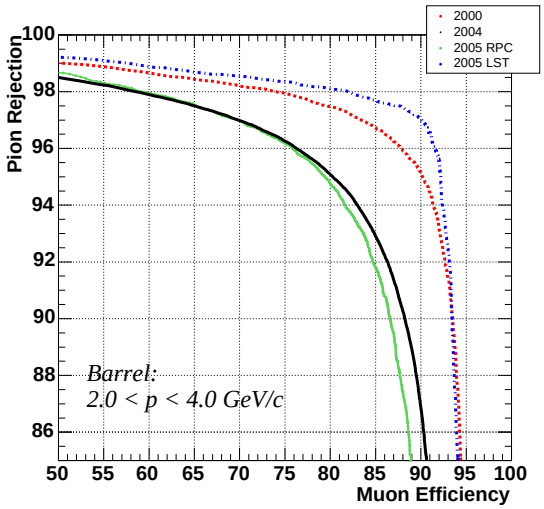

Figure 3.13: IFR pion rejection rate (%) as a function of muon identification efficiency (%) for several periods of the IFR's lifetime.

The IFR data acquisition system is composed of 3300 front-end cards (FECs), each of which serve 16 readout channels. The FECs read in signals from the detector and set a bit indicating whether a particular strip was above a configurable threshold. The signals are collected in eight front-end crates outside the detector that buffer strip hits, record timing information, and inject test pulses for calibration. Hits are stored in a first-in-first-out card that runs at the system clock frequency of 59.5 MHz.

Weekly calibrations track module efficiencies as a function of applied voltage based on cosmic ray data. The efficiency at the running voltage is stored in a database and used during event reconstruction.

The pion rejection versus muon efficiency during several periods of the IFR's lifetime is given in Fig. 3.13. More recently, for a tight set of particle identification criteria, the muon efficiency for tracks with center-of-mass momenta between 1.5

Table 3.1: Relative rates of different event types passing through the entire trigger system.

Event Type	Fraction of Output
Hadrons, $\tau\tau$, $\mu\mu$	13%
QED, 2-photon events	11%
Unidentified e^+e^- background	15%
Beam-induced background	21%
Calibration e^+e^-	25%
$\gamma\gamma$, $e^+e^-\gamma$	8%
Random triggers, cosmic rays	2%
Other diagnostics	6%

and 3.0 GeV/c is 90% with a pion fake rate of 2%.

3.6 Triggering

The *BABAR* trigger system is responsible for quickly selecting interesting events to record among the thousands of interactions that happen each second. At design luminosity ($3\times10^{33}\,\mathrm{cm}^{-2}\mathrm{s}^{-1}$), the total recorded event rate was about 120 Hz, though by 2007 it had increased to about 300 Hz during data-taking at the $\Upsilon(4S)$ resonance. The relative amounts of various types of events are given in Tab. 3.1.

There are two components to the system: Level 1, which is implemented in hardware and operates on the order of microseconds, and Level 3, which is run as software across a farm of 32 nodes, each taking several milliseconds to make the final decision.

3.6.1 Level 1

The first level of triggering uses basic, coarse-grained information from the DCH, EMC, and IFR. The three systems are largely orthogonal in the sense that they each detect different types of particles. Information from these systems is shipped to the global trigger (GLT) every 134 ns, where a trigger decision is made within 12.9 μs.

Information from the DCH is summarized into three so-called ϕ-maps: one for short tracks, long tracks, and combined discrimination of transverse momentum and distance of closest approach along the beam axis (z_0). Each bit in a ϕ-map corresponds to one of 16 regions divided by azimuthal angle. If the bit is active, then a L1 trigger object was detected in that region. The trigger objects are general, such as a DCH track reaching the outermost superlayer.

The creation of DCH trigger objects begins with the track segment finder, which samples the DCH signals every 269 ns. It only considers superlayers as a whole, not the individual layers. Weights are assigned to DCH hits depending on their timing and whether they are in agreement with hits in adjacent superlayers. If good agreement is found, a track segment is formed. Segments are shipped to the binary link tracker (BLT) every 134 ns and to the z and p_T discriminator (ZPD) every 269 ns. The BLT is responsible for linking segments into tracks and classifying them to create the trigger objects. The ZPD uses information from the axial superlayers to determine whether tracks are consistent with having momenta above a configurable threshold, based on a lookup table. Data from the stereo layers are used in a quick

fit to determine z_0 with a precision of about 4 cm.

The EMC trigger system divides the detector into 40 ϕ regions in both the barrel and endcap. The spread in θ is configurable. In each tower of crystals corresponding to a ϕ-θ region, crystal energies above 20 MeV are summed and sampled every 269 ns. Trigger objects in the form of ϕ-maps are created depending on the tower energy and its location in θ. For example, one object represents a tower in the forward endcap with energy greater than 100 MeV. Before the creation of the ϕ-maps, pairs of ϕ regions are grouped together to make 20-bit maps, except in the backward part of the barrel, where groups of four are combined into 10-bit maps.

Triggering on objects in the IFR is simpler. The system is divided into 10 sections: the six barrel regions, and 2 regions for each of the endcaps. Eight layers in each sector are selected as trigger layers, and a signal is counted if it is present in at least four within a window of 134 ns. Trigger objects are created depending on where signals were found: for example, an object corresponding to two back-to-back signals in the IFR barrel.

The GLT system synchronizes the input from each of the three subsystems and provides basic matching in ϕ between objects from different systems. The GLT can be configured to combine trigger objects using logical operations ("AND", "OR", etc.) for up to 24 trigger output lines. The system also determines the L1 trigger time from an average of the timing distribution of the highest-priority trigger, achieving a root-mean-square resolution of 52 ns for hadronic events. The L1 output rate at design luminosity was about 1 kHz, though by 2007 it was typically about 3.5 kHz. The overall L1 efficiency for $B\overline{B}$ events is greater than 99.9%, greater

than 98% for $e^+e^- \to q\overline{q}$ ($q = \{u, d, s, c\}$) continuum, and just under 95% for $\tau^+\tau^-$ events.

3.6.2 Level 3

The Level 3 (L3) software trigger has access to all of the event information. It is based around a set of scripts, each of which produces a single pass/fail bit. The results of one or more scripts are logically combined to produce the L3 output lines.

In the L3 DCH tracking algorithm, track segments from L1 are used to determine the start time t_0 of the event, based on the mean t_0 from the individual segments (ignoring outliers). The resolution is 1.8 ns for Bhabha events and 3.8 ns for hadronic events. A lookup table method is then used to combine track segments into track candidates. The candidates are fit to a five-parameter helix using the hit information from the DCH.

The L3 EMC clustering algorithm also uses a lookup table method to turn lists of crystals into clusters. It starts with crystals of energy greater than 20 MeV within 1.3 μs of the event time. Based on the lookup table, groups of crystals are combined into clusters if the cluster energy is greater than 100 MeV. The energy-weighted centroid, number of crystals, lateral moment and average time of the cluster are calculated for use in the scripts.

The purpose of the L3 scripts is to identify interesting events based on high-level, physics-oriented information. DCH filters choose events with at least one high-p_T track or two lower-p_T tracks originating in the interaction region. In the

EMC, interesting events have either high-energy clusters, or high cluster multiplicity. Both systems are used to reject the dominant background from Bhabha events: the DCH-based veto relying on detection of the electron and positron tracks, and the EMC-based one relying on the ratio of energy to momentum.

After passing through both levels of triggering, $B\overline{B}$ events are selected with an efficiency greater than 99.9%. Quark continuum events have an efficiency over 95%, while $\tau^+\tau^-$ events are 92.0% efficient. In each case, the design goal was met. At design luminosity, approximately 13% of the L3 output rate is composed of events suitable for physics analysis, while 40% is used for calibration and diagnostic purposes. The remainder is made up of background events.

Chapter 4

Offline Analysis Framework

A major infrastructure is required to transform the raw data signals described in the previous chapter into data that may be manipulated for analysis. In this chapter I describe the basic event reconstruction algorithms that provide access to information on tracks and neutral clusters. I also describe tools like B flavor tagging and B counting, which are necessary for the analyses presented in this work. Finally, I briefly discuss how *BABAR* simulates data in order to study specific types of signal and background processes.

4.1 Event Reconstruction

Within a few hours after data are recorded by *BABAR*, they pass through prompt calibration (PC) and rolling calibration processes that implement many of the calibrations discussed in the previous chapter. Next, data are sent to the Tier-A computing center at the University of Padova, Italy for offline event reconstruction (ER). The flow of data is given in Fig. 4.1. The next few sections describe the ER algorithms used to turn raw measurements into reconstructed tracks and neutral clusters. The processed data are then stored in ROOT collections for *BABAR* analysts. These processes typically run within 48 hours, yielding a high turnaround rate between data acquisition and the availability of data for physics analyses.

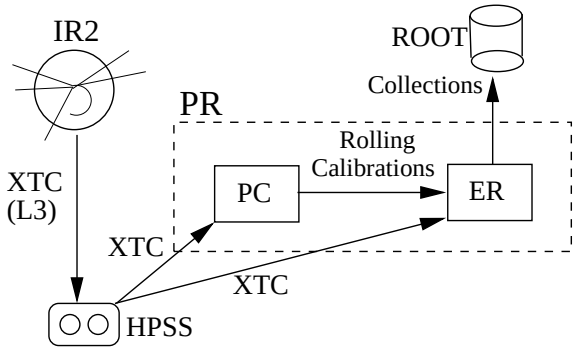

Figure 4.1: Schematic of the data path from its origin in the *BABAR* detector at PEP-II interaction region 2 (IR2) as raw data (XTC format). It is stored on tape (HPSS) and also sent for offline prompt reconstruction (PR). Processed data are stored as ROOT files.

4.1.1 Track Reconstruction

Charged particles moving in the presence of a uniform magnetic field travel in helices. These trajectories can be parameterized by five quantities: the distance of closest approach to the origin in the x-y plane (d_0), the azimuthal angle of that point (ϕ_0), the distance of closest approach in the z direction (z_0), the transverse momentum (p_T), and the angle between the transverse and longitudinal momentum,

the dip angle (λ). The parameters are related to the positions and momenta by

$$
\begin{aligned}
x &= r\sin\phi - (r + d_0)\sin\phi_0 \\
y &= -r\cos\phi - (r + d_0)\cos\phi_0 \\
z &= z_0 + l\tan\lambda \\
p_x &= p_T\cos\phi \\
p_y &= p_T\sin\phi \\
p_z &= p_T\tan\lambda,
\end{aligned}
\tag{4.1}
$$

where $r = p_T/qB_z$ and $\phi = \phi_0 + l/r$, with l being the parameter that varies along the helix. The variables q and B_z are the particle's electric charge and the axial strength of the magnetic field.

Track reconstruction begins with the output of the Level 3 DCH tracking algorithm. A helix fit is performed using a Kalman filter method [44] that takes into account measurement uncertainties as well as uncertainties due to multiple scattering and energy loss in the detector material traversed by the particle. Several passes are made through the DCH hit list to add hits that may have been missed in the original algorithm. Afterwards, trajectories are extrapolated into the SVT, where track segments from the SVT standalone tracking are added, based on the hit residuals along the segment and the number of SVT layers traversed. Finally, the full trajectory is refit using information from both the SVT and DCH. Leftover segments in the SVT are also refit to create SVT-only tracks.

To assess the track-reconstruction performance, cosmic ray muons passing though both the SVT and DCH near the interaction point are selected. The two

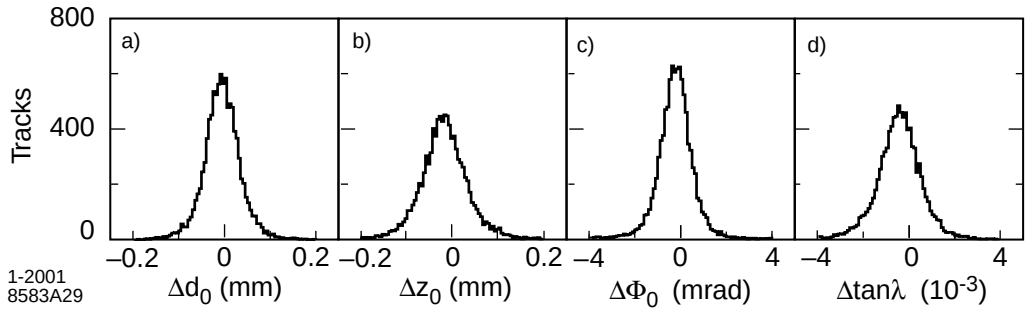

Figure 4.2: Difference between track parameters of two halves of cosmic ray muons, (a) Δd_0, (b) Δz_0, (c) $\Delta\phi_0$, (d) $\Delta \tan\lambda$.

halves of each muon track are fit separately, and the difference between the measured parameters in each half is taken as the resolution (Fig. 4.2). The resolutions are found to be

$$\sigma_{d_0} = 23\,\mu\text{m} \qquad \sigma_{\phi_0} = 0.43\,\text{mrad}$$

$$\sigma_{z_0} = 29\,\mu\text{m} \qquad \sigma_{\tan\lambda} = 0.53 \times 10^{-3}.$$

The transverse momentum resolution is found to scale linearly with the transverse momentum (Fig. 4.3). It can be parameterized by

$$\sigma p_T/p_T = (0.13 \pm 0.01)\% \cdot p_T + (0.45 \pm 0.03)\%.$$

Track reconstruction efficiency may be determined separately for the SVT and DCH because both systems can perform standalone tracking. The DCH efficiency is calculated as the ratio of tracks reconstructed in the DCH to tracks reconstructed in the SVT (within the DCH acceptance). Figure 4.4 shows the DCH track reconstruction efficiency at the nominal 1960 V and for 1900 V. The SVT

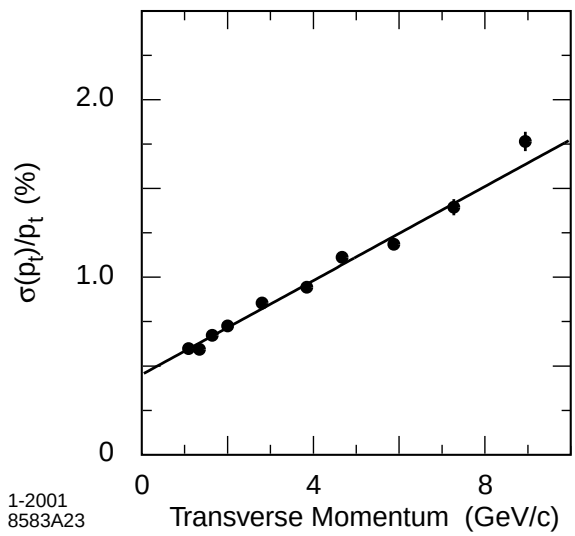

Figure 4.3: Resolution of transverse momentum of cosmic ray muons as a function of transverse momentum.

reconstruction efficiency performance is best-characterized by reconstruction of low-momentum particles. This can be measured in samples of $B\overline{B}$ events containing D^* decays in which a soft pion is emitted. The Monte Carlo simulation reproduces the data well, and is used to determine the SVT track reconstruction efficiency, shown in Fig. 4.5.

It should be noted that data processed after July 2006 received an extra pass of tracking algorithms, collectively known as `TrkFixUp` [45]. Due to the timing, the data used for the $B^0 \to K_S^0\pi^0\gamma$ analysis had this improvement, while the data used for $B \to K\phi\gamma$ did not. The algorithms use sophisticated pattern recognition to add or subtract hits to improve track reconstruction while also improving rejection of background or poorly-measured tracks.

Any difference in track reconstruction efficiency between positively and negatively-charged particles will bias *CP* asymmetry measurements. This is of particular con-

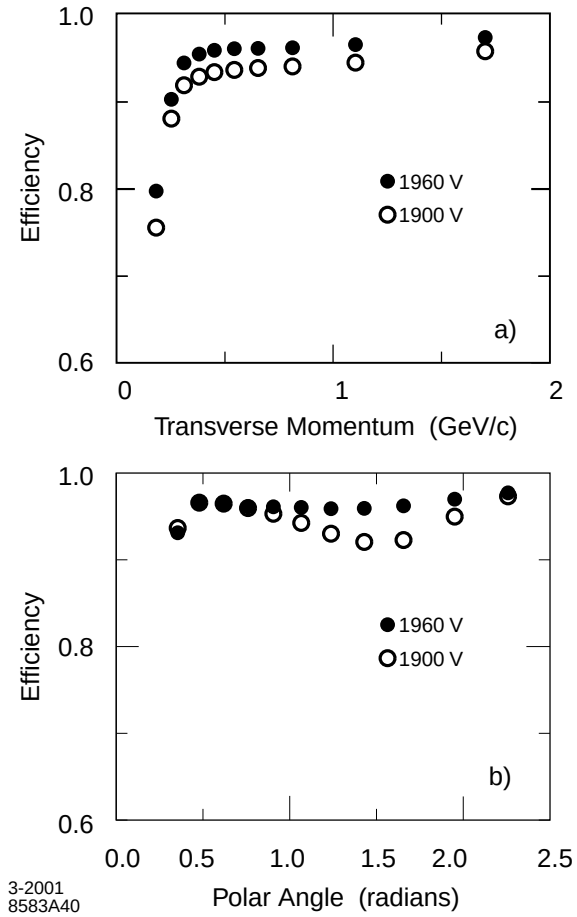

Figure 4.4: DCH track reconstruction efficiency relative to the SVT for two operating voltages as a function of transverse momentum (a) and polar angle (b).

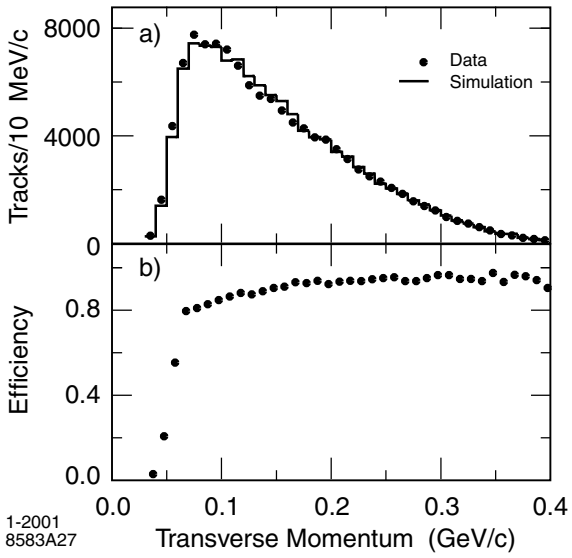

Figure 4.5: SVT low-momentum track reconstruction performance. The top plot (a) shows the soft pion momentum from $D^{*+} \to D^0\pi^+$ in $B\overline{B}$ data (after background subtraction) compared to $B\overline{B}$ Monte Carlo simulation. The bottom plot (b) shows the Monte Carlo reconstruction efficiency of the soft pion.

cern for kaons because K^+ and K^- mesons have different interaction cross sections with the nucleons making up the *BABAR* detector [7]. For example, K^+ mesons at $3.0\,\mathrm{GeV}/c$ interact with protons and neutrons with cross sections of $17.2 \pm 0.2\,\mathrm{mb}$ and $17.8 \pm 0.7\,\mathrm{mb}$, respectively; for K^- the cross sections are $27.4 \pm 0.3\,\mathrm{mb}$ and $22.4 \pm 0.7\,\mathrm{mb}$. For pions, there are data for $2.47\,\mathrm{GeV}/c$ π^+ and π^- on deuterons with cross sections of $62.9 \pm 0.8\,\mathrm{mb}$ and $63.2 \pm 1.0\,\mathrm{mb}$, respectively.

The effects of detector asymmetries were studied in detail in *BABAR*'s analysis of *CP* violation in $B^0 \to K^+\pi^-$ and $B^0 \to \pi^+\pi^-$ [46]. For kaons, the possible bias is determined with a simulated Monte Carlo (MC) sample of $B^0 \to K^+\pi^-$ decays, generated with no inherent direct *CP* asymmetry. The measured asymmetry is found to be $(-0.49 \pm 0.05)\%$ for signal and $(-0.45 \pm 0.40)\%$ for background (statistical uncertainties only). These are consistent with each other, and they agree with a calculation using the kaon-nucleon cross sections above, yielding $(-0.54 \pm 0.02)\%$ based on the detector material composition (the uncertainties are only those of the cross sections). In the fit to data, the asymmetry of the background is found to be $(-1.1 \pm 0.4)\%$.

To summarize, the central value of the asymmetry is taken to be -0.50% based on the MC and an independent calculation. The conservative lower bound on the magnitude is taken to be half the value, 0.25%. The difference of 0.60% between the central value and the asymmetry in the data background is taken as the upper bound. Therefore, a bias correction of $+0.5^{+0.6}_{-0.3}\%$ is applied to $A_{CP}(B^0 \to K^+\pi^-)$.

In the study of $B^0 \to \pi^+\pi^-$, no significant bias is found in the MC, nor is it expected based on pion-nucleon cross sections. The accuracy given by the MC

statistics on $A_{CP}(B^0 \to \pi^+\pi^-)$ is 0.4%, which is taken as a conservative uncertainty. These corrections and uncertainties show that the *CP* asymmetry induced by the detector is no more than 1%.

4.1.2 Particle Identification

The goal of the particle identification algorithms is to distinguish between the long-lived particles detected by *BABAR*: electrons, muons, pions, kaons, and protons. Several methods using the same information provide varying levels of performance. Simple cuts, parameterized likelihood functions, or artificial neural networks may be used. The input information consists of the $\mathrm{d}E/\mathrm{d}x$ energy loss in the tracking system, the Cherenkov angle θ_c from the DIRC, the number of Cherenkov photons, the amount and profile of energy deposited in the EMC, and cluster depth and shape in the IFR. Not all of these data are necessarily available for each track.

Electrons are primarily identified by the ratio of their energy to momentum, which should peak near 1. The $\mathrm{d}E/\mathrm{d}x$, θ_c, and EMC shower shape are also required to be consistent with the electron hypothesis. For muons, the number of interaction lengths traversed, mainly in the IFR, provides the greatest discrimination. Muons should also produce a signal in the EMC consistent with a minimum ionizing particle. Muon efficiency and electron fake rate for a tight muon selector are given in Fig. 4.6.

Kaons, pions, and protons are distinguished primarily by their energy loss, Cherenkov angle, and number of Cherenkov photons. Figure 4.7 shows the kaon

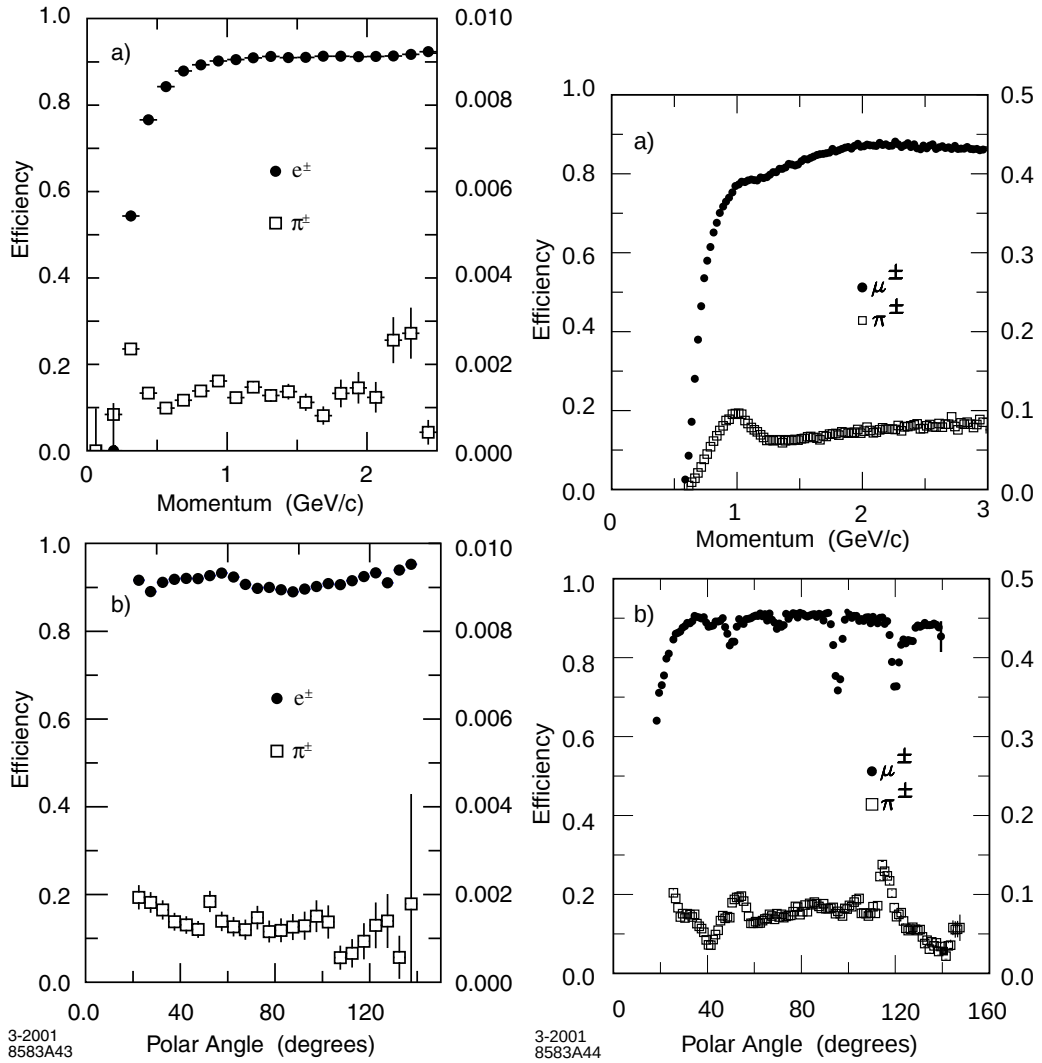

Figure 4.6: Plots for electron (left) and muon (right) efficiency and pion fake rate as functions of momentum (top) and polar angle (bottom). The left scales are the efficiency while the right scales give the fake rates. The electron plots are created using tight identification criteria, while the muon plots use loose criteria.

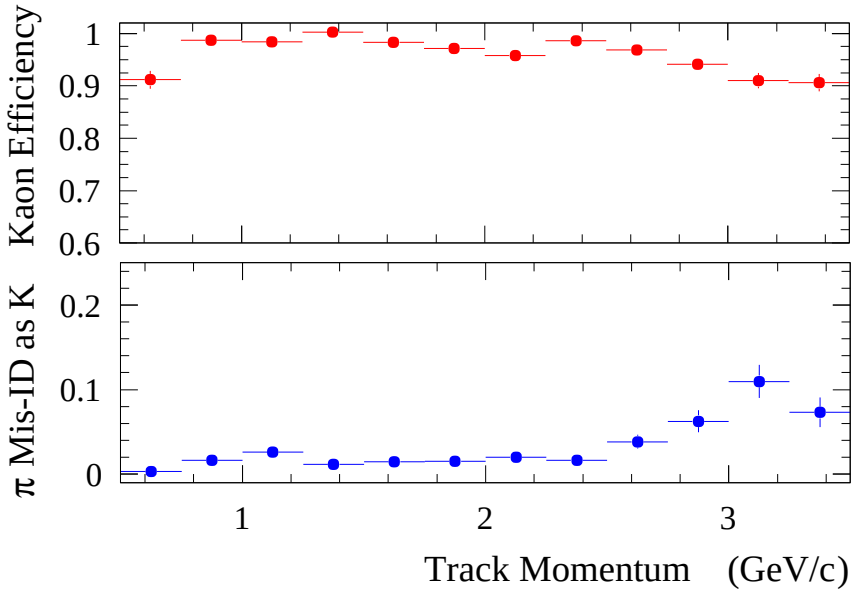

Figure 4.7: Charged kaon efficiency (top) and pion fake rate (bottom) as a function of momentum in $D^0 \to K^-\pi^+$ processes from D^* sample.

efficiency and pion fake rate for charged kaon candidates from $D^0 \to K^-\pi^+$ processes in a D^* sample. Additional particle identification performance data related to the kaons used in the $B \to K\phi\gamma$ analysis and to the B^0 flavor-tagging algorithm will be discussed in those sections.

4.1.3 Neutral Reconstruction

EMC objects are identified as clusters of deposited energy. Each local maximum of energy inside a cluster is identified as a bump. Cluster reconstruction starts with a seed crystal of at least 10 MeV. Adjacent crystals are added to the cluster if their energy is at least 1 MeV, or if they have a neighboring crystal of at least 3 MeV. For each local maximum of energy within a cluster, a bump is defined. Its energy is determined using an iterative algorithm that assigns a weight to the energy of each of the component crystals. The weighting algorithm takes into account the distance between the crystals and the bump centroid, relative to the Molière radius of the CsI crystals (3.8 cm). After each iteration, the centroid of the bump is recalculated, and the procedure repeats until the centroid is constant within 1 mm. Due to the non-projectivity of the crystals, the position is corrected by ± 2.6 mrad for bumps on the forward (+) and backward (−) sides of the detector. Bumps are identified as charged if a track helix may be extrapolated to intersect with the bump at the EMC surface. Otherwise, the bumps are neutral.

Besides the cluster energy, the shower shape is also useful. This is quantified using two quantities known as the lateral moment (LAT) and second moment. The LAT is defined as the ratio of (a) the sum of the energies E_i of all but the two most energetic crystals, weighted by the square of their distance to the center of the cluster r_i, and (b) the sum of all energies in the cluster, weighted by the square of the length scale r of the crystals, 5 cm:

$$\mathrm{LAT} = \frac{\sum_{i=3}^{N} E_i r_i^2}{\sum_{i=1}^{N} E_i r^2}. \tag{4.2}$$

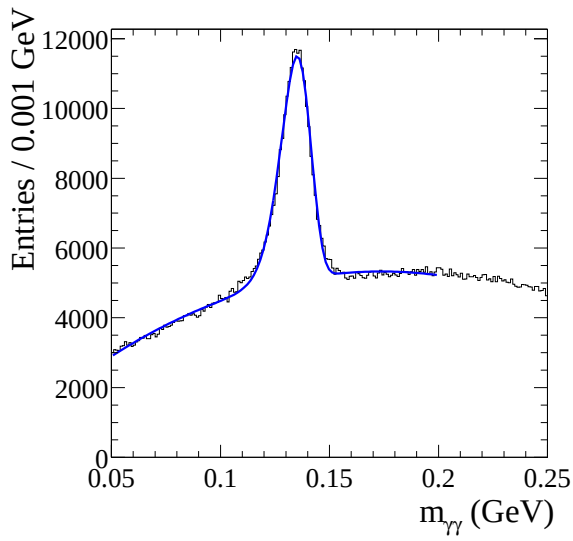

Figure 4.8: Diphoton invariant mass around the π^0 peak in $B\overline{B}$ events.

The second moment is the ratio of (a) the sum of the energies E_i of the crystals, weighted by the square of their angular distance α from the center of the cluster, and (b) the cluster energy:

$$2^{\text{nd}} \text{ Moment} = \frac{\sum_{i=1}^{N} E_i \alpha^2}{\sum_{i=1}^{N} E_i}. \tag{4.3}$$

These are important as electromagnetic interactions tend to be more concentrated than hadronic interactions.

Photon reconstruction performance can be characterized by the π^0 mass peak in $B\overline{B}$ events. Figure 4.8 shows the reconstructed invariant mass of two photons, one of energy greater than 30 MeV and the other of energy greater than 300 MeV. The peak position of 135.1 MeV/c^2 is stable within 1% over the entire range of photon energies. The width of the peak, corresponding to the mass resolution, is 6.9 MeV/c^2.

Besides photons, K_L^0 mesons may be reconstructed using a combination of

EMC and IFR information. Neutral EMC clusters of energy between 200–2000 MeV and polar angle $|\cos\theta| < 0.935$ are considered as K_L^0 candidates if, when combined with other neutral clusters of energy greater than 30 MeV, do not create π^0 candidates with mass $100 < m_{\pi^0} < 150\,\mathrm{MeV}/c^2$. Neutral IFR clusters may be identified as K_L^0 mesons. To reduce beam-generated backgrounds, only those clusters with polar angle $-0.75 < \cos\theta < 0.93$ are accepted. Clusters beginning in the outer 25% of the forward IFR endcap are vetoed. To reduce backgrounds from charged hadrons, IFR K_L^0 candidates are rejected if they lie near a charged EMC cluster within ± 350 mrad in polar angle and -750 (-300) to $+300$ ($+750$) mrad in azimuth for positively (negatively) charged tracks. Based on a sample of $e^+e^- \to \phi\gamma$ events, with $\phi \to K_S^0 K_L^0$, the K_L^0 reconstruction efficiency was found to be about 60% at the start of data taking in 1999, dropping to 52% in 2004 due to degredation of the RPCs.

4.2 B Tagging

Determining the flavor of a B^0 meson in the event is essential to time-dependent CP violation measurements. At *BABAR* this is accomplished by exploiting correlations between the charges of final-state particles and the flavor of the original B^0 or $\overline{B}^0$ meson. In all cases, tagging begins with the CKM-favored $b \to c$ transition.

In the case of a $b \to c\ell\nu$ transition, the lepton charge carries the same sign as the tag-side b quark charge. If instead the B decays hadronically, then the b flavor may be determined from the $b \to c \to s$ cascade in which a final-state charged

kaon carries the same sign as the b quark charge. Additional information may be exploited if a D^* meson is produced in the cascade: its decay could include a charged soft pion with the opposite sign of the b charge. Furthermore, if the final state of the D^* decay includes a charged kaon, then its charge will be opposite the soft pion. Other less-reliable, but still useful, processes are discussed below.

There are a total of six categories, each with a different level of performance.They are known as Lepton, Kaon 1, Kaon 2, Pion, Kaon-Pion, and Other. A seventh category indicates that no flavor tag could be determined. The categories are characterized by their average efficiencies ϵ, mistag probabilities w, and the flavor differences: $\Delta\epsilon = \epsilon_{B^0} - \epsilon_{\overline{B}^0}$ and $\Delta w = w_{B^0} - w_{\overline{B}^0}$. The effective tagging efficiency is defined as $Q = \epsilon(1-2w)^2$ with a corresponding ΔQ.

Each tagging category is implemented as one or more artificial neural networks (NN). The outputs of the individual NNs are used as input to the final flavor tag NN, which produces continuous output in the range $[-1, 1]$, the sign indicating either B^0 $(+)$ or $\overline{B}^0$ $(-)$ and the magnitude indicating the tagging category.

Lepton tags are produced by $b \to c\ell\nu$ decays, where the charge of the muon or electron has the same sign as the charge of the b quark. There are two separate NNs for electrons and muons, but they both use the same information calculated in the CM frame: the momentum of the lepton, the cosine of the angle between the lepton and the missing momentum of the event (roughly the direction of the neutrino), and the energy in the hemisphere defined by the virtual W, assuming the tag B was produced at rest.

Kaon tags come from cascade $b \to c \to s$ hadronic decays, in which the sign

of the kaon charge is the same as that of the b quark. Because multiple kaons can be produced, several charged and neutral kaon candidates are used. This NN accepts the kaon particle identification likelihood of the three best charged kaons in the event, the number of K_S^0 mesons detected, and the sum of the squares of the transverse momenta of these kaons.

Pion tags originate in $B^0 \to D^{*-}X^+$ decays, with $D^{*-} \to \overline{D}^0\pi^-$. The pion charge in this case is opposite the b quark charge. Because the pion momenta range from 40–250 MeV in the CM frame, the pions are designated as slow. The data used by the NN are the pion's CM momentum, its kaon likelihood, and the cosine of its CM angle with respect to the tag B thrust axis. The latter is relevant as the slow pion is produced primarily in the same direction as the other decay products.

Related to the slow pion tags are the pion-kaon correlation tags, in which the D^0 includes a charged kaon in its decay products. The kaon and pion charges are expected to be opposite. This tagger uses the kaon likelihood of the best kaon (with correct charge) and the output of the slow pion tagger. Because the kaon and pion should be in the same direction, the cosine of the CM angle between the kaon and pion is also used.

Finally, three additional taggers are used in the "other" category. They consist of tagging based on high-CM-momentum ($> 0.5\,\mathrm{GeV}/c$) tracks, correlations between slow pions and fast tracks, and a Λ tagger based on $b \to c \to s$ decays. The performances of the various sub-taggers, and their cutoff in the final NN output to designate the categories, are given in Table 4.1. Note that for the Lepton category, either the electron or muon subtagger must have an output magnitude greater than

Table 4.1: Tagging category definition and performance. See the text regarding the Lepton and Kaon 1 differences.

Category	NN Output	ϵ (%)	$\Delta\epsilon$ (%)	w (%)	Δw (%)	Q (%)	ΔQ (%)
Lepton	0.8–1.0	8.96 ± 0.07	-0.1 ± 0.2	2.8 ± 0.3	0.3 ± 0.5	7.98 ± 0.11	-0.14 ± 0.36
Kaon 1	0.8–1.0	10.82 ± 0.07	0.0 ± 0.2	5.3 ± 0.3	-0.1 ± 0.6	8.65 ± 0.14	0.02 ± 0.45
Kaon 2	0.6–0.8	17.19 ± 0.09	0.2 ± 0.3	14.5 ± 0.3	0.4 ± 0.6	8.68 ± 0.17	-0.09 ± 0.49
Pion	0.4–0.6	13.67 ± 0.08	0.0 ± 0.2	23.3 ± 0.4	-0.7 ± 0.7	3.91 ± 0.12	0.21 ± 0.34
Kaon-Pion	0.2–0.4	14.18 ± 0.08	-0.7 ± 0.3	32.5 ± 0.4	5.1 ± 0.7	1.73 ± 0.09	-1.10 ± 0.23
Other	0.1–0.2	9.54 ± 0.07	0.3 ± 0.2	41.5 ± 0.5	3.8 ± 0.8	0.27 ± 0.04	-0.23 ± 0.09
Total		74.37 ± 0.10	-0.2 ± 0.6			31.2 ± 0.3	-1.3 ± 0.9

0.7, while for the Kaon 1 tagger, the lepton subtaggers must both be below 0.7. The performance is evaluated on a data sample of self-tagging $B^0 \to D^{(*)-}\pi^+$, $B^0 \to D^{(*)-}\rho^+$, and $B^0 \to D^{(*)-}a_1^+$ decays.

4.3 B Counting

To measure branching fractions, one has to know how many B mesons have been produced at *BABAR*. This is determined by comparing data taken at the $\Upsilon(4S)$ resonance with data taken at 40 MeV below it. The number of "hadronic" events (described below) is compared with the number of $e^+e^- \to \mu^+\mu^-$ events to determine the total number of $\Upsilon(4S)$ mesons produced. This method assumes that the difference in the fraction of hadronic events is due to the resonance, and also that the $\Upsilon(4S)$ always decays to a $B\overline{B}$ pair. The method is described in detail in Ref. [47].

The number of $\Upsilon(4S)$ produced, N_Υ, is determined by

$$N_\Upsilon = N_{\text{on}} - M_{\text{on}} \cdot R_{\text{off}} \cdot \kappa, \tag{4.4}$$

where N_{on} is the number of on-resonance hadronic events, M_{on} is the number of on-resonance muon pairs, R_{off} is the ratio of hadronic to muon pair events in off-

resonance data, and $\kappa = 1.0000 \pm 0.0025$ to account for variations in the cross sections and efficiencies with the CM energy.

Hadronic events are required to pass both levels of either the DCH or EMC trigger algorithms. They must have at least three tracks that lie within the tracking volume $0.41 < \theta < 2.54$, each of which must create at least 12 DCH hits, have $p_T > 100\,\mathrm{MeV}/c$, and a distance of closest approach less than 3 cm from the beam spot in z and less than 1.5 cm in the transverse plane. The event-shape variable R_2 [48], which determines how isotropic the event is in the CM frame, must be less than 0.5. To reject beam backgrounds, the primary event vertex (determined using charged particles) must be within 0.5 cm of the beam spot in the transverse plane and within 6 cm in z. The total energy observed by the detector must be above 4.5 GeV. These criteria select about 95% of simulated $\Upsilon(4S) \to B\overline{B}$ events.

To select muon pair events, the two highest-momentum tracks in an event are examined. Each track must deposit less than 1 GeV in the EMC. In the CM frame, they must be back-to-back within 10°, must lie within the tracking volume ($|\cos\theta| < 0.75$), and must have a combined invariant mass greater than $7.5\,\mathrm{GeV}/c^2$.

The systematic uncertainty in the B counting is 1.1%, dominated by differences between the data and Monte Carlo tracking efficiency. The statistical uncertainty is negligible.

4.4 Simulation

The MC simulation of *BABAR* events has two main components. Fundamental physical processes such as B mixing and particle decays are generated by EvtGen [49]. After long-lived particles have been produced, they are passed through a detailed GEANT4 simulation of the detector material [50]. The EvtGen package generates events based on quantum amplitudes for specific decays, allowing for the possibility of interference. This is critical for simulating the time-dependence of B^0 mixing and decay, and also in generating correct angular distributions of final-state particles based on helicity amplitudes. GEANT4 accurately models the passage of particles through matter, simulating processes like bremsstrahlung, multiple scattering, photon conversion, and decays of long-lived particles like charged kaons and pions. The package uses a detailed model of the *BABAR* detector geometry and materials.

Simulation data are produced in varying amounts depending on the process. For rare B decays, about 1000 events are simulated for each fb^{-1} of real data collected. $\Upsilon(4S)$ decays to neutral and charged pairs of B mesons are produced at $3\times$ data luminosity each. Light continuum events, $e^+e^- \to q\overline{q}$ $(q = u, d, s)$ are produced at $1\times$ luminosity, while $e^+e^- \to c\overline{c}$ events are simulated at $2\times$ luminosity.

Chapter 5

Analysis Overview

This chapter describes elements common to both the $B^0 \to K_S^0 \pi^0 \gamma$ and $B \to K\phi\gamma$ analyses. I discuss how B candidates and their daughters are formed from the reconstructed long-lived particles, the common variables used to separate signal from background, and the procedure of maximum likelihood fitting.

5.1 Building Candidates

To isolate the B mesons used in the analyses in this work, one combines the reconstructed tracks and neutral objects to build the intermediate short-lived particles, eventually reconstructing the B's. Vertices, flight lengths, momenta, and their associated uncertainties are determined in a single fit to the entire decay chain.

5.1.1 Decay Chain Fitting

The decay chains in these analyses are reconstructed and fit using an algorithm known within *BABAR* as `TreeFitter`. The algorithm details are given in [51]. The fit is modeled as a χ^2 quantity that depends on the particles' momenta, flight lengths, and decay vertices. These are expressed as parameters related to the measurements and uncertainties of the final-state particles (for example, hits in the drift chamber, measurements of $\mathrm{d}E/\mathrm{d}x$). Explicitly, for a five-parameter track helix with param-

eters $\vec{x}$, residuals $\vec{r}(\vec{x})$, and covariance matrix V, $\chi^2 = \vec{r}^T(\vec{x})V^{-1}\vec{r}(\vec{x})$. Constraints such as conservation of momentum and the equality of daughter production vertices to parent decay vertices are enforced through further contributions to the χ^2 in the form of Lagrange multipliers. Each constraint is expressed in the form $\vec{g}(\vec{x}) = 0$, and its χ^2 contribution is then $\chi^2 = 2\vec{\lambda}^T\vec{g}(\vec{x})$, where $\vec{\lambda}$ is the vector of Lagrange multipliers that will be treated the same as the other parameters in minimizing the χ^2. Other constraints (for example, mass constraints) are treated in the same way.

5.2 Separating Signal From Background

5.2.1 B Kinematic Variables

The primary way to identify B decays over background is to isolate a window around variables whose distributions show a peak for such decays. One common variable is the beam energy substituted mass,

$$m_{\mathrm{ES}} = \sqrt{(s/2 + \mathbf{p}_i \cdot \mathbf{p}_B)^2/E_i^2 - p_B^2}, \tag{5.1}$$

where $(E_i, \mathbf{p}_i)$ and $(E_B, \mathbf{p}_B)$ are the four-momenta of the initial e^+e^- system and the reconstructed B candidate. The m_{ES} variable peaks at the B mass. In the e^+e^- center of mass (CM) frame, m_{ES} takes on a particularly simple form: $m_{\mathrm{ES}} = \sqrt{s/4 - p_B^{*2}}$, where the asterisk denotes a quantity measured in the CM frame. Because the reconstructed B energy is not used in m_{ES}, another variable may be defined to exploit that information:

$$\Delta E = E_B^* - \sqrt{s}/2. \tag{5.2}$$

The resolution of ΔE depends on the energy of the final-state particles. In this work, the presence of a high-energy photon sets the scale of the ΔE resolution at about 60 MeV. For $m_{\rm ES}$, the resolution in an all-charged final state is determined by the beam energy resolution, and is typically about 2.5 MeV/c^2. However, the addition of a high-energy photon increases this to approximately 3.5 MeV/c^2. In a case like $B \to K\phi\gamma$, where the other particles besides the photon have a typical energy resolution of 10–15 MeV, an alternative to $m_{\rm ES}$ that makes use of a B mass constraint offers an improvement.

The alternate set of variables is constructed under the assumption that there are two B mesons in each event and each of them has the B-meson mass. One variable is simply the reconstructed mass:

$$m_{\rm Rec} = \sqrt{E_B^2 - p_B^2}. \tag{5.3}$$

The $m_{\rm Rec}$ variable is approximately equal to $\Delta E + m_B$. The other variable is the mass of the other side of the event, assuming the signal-side has the B mass:

$$m_{\rm Miss} = |q_i - \hat{q}_B|, \tag{5.4}$$

where q_i is the four-momentum of the e^+e^- system and $\hat{q}_B$ is the four-momentum of the reconstructed B after a mass constraint has been applied. Near the B mass peak, $m_{\rm Miss}$ and $m_{\rm ES}$ are related by $m_{\rm ES} \approx (m_{\rm Miss} + m_B)/2$. That is, the raw $m_{\rm Miss}$ distribution is wider than $m_{\rm ES}$ by a factor of two for both signal and background, so to compare directly between $m_{\rm Miss}$ and $m_{\rm ES}$, one must replace $m_{\rm Miss}$ by $(m_{\rm Miss} + m_B)/2$.

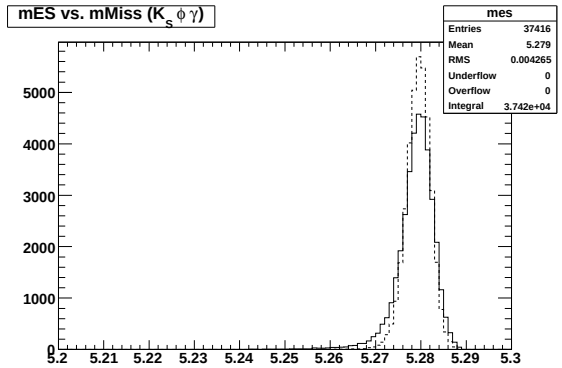

Figure 5.1: Comparison of $m_{\rm ES}$ (solid) and $(m_{\rm Miss} + m_B)/2$ (dashed) for $B \to K\phi\gamma$. The vertical scale is arbitrary, though both histograms are normlized to the same area.

In the $B \to K\phi\gamma$ analysis (Fig. 5.1), the $m_{\rm Miss}$ distribution is narrower than $m_{\rm ES}$, offering a better separation between signal and background. This is a result of the single photon's resolution improving due to the B mass constraint. Therefore, in that analysis the pair $m_{\rm Miss}$ and $m_{\rm Rec}$ is used instead of $m_{\rm ES}$ and ΔE. On the other hand, Fig. 5.2 shows that there is essentially no difference between $m_{\rm ES}$ and $m_{\rm Miss}$ for the $B^0 \to K^0_S\pi^0\gamma$ analysis. In this case both the photon and π^0 have poor resolution in comparison to the K^0_S, and mass-constraining the B cannot improve them simultaneously. Therefore, $m_{\rm ES}$ and ΔE are used in that case, as in most other *BABAR* analyses.

5.2.2 Angular Distributions

Because electrons and positrons are effectively massless at high energies, they can only have a vector interaction if their helicities are opposite. Therefore, when

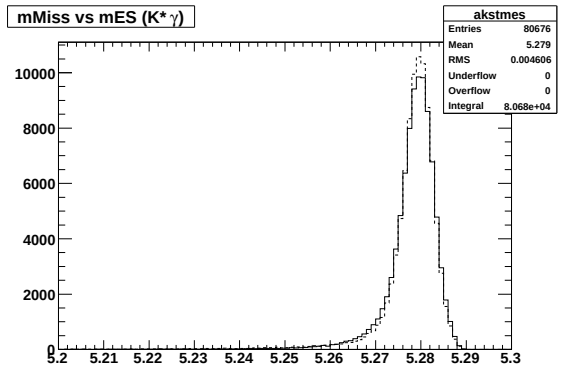

Figure 5.2: Comparison of $m_{\rm ES}$ (solid) and $m_{\rm Miss}$ (dashed) for $B^0 \to K^0_S \pi^0 \gamma$. The vertical scale is arbitrary, though both histograms are normalized to the same area.

the vector $\Upsilon(4S)$ resonance is produced at *BABAR*, it has a ± 1 spin polarization along its direction of motion. That means the distribution of the angle θ^*_B between one of the daughter B mesons and the electron direction in the $\Upsilon(4S)$ frame will follow $\left|Y^{m=\pm 1}_{\ell=1}(\theta,\phi)\right|^2 \propto \sin^2\theta$. The $\Upsilon(4S)$ frame is the event CM frame and the electron direction is the z axis, so this angle is also the polar angle of the B in the CM frame. For correctly-reconstructed $B\overline{B}$ events, the cosine of that angle will be distributed according to $\mathcal{P}(\cos\theta^*_B) = (1-\cos^2\theta^*_B)$. Non-$B\overline{B}$ events and improperly reconstructed events will be evenly distributed, as in Fig. 5.3.

5.2.3 Event Shape Variables

The thrust T of a set of particle momenta $\vec{p}_i$ is given by

$$T = \frac{\sum_i |\hat{n}\cdot\vec{p}_i|}{\sum_j |\vec{p}_j|}, \tag{5.5}$$

where the unit-vector thrust axis $\hat{n}$ maximizes T. The more particles that are aligned along a certain direction, the higher the thrust will be. Because B mesons are

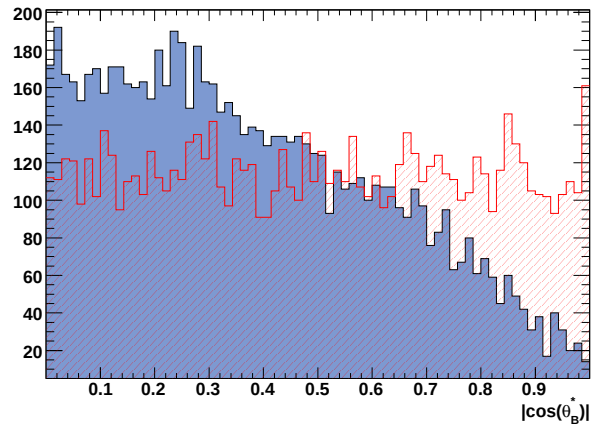

Figure 5.3: Monte Carlo comparison of $|\cos(\theta_B^*)|$ for signal (solid blue) and continuum background (hatched red). The histograms are normalized to equal areas.

produced nearly at rest in the *BABAR* CM frame, $\Upsilon(4S) \to B\overline{B}$ events will be more isotropically distributed, whereas continuum events are more jet-like. Therefore, the thrust of $B\overline{B}$ events is smaller than for continuum. The thrust and thrust axis may be calculated for all particles in an event, or only for a subset.

The thrust axis may be used to calculate a series of event-shape moments, L_i, defined by

$$L_i = \sum_j |p_j^*||\cos\theta_j^*|^i, \tag{5.6}$$

where p_j^* is the CM momentum of each particle j not used to reconstruct the signal B candidate and θ_j^* is the angle between that particle and the thrust axis of the signal B candidate. The ratio L_2/L_0 is a measure of how isotropic a group of particles is. Smaller values indicate a more spherical distribution, while larger values indicate a jet-like distribution. A comparison is given in Fig. 5.4. This ratio is used in both analyses of this work to separate $B\overline{B}$ events from continuum.

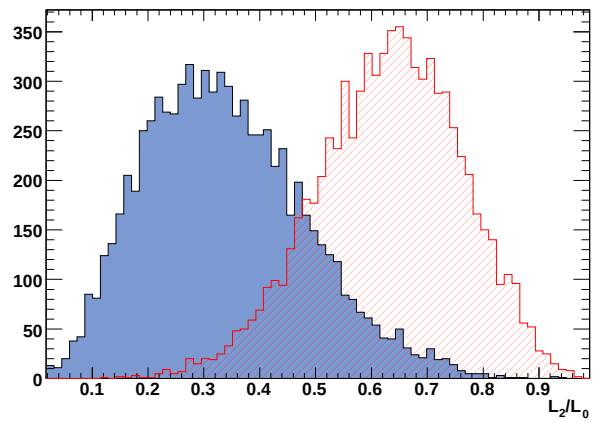

Figure 5.4: Monte Carlo comparison of L_2/L_0 for signal (solid blue) and continuum background (hatched red). The histograms are normalized to equal areas.

5.2.4 Low-Level Event Selection

Both of the analyses in this work share common low-level criteria to select hadronic events. The criteria are implemented as the logical OR of two filters, `BGFMultiHadron` and `BFGNeutralHadron`. The first one selects events with several charged hadrons. It requires more than two charged tracks (primarily to reject Bhabha scattering) and requires $R_2/R_0 < 0.98$, where $R_l = \sum_{i,j} \frac{|p_i^*||p_j^*|}{s} P_l(cos\theta_{ij}^*)$, P_l is the l-th order Legendre polynomial, and the sum involves particles of center-of-mass momenta p_i^* and p_j^*, separated by an angle θ_{ij}^*. This is qualitatively similar to L_2/L_0. For this filter, the sum is over the charged particles in the event. Because `BGFMultiHadron` is somewhat inefficient for final states with several neutral particles, the `BFGNeutralHadron` filter is also used.

`BFGNeutralHadron` is orthogonal to `BGFMultiHadron` in that it operates on events with no more than two charged tracks. It considers neutral EMC clusters

of energy greater than 100 MeV and labels them as photons if the energy is greater than 500 MeV. Events with two tracks must also contain at least 2 photons or 3 clusters. Events with one track must contain at least two photons or four clusters. Finally, events without any tracks must have at least three photons or six clusters. The ratio R_2/R_0, in which the sums are over charged tracks and neutral clusters, must be less than 0.95.

5.3 Maximum Likelihood Fitting

The maximum likelihood method is a general method to separate signal from background based on the known distributions of various quantities, and to extract physical parameters from these distributions. One begins by describing the distributions of the observables $\vec{x}$ in terms of probability density functions (PDFs) $\mathcal{P}$, which may depend on parameters $\vec{\alpha}$. If there are N_{Tot} events in a data set, the likelihood $\mathcal{L}$ is written as

$$\mathcal{L} = \prod_{i}^{N_{\mathrm{Tot}}} \left[f\mathcal{P}_{\mathrm{sig}}(\vec{x}_i; \vec{\alpha}_{\mathrm{sig}}) + (1-f)\mathcal{P}_{\mathrm{bkg}}(\vec{x}_i; \vec{\alpha}_{\mathrm{bkg}}) \right], \tag{5.7}$$

where f is the fraction of signal events. This method may be extended to include more types of signal and background, with a corresponding increase in the number of f parameters. The parameters $\vec{\alpha}$ and f are varied until a maximum is found in $\mathcal{L}$. In practice this is usually accomplished by minimizing $-\log \mathcal{L}$.

An extended maximum likelihood fit incorporates the Poisson probability denisities for the number of each type of event. Using again the example with

signal and background, the extended likelihood is

$$\mathcal{L} = \frac{\exp\left[-(N_{\text{sig}} + N_{\text{bkg}})\right]}{N_{\text{Tot}}!} \prod_{i}^{N_{\text{Tot}}} \left[N_{\text{sig}}\mathcal{P}_{\text{sig}}(\vec{x}_i; \vec{\alpha}_{\text{sig}}) + N_{\text{bkg}}\mathcal{P}_{\text{bkg}}(\vec{x}_i; \vec{\alpha}_{\text{bkg}})\right]. \tag{5.8}$$

The extended maximum likelihood method is used in this work to extract signal yields, signal *CP* asymmetries, and various background parameters.

5.3.1 Conditional Observables

In the above equations, a clear separation is made between the observables $\vec{x}_i$ and the parameters $\vec{\alpha}$. However, this is not always the case. For example, the event-by-event uncertainty of Δt changes the parameters of the Δt resolution function (Eq. 6.9) for each event. Therefore, the PDF must be normalized individually for each event, depending on the value of the so-called conditional observable, such that its integral over the other (non-conditional) observables is always one.

Chapter 6

Time-Dependent *CP* Violation

In Sec. 2.4.1.2 I described how a study of time-dependent *CP*-violating asymmetries could reveal information on the photon polarization in certain $b \to s\gamma$ decays. Here I present the details of how *CP* violation in $\Upsilon(4S) \to B^0\overline{B}^0$ decays varies with time, and how the time difference between the two B^0 decays in the event is determined.

6.1 Mathematical Formalism

At the PEP-II storage ring at SLAC, electrons and positrons collide at a center of mass energy corresponding to the peak of the $\Upsilon(4S)$ resonance. When the $\Upsilon(4S)$ decays to neutral B pairs, it produces an entangled B^0-$\overline{B}^0$ state in which the meson flavors oscillate in phase. Once can define the proper time t_1 of the forward-moving B and the proper time t_2 of the backward-moving one such that the particles are produced at $t_1 = t_2 = 0$. Continuing with the notation of Sec. 2.3, the combined B^0-$\overline{B}^0$ state may be written

$$|\psi(t_1, t_2)\rangle = \frac{1}{\sqrt{2}}\left[|B^0(t_1)\rangle|\overline{B}^0(t_2)\rangle - |\overline{B}^0(t_1)\rangle|B^0(t_2)\rangle\right]. \tag{6.1}$$

The relative negative sign between the two terms preserves the bose symmetry of the state if the forward and backward particles, which have relative orbital angular momentum $L = 1$, are swapped. Writing this in terms of the flavor eigenstates

(Eq. 2.14), one obtains:

$$|\psi(t_1,t_2)\rangle = \frac{1}{\sqrt{2}}e^{-(\Gamma/2+i\bar{m})(t_1+t_2)}[\cos(\Delta m\Delta t/2)(|B^0\rangle|\overline{B}^0\rangle - |\overline{B}^0\rangle|B^0\rangle)$$
$$-i\sin(\Delta m\Delta t/2)(\frac{p}{q}|B^0\rangle|B^0\rangle - \frac{q}{p}|\overline{B}^0\rangle|\overline{B}^0\rangle)], \qquad (6.2)$$

where $\Delta t = t_1 - t_2$.

Now I define the amplitudes for neutral B^0 ($\overline{B}^0$) decay to a final state f^+ (f^-) that preserves the B flavor at the time of decay (self-tagging decay):

$$A_{f^+} = \langle f^+|H|B^0\rangle \qquad \overline{A}_{f^+} = \langle f^+|H|\overline{B}^0\rangle = 0$$
$$\overline{A}_{f^-} = \langle f^-|H|\overline{B}^0\rangle \qquad A_{f^-} = \langle f^-|H|B^0\rangle = 0. \qquad (6.3)$$

Here H is the full Hamiltonian responsible for B interactions, including decay. The absolute-value-squared of each amplitude represents the branching fraction for the decay. The matrix element between the state $|\psi(t_1,t_2)\rangle$ and a final state composed of two oppositely-charged self-tagging states is sensitive only to the cosine term in Eq. 6.2, the coefficient of which is related to the direct CP asymmetry

$$A_{CP} = \frac{\Gamma(\overline{B}\to f^-) - \Gamma(B\to f^+)}{\Gamma(\overline{B}\to f^-) + \Gamma(B\to f^+)}. \qquad (6.4)$$

Alternatively, a self-tagging final state with two of the same tag is sensitive only to the sine term, related to CP violation in B^0 mixing. If one of the B mesons (call it the one that decays at time t_1) decays to a state f_{CP} accessible to both B^0 and $\overline{B}^0$, then the matrix element is sensitive to both terms, and to possible interference between B^0 mixing and decay. In this case, the f_{CP} state must be an eigenstate of charge conjugation, and since it also comes from a parity eigenstate (either a B^0 or

$\overline{B}^0$) it is a CP eigenstate. Defining the amplitudes,

$$A_{f_{CP}} = \langle f_{CP}|H|B^0\rangle$$
$$\overline{A}_{f_{CP}} = \langle f_{CP}|H|\overline{B}^0\rangle, \tag{6.5}$$

one can write the probability distribution for a final state with one f_{CP} and one tag $f^{\pm}$ state:

$$\begin{aligned}\mathcal{P}_{\pm}(t_1,t_2) &= |\langle f_{CP}|\langle f^{\pm}|H|\psi(t_1,t_2)\rangle|^2 \\ &= \frac{\Gamma^2}{4}e^{-\Gamma(t_1+t_2)}\left[1 \pm \frac{2Im(\lambda)}{|\lambda|^2+1}\sin(\Delta m\Delta t) \pm \frac{|\lambda|^2-1}{|\lambda|^2+1}\cos(\Delta m\Delta t)\right],\end{aligned} \tag{6.6}$$

where $\lambda \equiv \frac{q}{p}\frac{\overline{A}_{f_{CP}}}{A_{f_{CP}}}$. Since (t_1+t_2) is independent of Δt, Eq. 6.6 can be integrated over (t_1+t_2) between $|\Delta t|$ and infinity. After defining $S \equiv \frac{2Im(\lambda)}{1+|\lambda|^2}$ and $C \equiv \frac{1-|\lambda|^2}{1+|\lambda|^2}$,

$$\mathcal{P}_{\pm}(\Delta t) = \frac{1}{4\tau}e^{-|\Delta t|/\tau}\left[1 \pm S\sin(\Delta m\Delta t) \mp C\cos(\Delta m\Delta t)\right], \tag{6.7}$$

where τ is the B^0 lifetime. The S term is a measure of CP violation due to interference between B^0 decays with and without mixing, while $C = -A_{CP}$.

6.2 Experimental Effects

Mistakes in flavor tagging dilute S and C by a factor of $(1-2w)$, where w is the mistag rate. Tagging efficiency differences $\mu = \frac{\epsilon_{B^0}-\epsilon_{\overline{B}^0}}{\epsilon_{B^0}+\epsilon_{\overline{B}^0}}$ also distort the measured CP asymmetry parameters. Taking these effects into account, Eq. 6.7 becomes

$$\begin{aligned}\mathcal{P}_{\pm}(\Delta t) = \frac{1}{4\tau}e^{-|\Delta t|/\tau}\{&1 \mp \Delta w \pm \mu(1-2w) \pm [(1-2w) \pm \mu(1 \mp \Delta w)] \\ &[S\sin(\Delta m\Delta t) - C\cos(\Delta m\Delta t)]\}.\end{aligned} \tag{6.8}$$

Because the measured values of Δt are not significantly larger than the detector resolution, one needs to convolve Eq. 6.8 with a resolution function (RF) that relates the measured Δt to the true one. The RF is parameterized as the sum of three Gaussian distributions (core, tail and outlier), and is a function of $\delta_t = \Delta t_{\text{Measured}} - \Delta t_{\text{True}}$ and the measurement uncertainty $\sigma_{\Delta t}$:

$$\begin{aligned}\mathcal{R}(\delta_t, \sigma_{\Delta t}) = &\frac{f_{\text{core}}}{S_{\text{core}}\sigma_{\Delta t}\sqrt{2\pi}} \exp\left(-\frac{(\delta_t - b_{\text{core}}\sigma_{\Delta t})^2}{2(S_{\text{core}}\sigma_{\Delta t})^2}\right) + \\ &\frac{f_{\text{tail}}}{S_{\text{tail}}\sigma_{\Delta t}\sqrt{2\pi}} \exp\left(-\frac{(\delta_t - b_{\text{tail}}\sigma_{\Delta t})^2}{2(S_{\text{tail}}\sigma_{\Delta t})^2}\right) + \\ &\frac{f_{\text{out}}}{\sigma_{\text{outl}}\sqrt{2\pi}} \exp\left(-\frac{\delta_t^2}{2\sigma_{\text{outl}}^2}\right). \end{aligned} \tag{6.9}$$

The f parameters represent the fraction of events in each Gaussian, and $f_{\text{out}} = 1 - f_{\text{core}} - f_{\text{tail}}$. The scale factors S_{core} and S_{tail} account for over- or under-estimations of the Δt uncertainties. Possible biases are given by b_{core} and b_{tail}. For the outlier distribution, which accounts for less than 0.5% of events, there is no offset and its width is fixed to 8 ps. Parameters of the RF are determined by the same sample of self-tagging $B^0 \to D^{(*)-}\pi^+/\rho^+/a_1^+$ decays used to evaluate the tagging algorithms (Sec. 4.2).

Finally, although Δt is needed to determine the S parameter in Eq. 6.8, it is not needed for C. As long as there is a usable flavor tag, C can be determined by integrating over all Δt:

$$\begin{aligned}\mathcal{P}_\pm = \frac{1}{2}\frac{1}{1 - \mu C[1 + \Delta m_d^2 \tau^2]^{-1}}[1 \pm \mu(1 - 2w) \mp \Delta w \\ - \frac{C}{1 + \Delta m_d^2 \tau^2}(\pm(1 - 2w) + \mu(1 \mp \Delta w))]. \end{aligned} \tag{6.10}$$

6.3 Measuring Δt

The proper lifetime difference Δt between two B^0 mesons in an event is primarily determined by the spatial separation of their decay vertices in the laboratory along the direction of the boost, Δz:

$$\Delta t = \Delta z / \beta\gamma c. \tag{6.11}$$

This ignores the momentum of the B^0 mesons in the $\Upsilon(4S)$ frame, approximately $340\,\mathrm{MeV}/c$. To improve the Δt resolution by about 5%, one can take into account the terms related to the transverse motion of the B^0 mesons. This also introduces a dependency on the sum of decay times $t_{\mathrm{sig}} + t_{\mathrm{tag}}$. Because this sum is not well-measured, an approximation is used: $t_{\mathrm{sig}} + t_{\mathrm{tag}} = \tau + |\Delta t|$. This yields

$$\Delta z = \beta\gamma\gamma^* \Delta t + \gamma\beta^*\gamma^* \cos\theta^* c(\tau + |\Delta t|), \tag{6.12}$$

where β^*, γ^*, and θ^* are the velocity, boost factor, and polar angle with respect to the z axis of the signal B in the $\Upsilon(4S)$ frame.

6.3.1 Determination of Δz

The Δz is primarily determined by track measurements in the SVT. The excellent position and angular resolutions translate into precise z vertex positions of the decay positions of the signal B and tag B. In the analysis of $B^0 \to K_S^0 \pi^0 \gamma$, there are no tracks originating directly from the signal B vertex, so some additional constraints must be applied, described in this section.

The vertex of the tag-side B is determined using all tracks in the event that

are not associated with the signal side. Because some of the decay products may be long-lived, such as K_S^0 and Λ^0 particles, a search for so-called V^0 neutral vertices is performed. The vertices for K_S^0 (Λ^0) candidates must be separated by at least 2 mm (5 mm) from the primary event vertex in the x-y plane with an opening angle greater than 200 mrad, the candidates must be within 7 MeV/c^2 (4 MeV/c^2) of the nominal mass, and the vertex fit probability (without a mass constraint) must be greater than 0.001. Photon conversion $\gamma \to e^+e^-$ candidates are also identified. The x-y distance between the two candidate tracks must be less than 5 mm, and less than 1 cm in z, with an invariant mass less than 10 MeV/c^2. To reduce the effects of long-lived charm-meson decays and other background tracks, some tracks are removed from the vertex fit. The track with the largest χ^2 contribution greater than 6 is removed and the vertex is refit. The procedure is iterated until all tracks pass this requirement. The z resolution on the tag side is approximately 180 μm.

In contrast, the signal side B decay vertex is usually determined with better precision. For example, in $B^0 \to J/\psi\, K_S^0$ events the B^0 vertex is primarily determined by the J/ψ decay to two leptons. In Monte Carlo (MC) studies, the B^0 vertex is reconstructed with a resolution of 65 μm, while the observed resolution in data is about 5% worse. Combined with the tag side vertex, the root mean square width of the residual Δz distribution in MC is 190 μm. This corresponds to a typical Δt resolution of 1.1 ps.

In hadronic B^0 decays, the signal-side vertex is normally determined in a fit using charged tracks originating either from the B^0 vertex or from strong resonances produced by it. However, all daughter particles of the $B^0 \to K_S^0\pi^0\gamma$ decay are

neutral. The decay vertex cannot be determined in the same manner as for $B^0 \to J/\psi\, K_S^0$ decays. However, precise reconstruction of the K_S^0 momentum and knowledge of the beam spot provide sufficient constraints to estimate a decay vertex. The beam spot is determined during data-taking with two-track events. Its dimensions are approximately $200\,\mu$m in x, $5\,\mu$m in y, and $8000\,\mu$m in z. The small transverse size of the beam provides a good constraint on the z position of a B^0 decaying inside it. A further constraint on the flight length of the B^0 mesons in the event is provided by requiring the average sum of B decay times to be 2τ with an uncertainty of $\sqrt{2}\tau$. The combination of these constraints with the K_S^0 momentum yields a Δt resolution of 1.4 ps, provided that both pions in the $K_S^0 \to \pi^+\pi^-$ decay leave hits in the SVT. This is discussed further in Sec. 7.1.2.

Chapter 7

Study of $B^0 \to K_S^0 \pi^0 \gamma$

In the previous section I discussed how to measure CP violation arising from interference between the amplitudes for B^0 mixing and the amplitudes for decay to a CP eigenstate. The final state must be accessible to both B^0 and $\overline{B}^0$ mesons, otherwise the mixing and decay processes do not interfere with each other. As discussed in Sec. 2.4.1.2, this phenomenon may be used to probe the photon polarization in $b \to s\gamma$ decays to final states accessible to both B flavors. Because the photon is polarized according to the B flavor in the standard model (SM), the interference effect is expected to vanish, resulting in an asymmetry S near zero. Any significant evidence of S larger than about ± 0.1 would point to new physics. For comparison, completely unpolarized photons would result in $S \approx -\sin(2\beta)$ if no new weak phases contribute.

A significant challenge for this analysis is determining the B^0 decay vertex without any charged tracks pointing to it (Fig 7.1). The technique discussed in Sec. 6.3.1 was pioneered by *BABAR* and initially used to determine time-dependent CP asymmetries in $B^0 \to K_S^0 \pi^0$ [52]. It was later applied to $B^0 \to K_S^0 \pi^0 \gamma$ decays with 124×10^6 $B\overline{B}$ pairs [53]. The most recent measurements by *BABAR* [54] and Belle [55] use 232×10^6 and 535×10^6 $B\overline{B}$ pairs, respectively. Here I present the final *BABAR* measurements of S and C in this mode, using the entire data set of

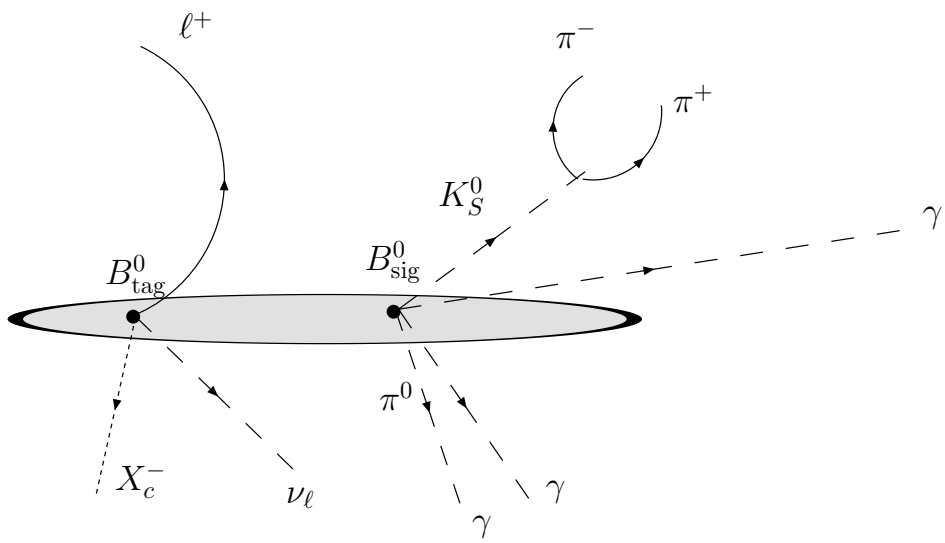

Figure 7.1: Schematic of the $B^0 \to K_S^0\pi^0\gamma$ decay topology near the beam spot (shaded area).

467×10^6 $B\overline{B}$ pairs.

7.1 Event Selection

The measurement is performed in two regions separated by K_S^0-π^0 invariant mass. The K^* region is defined by $0.8 < m(K_S^0\pi^0) < 1.0\,\mathrm{GeV}/c^2$, in which only the $K^*(892)^0$ resonance contributes. This is the region most commonly given in theoretical calculations, as described in Sec. 2.4.1.2 [23, 24, 27]. A higher-mass range is also defined, $1.1 < m(K_S^0\pi^0) < 1.8\,\mathrm{GeV}/c^2$, which is well-separated from the K^* region. For simplicity I refer to the latter range as the non-K^* region, although contributions from higher kaon resonances decaying to $K\pi$ are expected along with non-resonant decays. If SM hadronic corrections are not too large, then S and C

Table 7.1: Number of MC events used to evaluate selection criteria for $B^0 \to K_S^0\pi^0\gamma$. The "generic" B decays do not include $b \to s\gamma$ processes.

Sample	Number of Events	Equivalent Luminosity
uds Continuum	903.5M	$432\,\mathrm{fb}^{-1}$
Charm Continuum	1088M	$837\,\mathrm{fb}^{-1}$
Generic B^+ B^-	702.6M	$1{,}278\,\mathrm{fb}^{-1}$
Generic B^0 $\overline{B}^0$	685.3M	$1{,}246\,\mathrm{fb}^{-1}$
$B^+ \to X_s^+\gamma$	512k	$2{,}623\,\mathrm{fb}^{-1}$
$B^0 \to X_s^0\gamma$	587k	$3{,}007\,\mathrm{fb}^{-1}$
$B^0 \to K^{*0}\gamma$ signal	587k	$115{,}417\,\mathrm{fb}^{-1}$
$B^0 \to K_S^0\pi^0\gamma$ signal	587k	$120{,}226\,\mathrm{fb}^{-1}$

should not vary with $m(K_S^0\pi^0)$ [56]. However, because there is no consensus on details of these corrections [25, 26], the two $m(K_S^0\pi^0)$ regions are treated separately.

The Monte Carlo (MC) samples used to validate the selection criteria are summarized in Table 7.1. Events containing $b \to s\gamma$ decays are removed from the samples of generic B decays. In $b \to s\gamma$ decays and non-K^* signal, the photon energy spectrum is generated according to a model of Kagan and Neubert [57] with b quark mass $m_b = 4.62\,\mathrm{GeV}/c^2$. The recoiling hadronic system decays according to phase space.

7.1.1 Preselection

Candidate preselection involves creating lists of final-state particles and intermediate resonances. Events containing these candidates are used to create the parent B candidates by four-momentum addition. Primary photons are selected from single bumps in the EMC that have not been matched to any track. The photon candidate must have at least 30 MeV of energy, with a lateral moment less than

0.8. Primary photons are selected within a wide range of e^+e^- center-of-mass (CM) energy, $1.5 < E^*_\gamma < 3.5\,\mathrm{GeV}$. This is later reduced by the requirements on invariant mass of the recoiling hadronic system.

Candidate K^0_S mesons are selected from pairs of oppositely-charged tracks, assumed to be pions. The four-momenta (evaluated at closest approach to the interaction point) of the tracks used in the K^0_S must add to create an invariant mass between 300–800 MeV/c^2. Track pairs passing this criterion are then examined at their point of closest approach to each other. There, the track momenta are added to determine an effective invariant mass. This must be between 450–550 MeV/c^2. Finally, K^0_S candidates must pass a vertex fit with `TreeFitter` (Sec. 5.1.1), after which the invariant mass must be within $\pm 25\,\mathrm{MeV}/c^2$ of the nominal mass, determined by the particle data group [7].

Candidate π^0 mesons are created from photon pairs, each with energy greater than 30 MeV and lateral moment less than 0.8. The invariant mass of the combination must fall between 100 and 160 MeV/c^2, and the π^0 candidate energy must be greater than 200 MeV. The entire decay chain is fit to create B^0 candidates with $m_{\mathrm{ES}} > 5.2\,\mathrm{GeV}/c^2$ and $|\Delta E| < 0.250\,\mathrm{GeV}$. This fit includes the beam spot constraint and the sum-of-lifetimes constraint of the $\Upsilon(4S) \to B^0\overline{B}^0$ system necessary to create a signal-side vertex, described in Sec. 6.3.1. The tag-side B^0 vertex is determined using the method in the same section.

7.1.2 Final Selection

The above criteria select approximately 14 million events, the vast majority of which are combinatoric continuum background. In contrast, approximately 1000 K^* and 840 non-K^* signal events are expected at this stage, with an efficiency of about 40%. The branching fraction of $B^0 \to K^{*0}\gamma$ is $4.01 \pm 0.20 \times 10^{-5}$ [7], while in the non-K^* region it is assumed to be 3.8×10^{-5} based on the yield reported in *BABAR*'s previous publication of this mode [54]. To determine the final selection, the following criteria were selected to maximize the signal significance, taken to be the ratio of the number of signal events to the square root of signal-plus-background in MC. As a cross-check, the criteria were varied to verify that they result in the smallest expected errors on S and C.

The two charged pions making up the K_S^0 were required to fit to a vertex with a probability greater than 0.1%. K_S^0 candidates were selected to have a flight length greater than five times the uncertainty (Fig. 7.2). Finally, the K_S^0 candidate mass must be within $10\,\mathrm{MeV}/c^2$ of the nominal mass. These requirements are 80% efficient for signal and about 20% efficient for background, with most of the discriminating power coming from the flight length requirement.

Candidate π^0 mesons must have a mass within $20\,\mathrm{MeV}/c^2$ of the nominal π^0 mass. The laboratory energy of the π^0 must be greater than 590 MeV, which is a strong discriminant against background (Fig. 7.3). Together, these requirements are about 75% efficient for signal and 35% efficient for background.

In two-body $B^0 \to K^{*0}\gamma$ decays, angular momentum conservation requires

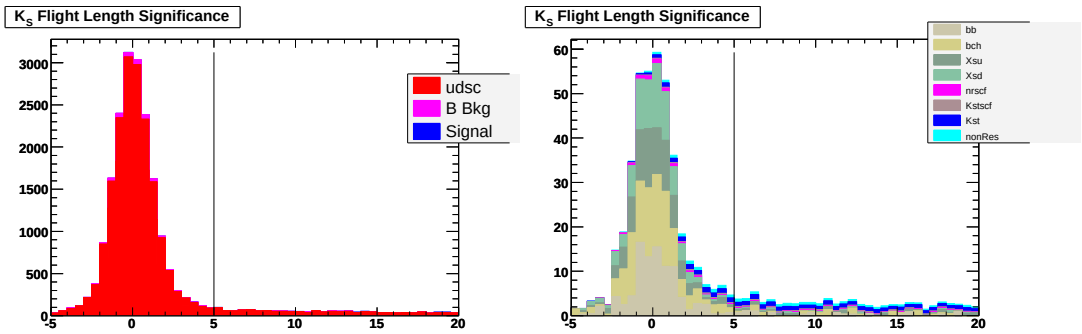

Figure 7.2: K_S^0 flight length significance in MC for signal and all background sources on the left, and with continuum removed on the right. The contributions on the right are, from the bottom up, generic B^0 decays, generic B^+, $B^+ \to X_s^+\gamma$, $B^0 \to X_s^0\gamma$, non-K^* cross feed, K^* cross feed, K^* signal, and non-K^* signal. The signal distributions are approximately flat and greater than zero, while background distributions peak at zero. The line marks the location of the cut.

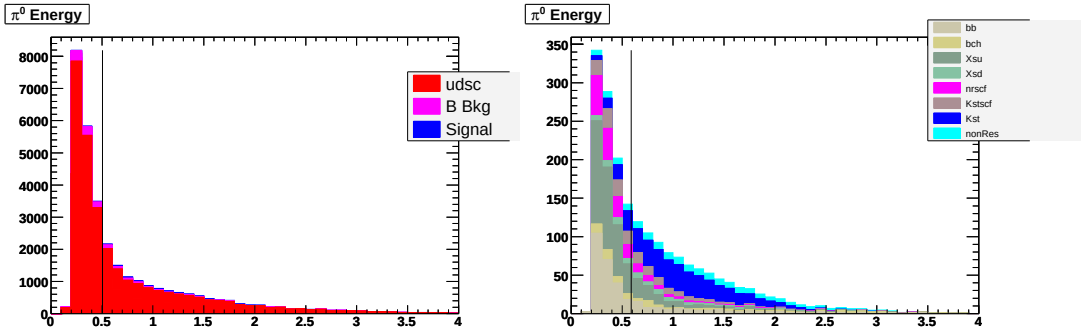

Figure 7.3: π^0 energy [GeV] in MC for signal and all background sources on the left, and with continuum removed on the right. The contributions on the right are, from the bottom up, generic B^0 decays, generic B^+, $B^+ \to X_s^+\gamma$, $B^0 \to X_s^0\gamma$, non-K^* cross feed, K^* cross feed, K^* signal, and non-K^* signal. The line marks the location of the cut.

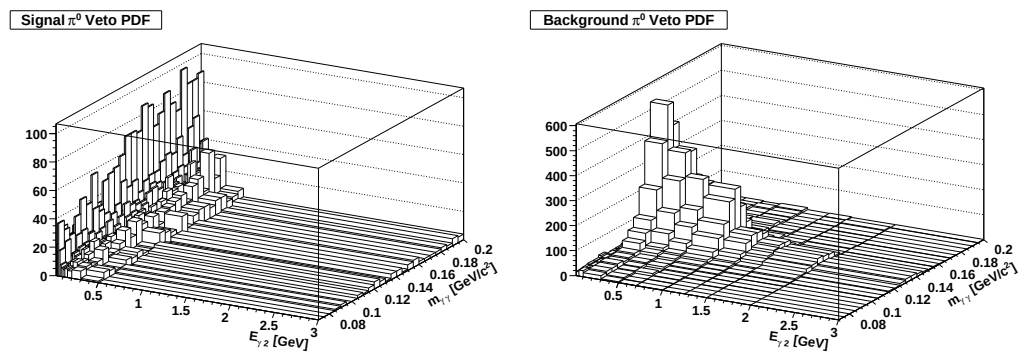

Figure 7.4: Signal and background histogram likelihood functions used for the π^0 veto of primary photons.

that the K^{*0} carry a polarization of ± 1 along its direction of motion. Therefore, in the K^* region, the signal distribution of the cosine of the K^{*0} helicity angle θ_{K^*} should follow $1 - \cos^2(\theta_{K^*})$, where θ_{K^*} is the angle in the K^{*0} frame between the K_S^0 and the B^0. Background events peak at ± 1, so a loose cut of $|\cos(\theta_{K^*})| < 0.9$ is applied in the K^* region.

Primary photon candidates that are likely to originate in π^0 or η decays are vetoed. The photon candidate is combined with all other photon candidates in the event, and a likelihood is formed from the diphoton mass and the energy of the second photon. Two-dimensional histograms are filled with MC samples of π^0 and η decays to serve as the background likelihood, $\mathcal{L}_{\rm bkg}$; signal MC samples are used to derive the corresponding signal likelihood, $\mathcal{L}_{\rm sig}$. Each likelihood is treated separately for π^0 and η discrimination. The π^0 likelihood shapes are given in Fig. 7.4.

The likelihood ratio for a photon candidate to be from a π^0 (η) is

$$\mathcal{L} = \frac{\mathcal{L}_{\rm bkg}}{\mathcal{L}_{\rm sig} + \mathcal{L}_{\rm bkg}}. \tag{7.1}$$

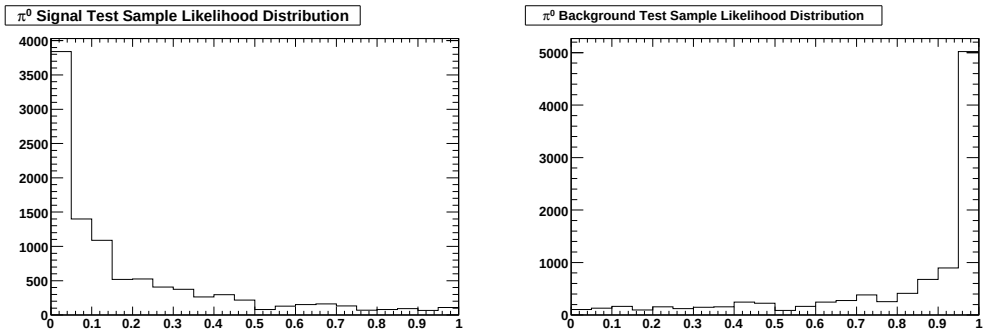

Figure 7.5: Signal and background likelihood ratio distributions of the π^0 test samples.

Values closer to one indicate a high background probability, while those closer to zero indicate more signal-like candidate photons. A second sample of MC events, separate from the sample used to fill the histograms, was used to validate this procedure. The likelihood ratio distributions of these so-called test samples are given in Fig. 7.5, and a comparison between the continuum MC and off-peak data is given in Fig. 7.6. The off-peak sample consists of $44\,\mathrm{fb}^{-1}$ of data taken at a center-of-mass energy 40 MeV below the $\Upsilon(4S)$ peak. The optimal cut on the π^0 (η) likelihood of the candidate photon was found to be 0.45 (0.90). Together these vetoes are 96% efficient for signal and 70–75% efficient for background.

As discussed in Sec. 5.2.2, in the CM frame B mesons are preferentially emitted away from the z axis, so a requirement of $|\cos(\theta_B^*)| < 0.90$ is imposed. To further reduce continuum background, the ratio of event-shape moments (Sec. 5.2.3) is limited to $L_2/L_0 < 0.55$. This quantity is used later to further discriminate $B\overline{B}$ events from continuum background in a maximum likelihood fit to the data.

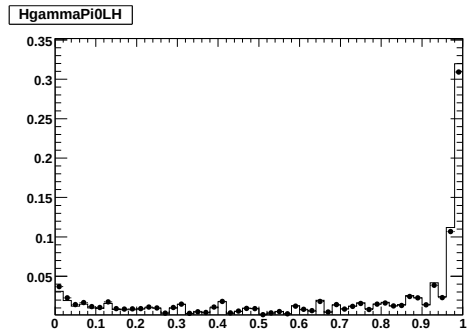

Figure 7.6: Offpeak data (points) compared to continuum MC (solid) for the π^0 likelihood ratio distributions, normalized to 1.

The unknown effective CP asymmetries of $B\overline{B}$ backgrounds could influence the signal CP asymmetries. This is discussed later in more detail as a systematic uncertainty in Sec. 7.3. To reduce this source of background, $B^+ \to K^{*+}(K_S^0\pi^+)\gamma$ candidates are explicitly reconstructed and the events containing them are removed. These events contributed one-quarter of the $B\overline{B}$ background in the 2005 publication of this analysis. In the current analysis, events containing a B^+ candidate with $m_{\rm ES} > 5.27\,{\rm GeV}/c^2$ and $0.8 < m(K_S^0\pi^+) < 1.0\,{\rm GeV}/c^2$ are removed.

Multiple B^0 candidates are found in 16% of the selected events. In these cases the candidate with π^0 mass closest to the nominal value is selected. If ambiguity persists, then the K_S^0 mass is used. In MC this procedure selects the signal candidate 94% of the time. After all selection criteria have been applied, the signal efficiency is 16%. In data, 3884 events are selected in the K^* region, of which 344 are expected to be signal, 37 $B\overline{B}$ background, and the rest are from continuum e^+e^- annihilation. In the non-K^* region, there are 6703 selected events, with 149 expected signal events,

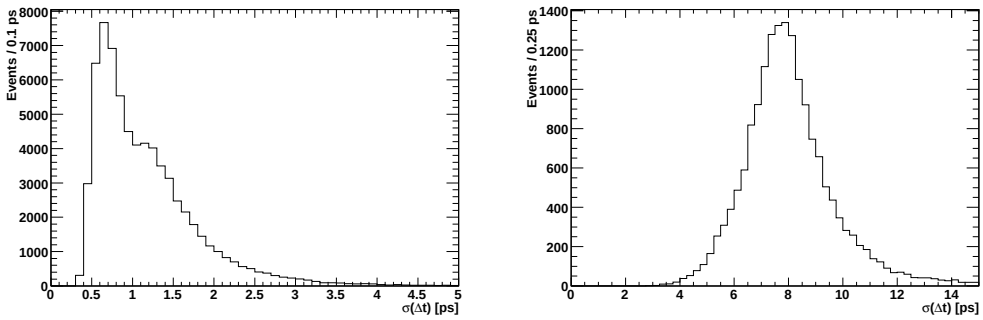

Figure 7.7: Δt uncertainty distribution for signal MC events in which both pion daughters of the K_S^0 have at least one ϕ and one z hit in the SVT (left) and events for which the pions are only detected in the DCH (right).

156 $B\overline{B}$ background, and the rest continuum.

The Δt quality depends on the transverse flight length of the K_S^0 candidate. If it decays outside the SVT, the resolution is greatly degraded (Fig. 7.7). Therefore, in order for an event to contribute to the S measurement, both pion tracks must each create at least one ϕ and one z hit in the SVT. Furthermore, the standard *BABAR* Δt quality cuts apply: $|\Delta t| < 20\,\text{ps}$ and $\sigma(\Delta t) < 2.5\,\text{ps}$. About 70% of both signal and background events pass these requirements and are labelled as having "good" Δt quality. The remaining events, with "poor" Δt quality, still contribute to the measurement of C as long as they have a usable flavor tag.

7.1.3 Characterization of Backgrounds

The majority of the background events after final selection consist of of continuum $e^+e^- \to q\overline{q}$. However, there are also significant expected $B\overline{B}$ backgrounds,

especially in the non-K^* region. These have a peaking shape in $m_{\rm ES}$, and have a peak offset from zero or no peak at all in ΔE. This type of background falls into two general categories: $b \to s\gamma$ backgrounds and hadronic B decays. Based on the MC, the two classes contribute about equally in the K^* region, while B to charm decays contribute about two-thirds of the $B\overline{B}$ background in the non-K^* region.

The $b \to s\gamma$ decays are simulated using the Kagan-Neubert model [57] with the effective b quark mass set to $4.65\,\mathrm{GeV}/c^2$. The main sources of $b \to s\gamma$ background are found to be $B \to K^*\pi\gamma$ modes, where the K^* decays to $K^0_S\pi$. At least one of the final-state pions is neutral, while the other one is not associated with the signal side. This source makes up half of the $b \to s\gamma$ background. Nonresonant $B^0 \to K^0_S\pi^+\gamma$ decays constitute about a quarter. The remaining background is from other $b \to s\gamma$ decays.

In the K^* region about one-quarter of the hadronic $B\overline{B}$ background comes from $B^0 \to \eta(\to \gamma\gamma)K^{*0}(\to K^0_S\pi^0)$, where the signal photon comes from the η decay and still passes the veto. The remaining backgrounds do not show any strong trends, but tend to contain a D meson whose decay includes a K^0_S, along with ρ mesons that produce pions. In the non-K^* region the largest contributions (15%) come from $B \to \rho^+ D$ processes in which the D emits a K^0_S in its decay.

Because the number of $B\overline{B}$ background events is expected to be about 10% as large as the signal in the K^* region and at least as large as the signal in the higher-mass region, an explicit parameterization for them is given in the maximum likelihood fit, described in the next section.

7.2 Determination of CP Asymmetries

The unbinned maximum likelihood fit to the two $m(K_S^0\pi^0)$ regions in data classifies three types of event: signal, $B\overline{B}$ background, and continuum background. The observables are $m_{\rm ES}$, ΔE, L_2/L_0, $m(K_S^0\pi^0)$, Δt, and tag flavor. In the non-K^* region, $m(K_S^0\pi^0)$ is not used. The conditional observables are the $m_{\rm ES}$ endpoint $m_0 = \sqrt{s}/2$ and the Δt uncertainty, $\sigma(\Delta t)$. The measured quantities S and C appear in the Δt probability distribution functions (PDFs), while the other variables are used to separate signal from the backgrounds. The data and PDFs are split two ways: by Δt quality and by tagging category. The full likelihood function can be written as:

$$\mathcal{L} = \prod_{c,t} \left[\frac{\exp\left[-\sum_j N_j f_{j,t} \epsilon_{j,c}\right]}{N_{c,t}!} \times \prod_i^{N_{c,t}} \left[\sum_j N_j f_{j,t} \epsilon_{j,c} \mathcal{P}_{j,t}(\vec{x}_i; \vec{\alpha}_{j,c}) \right] \right], \tag{7.2}$$

where N_j is the yield of component j (signal, $B\overline{B}$ background, or continuum), $f_{j,t}$ is the fraction of events of component j in Δt quality category t (good or poor), $\epsilon_{j,c}$ is the tagging efficiency for category c of component j, and $N_{c,t}$ is the number of data events in category c of quality t. The PDFs $\mathcal{P}_{j,t}$ are described below. In the following, signal and $B\overline{B}$ background parameters are determined by fits to MC, while continuum parameters are determined in the fit to data, except where noted.

7.2.1 Separation of Signal and Background

The signal $m_{\rm ES}$ PDF is modelled by a bifurcated Gaussian distribution with extended tails:

$$\mathcal{P}(x) = \exp\left[\frac{-(x-\mu)^2}{2\sigma_{L,R}^2 + \alpha_{L,R}(x-\mu)^2}\right], \tag{7.3}$$

where μ is the mean, σ is the core width, and α is the tail parameter. The L, R subscripts denote different parameter values on either the left or right side of the peak. The $m_{\rm ES}$ distribution for continuum background is an empirical threshold function [58]:

$$\mathcal{P}(m_{\rm ES}|m_0) = m_{\rm ES}[1-(m_{\rm ES}/m_0)^2]^{\frac{1}{2}} \times \exp\{c[1-(m_{\rm ES}/m_0)^2]\}, \tag{7.4}$$

where c is a slope parameter and m_0 is the conditional observable representing the kinematic endpoint. For $B\overline{B}$ background, the sum of a threshold function and bifurcated Gaussian is used.

The ΔE PDF for signal also uses the the bifurcated Gaussian distribution of Eq. 7.3. An exponential decay distribution is used for $B\overline{B}$ background and continuum, each with its own decay parameter. The distribution for L_2/L_0 is given in terms of a binned PDF. The variable bin widths ensure that approximately equal numbers of events fall into each bin. The signal, $B\overline{B}$ background, and continuum background distributions are all binned in the same way. The signal and $B\overline{B}$ background components share the same parameters, which are split by tagging category to account for different event shapes. However, the statistics of the data sample do not allow the same splitting to be done for background.

In the K^* region, the $m(K_S^0\pi^0)$ signal distribution is given by a relativistic

Breit-Wigner distribution appropriate for a P-wave K^* decay to $K_S^0\,\pi^0$. Both continuum and $B\overline{B}$ background use the same Breit-Wigner peaking shape on top of a linear background.

7.2.2 Fit to Δt Distribution

For events with good Δt quality, the PDFs for signal and $B\overline{B}$ background are a convolution of Eq. 6.8 with the resolution function of Eq. 6.9. The parameters of both functions are determined by a fit to a control sample of self-tagging $B^0 \to D^{(*)-}\pi^+/\rho^+/a_1^+$ decays in data. The core of the resolution function is split between the lepton tag category and the others to reflect the better performance of the lepton tag, which is found to have a smaller bias and a scale factor closer to one. The Δt shape of the continuum background was found to be consistent with prompt decays, described by the resolution function alone. Its parameters are determined in the fit to data.

Events with poor Δt quality are modelled by Eq. 6.10 for signal and $B\overline{B}$ background, which is sensitive to C but not S. For continuum events, the PDF depends only on the effective tagging efficiency difference μ for a given category.

$$\mathcal{P}_{\pm} = \frac{1}{2}(1 \mp \mu) \tag{7.5}$$

7.2.3 Fit Validation

The performance of the likelihood function is evaluated using simulated experiments generated both from PDFs and by sampling from MC distributions. In the

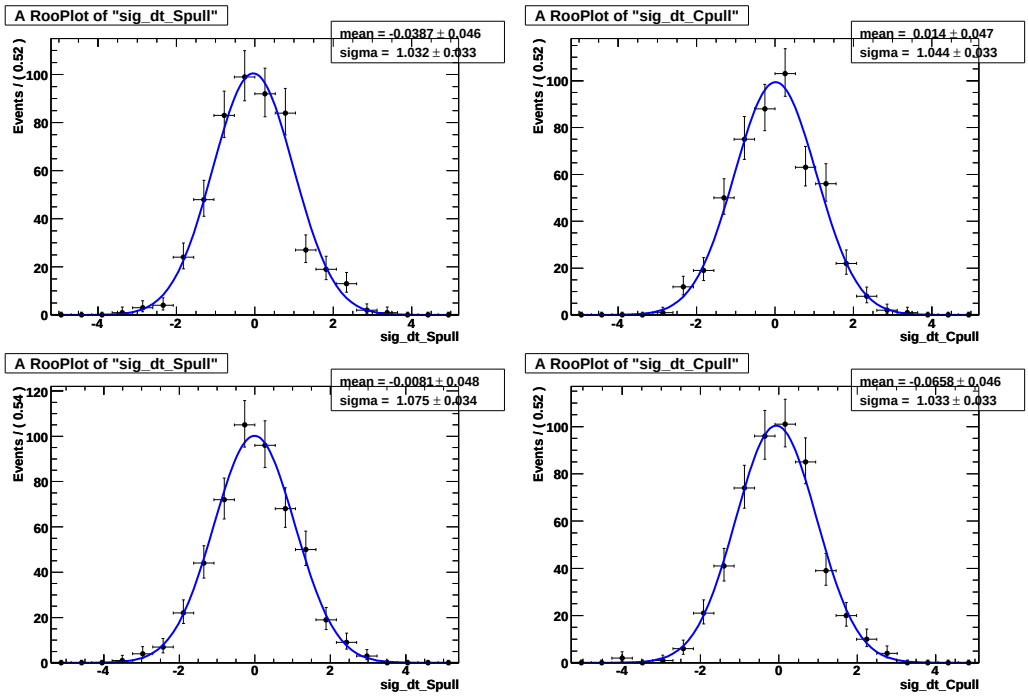

Figure 7.8: Pull distributions of 500 experiments in the K^* region (top) and the non-K^* region (bottom). A Gaussian fit is overlaid.

first test, 500 simulated experiments in each mass region are generated according to the PDFs determined in a fit to MC. S and C in each region are generated to be zero, as expected in the SM. Each experiment is fit using the likelihood function, and the resulting pull distributions of S and C in each mass region are given in Fig. 7.8. The means of the pull distributions are consistent with zero, and the widths are consistent with one. This indicates that the fit is unbiased and the uncertainties are estimated correctly. The widths of the S and C distributions themselves correspond to the expected resolution. In the K^* region this yields $\sigma(S) = 0.28$ and $\sigma(C) = 0.16$, while in the non-K^* region I find $\sigma(S) = 0.52$ and $\sigma(C) = 0.28$.

In another test, 2000 simulated experiments were performed in each mass

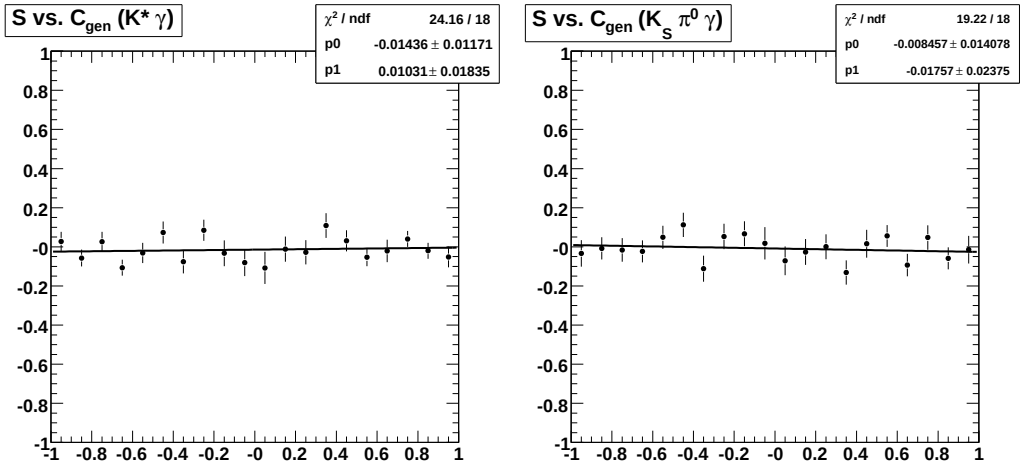

Figure 7.9: Measured S versus generated C for $B^0 \to K^{*0}\gamma$ on the left and $B^0 \to K_S^0\pi^0\gamma$ on the right.

Table 7.2: Results of linear fits to measured versus generated S and C.

	K^* Region		non-K^* Region	
	Slope	Intercept	Slope	Intercept
S_{meas} vs S_{gen}	0.987 ± 0.021	0.012 ± 0.013	0.989 ± 0.055	-0.036 ± 0.033
C_{meas} vs C_{gen}	1.021 ± 0.012	-0.007 ± 0.007	1.021 ± 0.024	-0.004 ± 0.014

region in which the generated S and C were selected randomly each time, subject to the physical condition $S^2+C^2 \leq 1$. Plots of the average measured S versus generated C are given in Fig. 7.9, showing no significant correlation. The fit linearity was tested by comparing measured versus generated parameters and fitting that relationship with a straight line. The results are given in Table 7.2, showing good agreement between the generated and observed values.

As a cross check, 250 experiments were performed in each mass region with the signal component sampled from MC and the background components generated from the PDFs. The resulting pull distributions are given in Fig. 7.10, again indicating

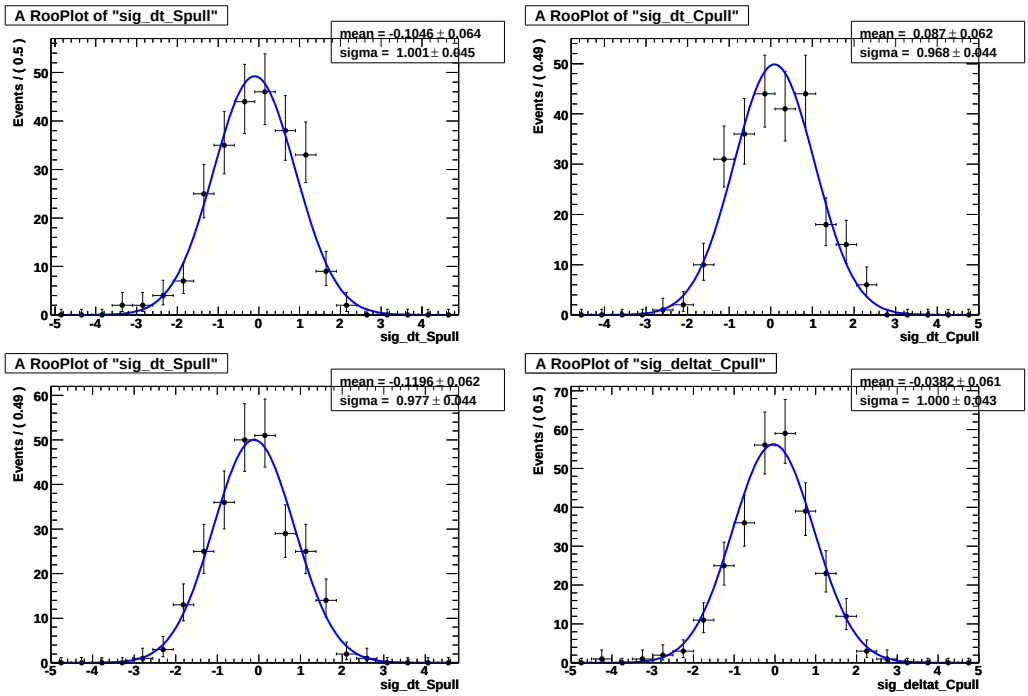

Figure 7.10: Pull distributions of 250 experiments in the K^* region (top) and the non-K^* region (bottom). Signal is sampled from the MC distributions.

that the fit performs as expected.

After the fit to data, one more ensemble of experiments is performed using the parameters determined in data. This is described in Sec. 7.3.3.

7.3 Systematic Uncertainties

The systematic uncertainties on S and C fall into four categories: those related to the Δt determination, the effective S and C of the $B\overline{B}$ background, possible fit bias, and tag-side interference. A summary of all systematic uncertainties appears at the end in Tab. 7.5.

7.3.1 Δt Determination

The determination of Δt relies on extrapolating the K_S^0 trajectory back to the beam spot. To be robust, the measurement must be insensitive to reasonable variations in the beam spot position, corresponding to the uncertainty of the beam spot position. Because the K_S^0 momentum direction is determined primarily by the SVT, mistakes in its alignment could affect the results. Finally, the resolution function for Δt is assumed to be the same as that determined by a data control sample; the uncertainty in this assumption is described here.

7.3.1.1 Beamspot and SVT Alignment

The transverse size of the beam spot is about $200\,\mu$m $\times$ $5\,\mu$m, the vertical direction being well-constrained. To test the sensitivity of the reconstruction to the beam spot position, signal MC is reprocessed in three ways: shifting the beam spot up by $20\,\mu$m, down by the same amount, and smearing its vertical component by $20\,\mu$m. The larger change of the first two checks is added in quadrature with the effect from smearing and taken as the uncertainty.

To evaluate the effect of SVT mis-alignments, the *BABAR* SVT alignment group provides several mis-alignment scenarios to be used in reprocessing signal MC. These scenarios are representative of typical SVT distortions over the lifetime of the experiment. The largest effect of these on S and C is taken as the uncertainty.

7.3.1.2 Resolution Function

The impact of the resolution function on the vertexing method used here is evaluated in *BABAR*'s study of time-dependent *CP* violation in $B^0 \to K^0_S \pi^0$ [59]. As part of that work, samples in data and MC of $B^0 \to J/\psi\, K^0_S$ decays are reconstructed in two ways: first, determining the B^0 vertex primarily from the $J/\psi \to \mu^+\mu^-$ decay; and second, ignoring the J/ψ vertex information and using the technique described here. A pull is formed based on the reconstructed Δt, assuming that the one including the J/ψ vertex information is correct:

$$p = \frac{\Delta t_{\text{No } J/\psi} - \Delta t_{\text{Incl } J/\psi}}{\sqrt{\sigma^2(\Delta t_{\text{No } J/\psi}) - \sigma^2(\Delta t_{\text{Incl } J/\psi})}}. \tag{7.6}$$

The pull distribution in data is found to be 7.4% wider in data than in MC. Applying a factor of 1.074 to the scale factors in the resolution function yields shifts in S and C that are taken as systematic uncertainties.

7.3.2 $B\overline{B}$ Background

There are two aspects of the $B\overline{B}$ background that can affect the signal S and C. The first is the shape of the background PDFs, which is discussed in the next section. Here, I discuss how the effective *CP* asymmetries of the $B\overline{B}$ background affects the measurement.

In the fit to data, the effective $B\overline{B}$ background S and C parameters are fixed to zero. These must be varied within a reasonable range to determine their effect on the signal. The $B\overline{B}$ backgrounds are divided first by whether they are B^+B^- events or $B^0\overline{B}^0$. Then they are split by whether they are $b \to s\gamma$ events or other

Table 7.3: Expected amounts of $B\overline{B}$ background.

Source	K^* Region	Non-K^* Region
$B^+ B^-$, no $b \to s\gamma$	2	52
$B^0 \overline{B}^0$, no $b \to s\gamma$	15	62
$B^+ \to X_s^+\gamma$	13	24
$B^0 \to X_s^0\gamma$	8	18

Table 7.4: Contributions to the $B\overline{B}$ background uncertainty on S and C.

Source	S	C
$B^+ B^-$, no $b \to s\gamma$	0	0.2
$B^0 \overline{B}^0$, no $b \to s\gamma$	0.4	0.2
$B^+ \to X_s^+\gamma$	0	0.1
$B^0 \to X_s^0\gamma$	0.5	0.1
Av. for $B^0 \to K^{*0}\gamma$	0.26	0.15
Av. for $B^0 \to K_S^0\pi^0\gamma$	0.22	0.17

generic B decays. The expected breakdown is given in Tab. 7.3. The allowed variations for C in each type are determined by a survey of the Review of Particle Physics [7]. For S in $b \to s\gamma$ decays the 1σ upper limit previously measured by *BABAR* is taken as the variation. For other B decays the root-mean-square width of a flat distribution between $-\sin(2\beta)$ and $+\sin(2\beta)$ is used as the variation. The total effective variation for S and C is then calculated as the weighted average of the individual variations. This is summarized in Tab. 7.4.

7.3.3 Fitting Procedure

The uncertainties associated with the fitting procedure come from the accuracy with which the signal and $B\overline{B}$ background PDFs are known, the degree to which the data match the MC, and any possible bias in the fit procedure. To address the uncertainties in the PDF parameters, each fixed parameter in the fit is varied within

its 1σ uncertainty, which is derived from the size of the MC samples. The effects on the measured signal S and C are added in quadrature.

To account for a possible disagreement between data and MC, the signal parameters of each PDF are released while fixing the background to the fit in data. The largest differences in S and C were observed when the signal L_2/L_0 shape was released, and this change was taken as the uncertainty. In the non-K^* region, the fixed $B\overline{B}$ background parameters dominate the uncertainty due to the PDFs.

To assess possible bias in the fit procedure, in addition to the validations described in Sec. 7.2.3, one final ensemble of simulated experiments was performed for each mass region using the parameters determined in the fit to data. This is discussed after the fit results are given in Sec. 7.4.

7.3.4 Tag-Side Interference

In the flavor tagging algorithm, the tag side is assumed to be dominated by a single decay amplitude; for example, that of $\overline{B}^0 \to D^+\pi^-$, in which the D decay produces a K^- meson corresponding to a $\overline{B}^0$ tag. However, this final state could be produced from a Cabibbo-suppressed $B^0 \to D^+\pi^-$ decay. The latter amplitude is suppressed by a factor of $r \approx |V_{ub}^* V_{cd}/V_{cb} V_{ud}^*| \approx 0.02$, with a relative weak phase difference of γ. Although it might seem that the interference would contribute to the effective mistag rate, it has been shown [60] that the effects on measured S and C are a function of r, the unitarity triangle angles β and γ, and the strong phase difference δ between the B^0 and $\overline{B}^0$ decay of the tag side. The differences ΔS and

ΔC between the measured and true (subscript-zero) values are

$$\Delta S = S_0 \left[2rG\cos\delta\cos(2\beta+\gamma)\right] + 2rC_0\sin\delta\cos(2\beta+\gamma)$$

$$\Delta C = C_0 \left[2r\cos\delta\left\{G\cos(2\beta+\gamma) - S_0\sin(2\beta+\gamma)\right\}\right]$$

$$- 2r\sin\delta\left\{S_0\cos(2\beta+\gamma) + G\sin(2\beta+\gamma)\right\}, \tag{7.7}$$

where $G = 2\mathrm{Re}\lambda_{K_S^0\pi^0\gamma}/(|\lambda_{K_S^0\pi^0\gamma}|^2+1)$. A dedicated *BABAR* study determined the effect of tag-side interference in context of the $\sin(2\beta)$ measurement in B^0 decays to $c\bar{c}s$ [61]. That work performed simulated MC experiments in which a wide range of values for r, δ, and γ were tested. The results of that study are used here as well, which is conservative in this analysis because the corrections are proportional to the true values of S and C, expected to be near zero.

7.3.5 Summary

The systematic uncertainties are summarized in Tab. 7.5. The uncertainties in the K^* region arise from several sources contributing at about the same level. However, in the non-K^* region the $B\overline{B}$ backgrounds contribute the most uncertainty, which is still significantly smaller than the statistical uncertainties.

Table 7.5: Summary of systematic uncertainties for $B^0 \to K^0_S \pi^0 \gamma$.

	K^* Region		non-K^* Region	
Source	ΔS	ΔC	ΔS	ΔC
Beamspot	0.007	0.002	0.007	0.002
SVT Alignment	0.010	0.010	0.010	0.010
Resolution Function	0.011	0.018	0.011	0.018
Bias Uncertainty	0.015	0.009	0.028	0.016
PDF Uncertainty	0.015	0.013	0.060	0.019
$S^{\rm bkg}_{B\bar{B}}$ and $C^{\rm bkg}_{B\bar{B}}$	0.008	0.002	0.060	0.018
Suppressed $B_{\rm tag}$ Decays	0.001	0.015	0.001	0.015
Total	0.028	0.030	0.091	0.040

Table 7.6: Fit results for the two $m(K^0_S \pi^0)$ regions. The SM expectations are given for S and C. Reported uncertainties are statistical and, when present, systematic.

	K^* Region	non-K^* Region	SM Expectation
S	$-0.03 \pm 0.29 \pm 0.03$	$-0.78 \pm 0.59 \pm 0.09$	$< \pm 0.10$
C	$-0.14 \pm 0.16 \pm 0.03$	$-0.36 \pm 0.33 \pm 0.04$	$< \pm 0.01$
Events in Sample	3884	6703	—
$N_{\rm sig}$	339 ± 24	133 ± 20	—
$N_{B\bar{B}}$	19 ± 27	167 ± 49	—

7.4 Results

The results of the fit to data are summarized in Tab. 7.6. Within the uncertainties, the results are consistent with SM expectations. The linear correlation coefficient between $S_{K^*\gamma}$ and $C_{K^*\gamma}$ is +0.050, while for $S_{K^0_S\pi^0\gamma}$ and $C_{K^0_S\pi^0\gamma}$ it is +0.015. Figure 7.11 shows signal-enhanced distributions for $m_{\rm ES}$ and ΔE created by cutting on the likelihood of the unplotted fit variables. Figure 7.12 shows the background-subtracted distributions of Δt in the K^* region, obtained with the sPlot event weighting technique [62]. This method uses the likelihood function to apply a

weight to each event, corresponding to its probability to be signal. Figure 7.13 shows the 68% confidence level boundary in the S-C plane for both mass regions. Finally, the sPlot technique is also used to determine the signal $m(K_S^0\pi^0)$ distribution, given in Fig. 7.14.

A final ensemble of simulated experiments was generated to evaluate any possible bias on S and C due to the fitting procedure, using the parameters determined in the fit to data. The pulls of S and C in the K^* region were consistent with Gaussian distributions of unit width; therefore, any possible bias is conservatively bounded by the ensemble in which signal MC was embedded into background samples generated from the PDFs (Sec. 7.2.3). However, in the non-K^* region, the post-fit ensemble shows a bias in the S parameter and a wide pull distribution for the C parameter. These effects are apparently because the data fit result is close to the physical boundary of $S^2 + C^2 \leq 1$ (Fig 7.13), and the problems disappear if the ensemble is generated with $S = C = 0$.

To determine any S-dependent bias, ensembles of simulated experiments were generated with different values of S. The ensemble that produced a result within one standard deviation of the uncorrected fit value (-0.843) was taken to indicate the true value. The ensemble fit results are given in Tab. 7.7. The final row shows that a generated value of -0.777 is consistent with the uncorrected value, within the uncertainty. Therefore, -0.777 is taken as the true value, with a systematic uncertainty of 0.028.

Although the C parameter is unbiased, the statistical error is underestimated by about 12%. The width of the C parameter distribution in the ensemble is taken

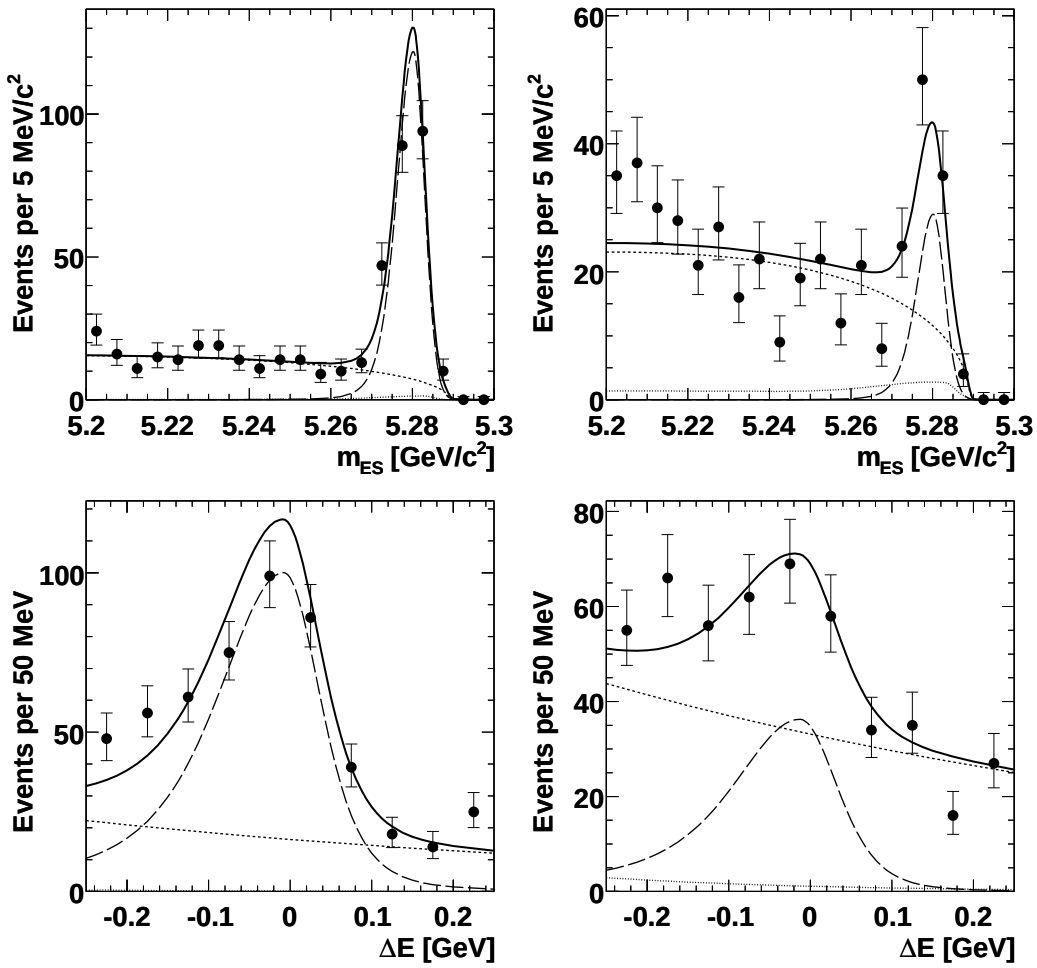

Figure 7.11: Signal-enhanced distributions for $m_{\rm ES}$ (top) and ΔE (bottom) for the K^* region (left) and the non-K^* region (right). We show the fit result (solid line) and PDFs for signal (long dashed), continuum (short dashed), and $B\overline{B}$ (dotted).

Table 7.7: Results of the procedure used to recreate the uncorrected value of $S_{K^0_S\pi^0\gamma}$ in data. Line zero is the result of the initial ensemble showing evidence of a bias.

Attempt	Generated S	Fit Average
0	-0.843	-0.932 ± 0.026
1	-0.754	-0.798 ± 0.027
2	-0.777	-0.829 ± 0.028

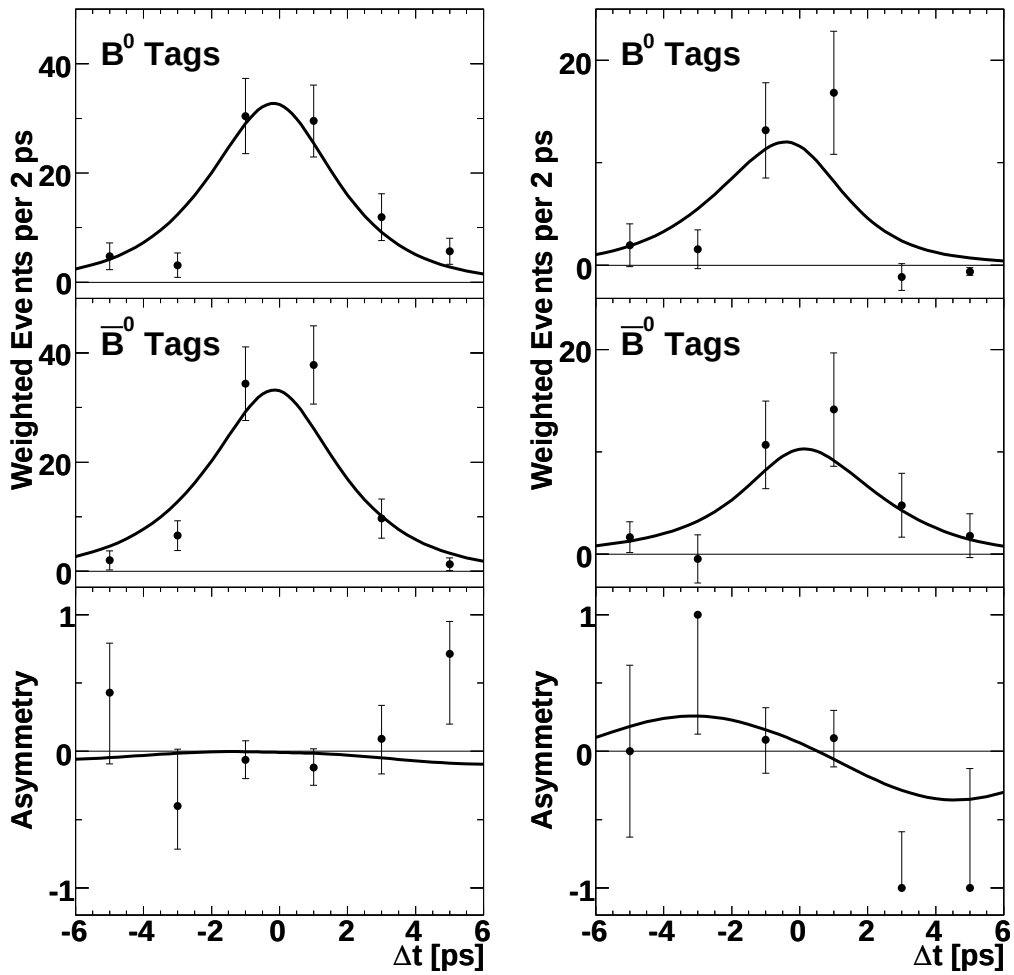

Figure 7.12: Background-subtracted distributions of Δt in the K^* region (left) and the non-K^* region (right), with $B_{\rm tag}$ tagged as B^0 (top) or $\overline{B}^0$ (center), and the asymmetry (bottom). The curves are the signal PDFs.

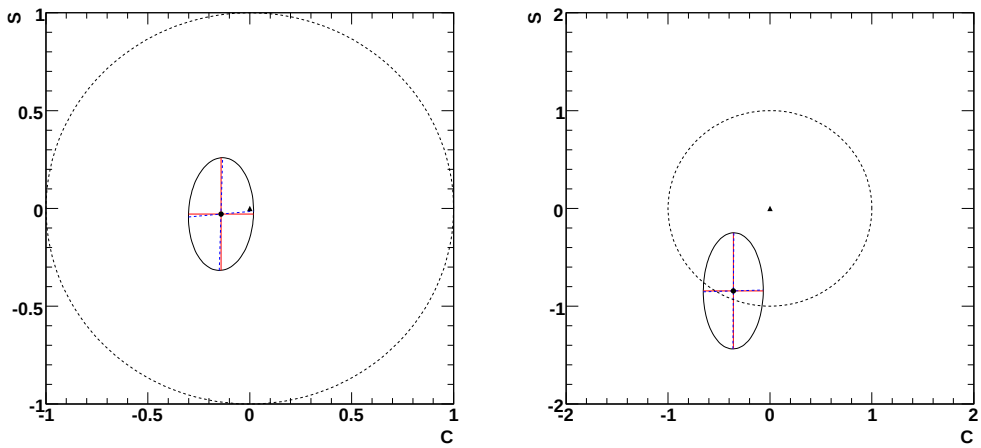

Figure 7.13: Results in the S-C plane showing the 1σ contour for the K^* region (left) and non-K^* region (right). The triangle marks $S = C = 0$, while the dashed circle indicates the physical boundary.

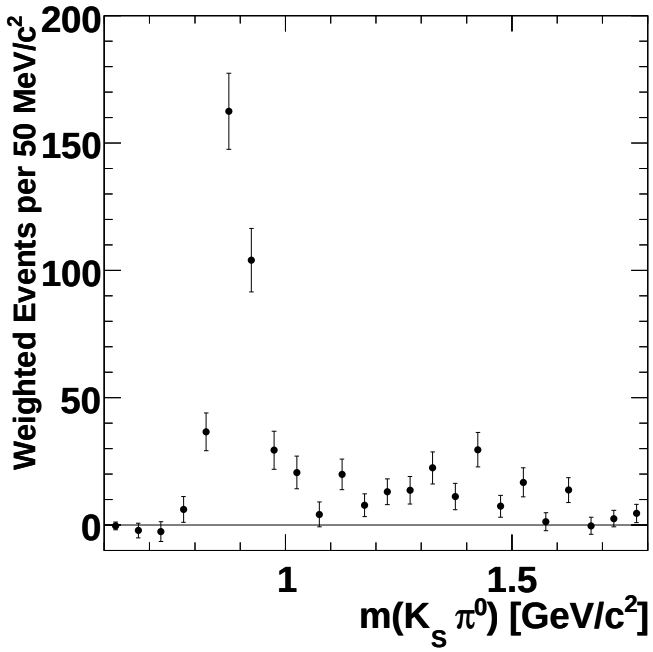

Figure 7.14: Background-subtracted distribution of $m(K_S^0\pi^0)$.

as the true statistical uncertainty, increasing it from 0.29 to 0.33.

This work, representing the full *BABAR* dataset at the $\Upsilon(4S)$ resonance, was published in Physical Review D in 2008 [63].

Chapter 8

Study of $B \to K\phi\gamma$

The $B \to K\phi\gamma$ process was first observed by the Belle Collaboration [64]. Based on $90\,\mathrm{fb}^{-1}$ of data at the $\Upsilon(4S)$ resonance, they measured the charged-mode branching fraction $\mathcal{B}(B^+ \to K^+\phi\gamma) = (3.4 \pm 0.9 \pm 0.4) \times 10^{-6}$ and set a limit on that of the neutral-mode of $\mathcal{B}(B^0 \to K^0\phi\gamma) < 8.3 \times 10^{-6}$ at 90% confidence level. This dissertation describes *BABAR*'s measurements of these modes, including a more stringent limit on the neutral mode's branching fraction and the first measurement of the direct *CP* asymmetry in the charged mode. This represents the first step toward future studies of other observables in the $B \to K\phi\gamma$ process, such as time-dependent *CP* violation in the neutral mode and an angular analysis of the decay products.

This analysis uses $207\,\mathrm{fb}^{-1}$ of data at the $\Upsilon(4S)$ resonance, collected between 1999–2004, corresponding to $(228.3 \pm 2.5) \times 10^6$ $\Upsilon(4S) \to B\overline{B}$ events. To optimize selection criteria and evaluate signal efficiency and background rejection, several samples of simulated Monte Carlo (MC) events are used, summarized in Table 8.1. The signal samples are given assuming a branching fraction of 3.4×10^{-6}, with $\phi \to K^+K^-$ and $K^0_S \to \pi^+\pi^-$ 100% of the time. The photon energy spectrum was generated according to the model of Kagan and Neubert [57] with b quark mass $m_b = 4.62\,\mathrm{GeV}/c^2$. The recoiling ϕK system decays according to phase space.

Table 8.1: Number of MC events used to evaluate selection criteria for $B \to K\phi\gamma$.

Sample	Number of Events	Equivalent Luminosity
uds Continuum	677.0M	$322\,\mathrm{fb}^{-1}$
Charm Continuum	425.6M	$327\,\mathrm{fb}^{-1}$
Generic B^+ B^-	584.0M	$1{,}112\,\mathrm{fb}^{-1}$
Generic B^0 $\overline{B}^0$	522.9M	$996\,\mathrm{fb}^{-1}$
$B^+ \to K^+\phi\gamma$ signal	234k	$133{,}495\,\mathrm{fb}^{-1}$
$B^0 \to K^0_S\phi\gamma$ signal	234k	$387{,}224\,\mathrm{fb}^{-1}$

8.1 Event Selection

8.1.1 Preselection

The preselection of K^0_S and photon candidates is the same as in Sec. 7.1.1. To make ϕ candidates, one of the tracks must pass no further than 1.5 cm from the interaction point (IP) in the x-y plane, and must be within ± 10 cm of the IP in z (loose criteria). The other track must satisfy those requirements as well as having at least 100 MeV/c of transverse momentum and 12 hits in the DCH (tight criteria). The four-momenta of these tracks (at the IP) must create an invariant mass within $\pm 30\,\mathrm{MeV}/c^2$ of the PDG mass.

Neutral B candidates are built from these K^0_S, ϕ, and γ candidates. Charged B candidates are built from the same ϕ and γ requirements as the B^0 candidates, and also from charged kaon candidates that satisfy the particle identification (PID) criteria described below. The combined four-momenta must create a B candidate within $0.4\,\mathrm{GeV}/c^2$ of the nominal B mass. If this is satisfied, then the entire decay chain is fit, and afterward the reconstructed B must have a mass m_{Rec} in the range $[-0.4, +0.3]\,\mathrm{GeV}/c^2$ around the B mass and a missing mass m_{Miss} within

$[5.19, 5.34]\,\mathrm{GeV}/c^2$. An asymmetric m_{Rec} selection is used in order to include a low-side tail caused by incomplete shower containment of the primary photon in the EMC. The preselection process is 36% efficient for the neutral mode and 47% efficient for the charged mode.

8.1.2 Kaon Identification

The charged kaon from the B^+ and those from the ϕ decays are subject to loose PID criteria based on $\mathrm{d}E/\mathrm{d}x$ in the tracking system and the Cherenkov angle measurement from the DIRC. Likelihoods for the SVT and DCH $\mathrm{d}E/\mathrm{d}x$ measurements are formed based on the difference between the measured and expected $\mathrm{d}E/\mathrm{d}x$ values. This residual is divided by its corresponding uncertainty to form a pull, which is then parameterized as a bifurcated Gaussian distribution in the SVT and as a single Gaussian in the DCH. The likelihood in the DIRC is represented by a histogram, binned in momentum and Cherenkov angle and filled based on pure MC samples. The likelihoods for SVT, DCH, and DIRC are multiplied to create an overall likelihood $\mathcal{L}$ for each particle hypothesis. To isolate kaon tracks for this analysis, the requirements are $\mathcal{L}_K/(\mathcal{L}_K + \mathcal{L}_\pi) > 0.2$ or $\mathcal{L}_p/(\mathcal{L}_p + \mathcal{L}_\pi) > 0.2$.

The performance of this PID selector is evaluated on clean samples in both data and MC. The kaon efficiency, pion fake rate, and proton fake rate are given in Fig. 8.1. Although protons are likely to pass this selector, they do not constitute a large source of background for ϕ reconstruction.

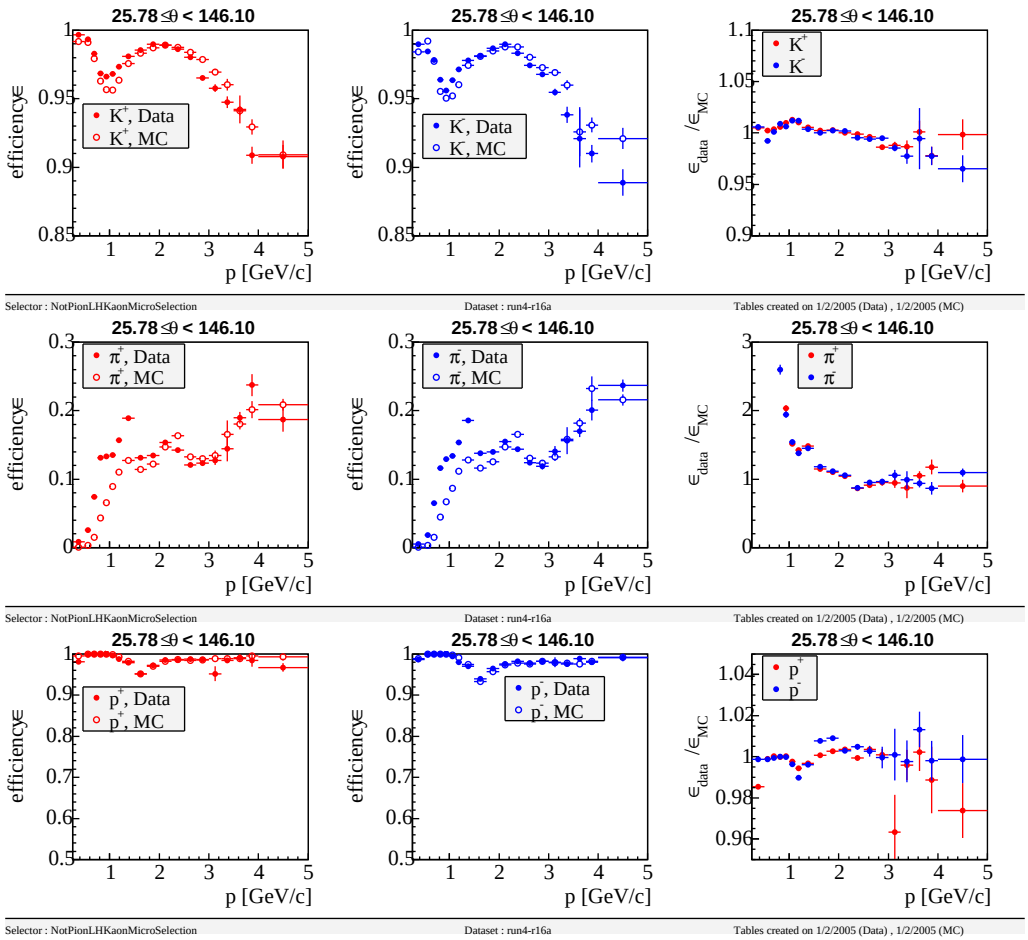

Figure 8.1: The probability that kaons, pions, and protons will pass the kaon PID selector described in the text. The angular range corresponds to the DIRC acceptance.

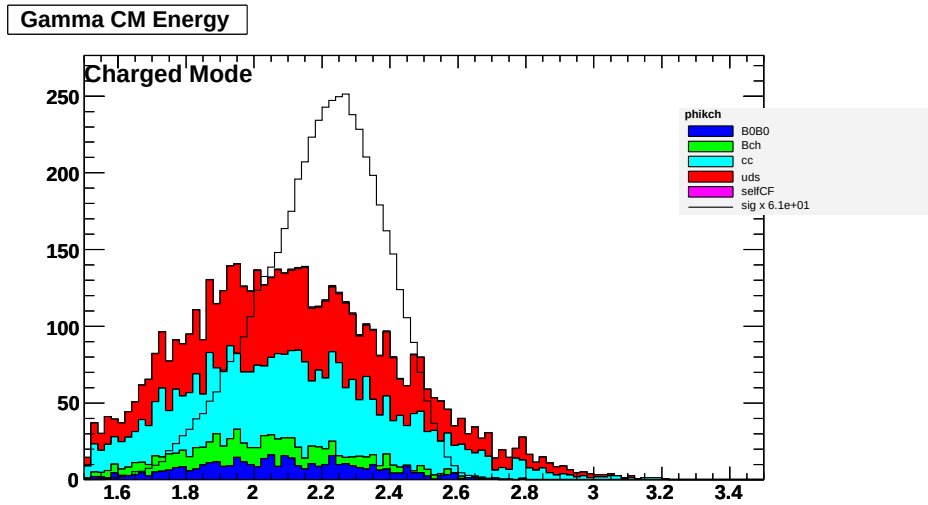

Figure 8.2: Monte Carlo distributions of the primary photon's CM energy in $B^+ \to K^+\phi\gamma$ (units of GeV). The blue and green histograms are background photons from the neutral and charged generic $B\overline{B}$ samples, respectively. Red is light continuum (u, d, s) and cyan is charm continuum. All backgrounds are scaled to $207\,\mathrm{fb}^{-1}$, while the solid-line histogram is signal MC with arbitrary normalization.

8.1.3 Final Selection

After preselection, the majority of the candidate events are from continuum background processes in which events pass the criteria by chance. There are approximately two and three million background events in the neutral and charged modes, respectively, compared to 45 and 170 expected signal events.

The lower bound of the ϕ-K system invariant mass ($1.5\,\mathrm{GeV}/c^2$) introduces an upper limit on the photon energy in the B rest frame of about $2.4\,\mathrm{GeV}$. After accounting for resolution and smearing from the B meson momentum in the e^+e^- center of mass (CM) frame (Fig. 8.2), an upper limit of $2.6\,\mathrm{GeV}$ is placed on the

CM photon energy to remove continuum background. To reduce background from π^0 or η decays that create a fake photon candidate, the EMC second moment must be less than 0.0022. The photon candidate must be well-isolated: at least 25 cm from any other charged or neutral EMC clusters. Finally, the photon is combined with all other photons in the event to explicitly search for combinations creating a π^0 (η) candidate. A primary photon is vetoed if its diphoton mass is between 115–155 MeV/c^2 (470–620 MeV/c^2) when combined with another photon of energy greater than 50 MeV (250 MeV). These rejection criteria are 77% efficient for signal and 30% efficient for background.

Both the K_S^0 and ϕ meson candidates must be within 10 MeV/c^2 of their nominal mass; this corresponds to about three and five times the mass resolution, respectively. The track pair for each must fit to a production vertex with a probability greater than 0.1%. Additionally, for K_S^0 candidates, the reconstructed flight length must be greater than three times the error on that quantity. One of the greatest reductions in background is achieved through the PID criteria applied to the charged kaons from the ϕ mesons. Collectively, they are 85% efficient for signal but only 6% efficient for background.

The ϕ-K system is subject to two additional constraints. Firstly, cut optimization based on the ratio of the number of signal events to the square root of signal-plus-background in MC indicates that an upper limit 3.0 GeV/c^2 should be placed on the ϕ-K invariant mass, $m(\phi K)$. At higher masses, continuum backgrounds become dominant (Fig. 8.3). The low signal at higher mass is also supported by inclusive determinations of the hadronic mass spectrum in $b \to s\gamma$ measurements [65]. Another

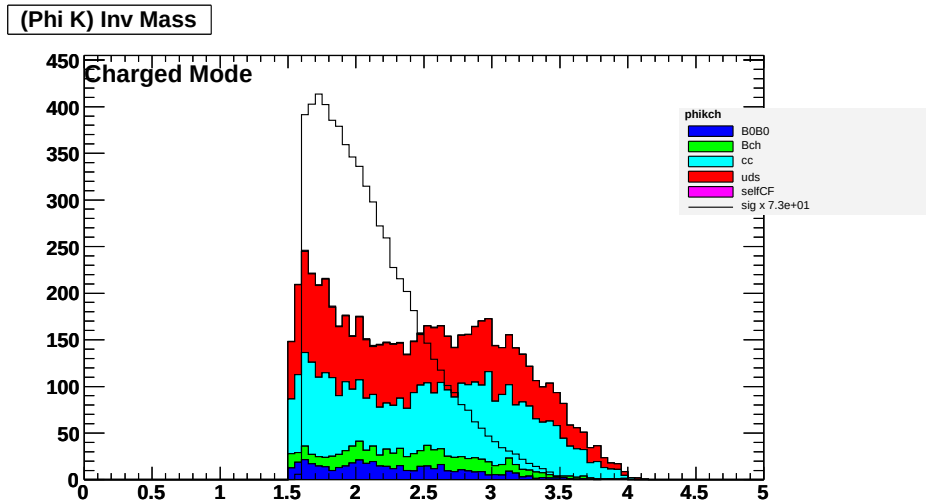

Figure 8.3: MC distributions of ϕ-K^+ invariant mass in $B^+ \to K^+\phi\gamma$ (units of GeV/c^2). Color coding and normalizations are the same as Fig. 8.2.

constraint on the ϕ-K system only applies to the neutral mode, in which the $m(\phi K)$ spectrum shows a peak due to D^0 decays. These are removed by a veto window of $\pm 10\,\mathrm{MeV}/c^2$ around the D^0 mass. There is no significant corresponding peak in the charged mode because $D^+ \to K^+\phi$ decays are doubly Cabibbo-suppressed.

As in the $B^0 \to K_S^0\pi^0\gamma$ analysis, the event-shape ratio L_2/L_0 is required to be less than 0.55, and it is later used in a maximum likelihood fit to discriminate continuum from $B\overline{B}$ events. A limit on the CM polar angle of the B $|\cos(\theta_B^*)| < 0.90$ is also required.

After all criteria have been applied, selected events contain an average of 1.01 B candidates in the neutral mode and 1.07 in the charged mode. To pick the best candidate a χ^2 is formed from the ϕ mass and, in the neutral mode, the K_S^0 mass:

$$\chi^2 = \frac{(m_\phi - m_{\mathrm{PDG}})^2}{\sigma_\phi^2 + (\Gamma_\phi/2.35)^2} + \frac{(m_{K_S^0} - m_{\mathrm{PDG}})^2}{\sigma_{K_S^0}^2}, \tag{8.1}$$

where σ_ϕ^2 and $\sigma_{K_S^0}^2$ are the variances of the ϕ and K_S^0 masses, Γ_ϕ is the ϕ natural width, and it is divided by 2.35 to convert a full width at half-maximum to an effective Gaussian width. The candidate with the smallest χ^2 is selected . Multiple candidates due to alternate charged kaons or photons are found to be negligible in the signal MC. The total selection efficiencies for the charged and neutral modes are 22% and 15%.

8.1.4 Characterization of Backgrounds

After the event selection, there are 443 neutral-mode events and 3267 charged-mode ones, of which about 20 and 85 are expected to be signal. The majority of the background events are due to continuum combinatorics. However, there are three classes of background that peak in $m_{\rm Miss}$ and $m_{\rm Rec}$: $B \to \phi K \pi^0$, $B \to \phi K \eta$, and $B \to K^+K^-K$. The reconstruction efficiency is 0.57% for $B^0 \to \phi K_S^0 \pi^0$ and 0.72% for $B^+ \to \phi K^+ \pi^0$, but the branching fractions are unknown. The contribution from nonresonant $B \to K^+K^-K$ decays under the ϕ peak can be estimated from the ϕ mass sidebands. The corrections for these backgrounds are described in Sec. 8.3.

8.2 Determination of Signal and Background Yields

The numbers of signal and background events are extracted using an unbinned maximum likelihood fit according to Eq. 5.8. Here I describe the PDFs $\mathcal{P}_{\rm sig}$ and $\mathcal{P}_{\rm bkg}$, which are functions of $m_{\rm Miss}$, $m_{\rm Rec}$, L_2/L_0, and $\cos(\theta_B^*)$. To measure the direct CP asymmetry in the charged mode, $A_{CP} = \frac{\Gamma(B^-)-\Gamma(B^+)}{\Gamma(B^-)+\Gamma(B^+)}$, the data set is split according

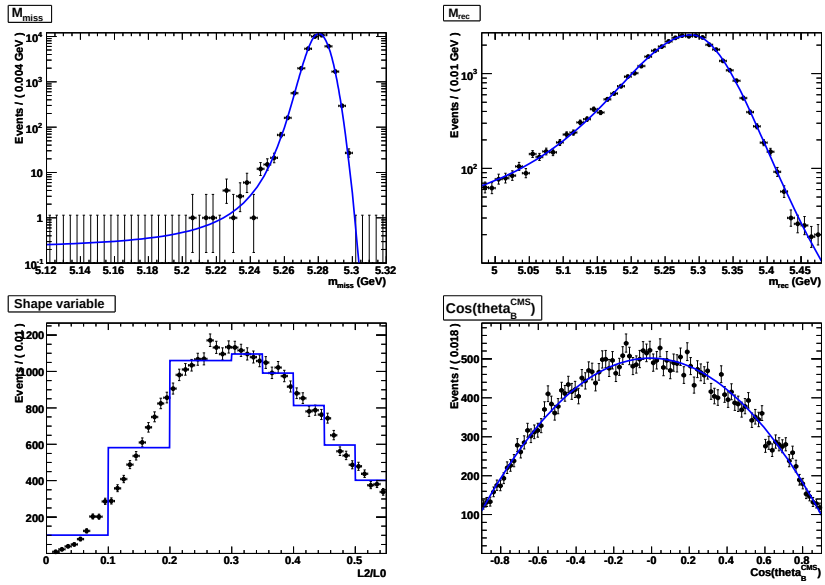

Figure 8.4: Distribution of the discriminating variables used in the maximum likelihood fit for $B^0 \to K_S^0 \phi \gamma$. The dots represent the distribution for signal MC events, and the line is the projection of the fitted PDF.

to the charge of the B and the number of B^+ and B^- events are used to determine the total signal and the asymmetry:

$$N^{\pm} = \frac{1}{2}(1 \mp A_{CP})N_{\text{sig}}. \tag{8.2}$$

Examples of the signal distributions are given in Fig. 8.4. Monte Carlo studies (Sec. 8.2.2) show that any correlations among the observables are negligible. Therefore, the PDFs may be parameterized as the product of one-dimensional distributions. For the signal m_{Miss} and m_{Rec}, the bifurcated Gaussian distribution of Eq. 7.3 is used. The background m_{Miss} distribution is the threshold function of Eq. 7.4. The threshold endpoint is set on an event-by-event basis by $m_0 = \sqrt{s} - m_{B^0}$. The background distribution of m_{Rec} is modeled as a second-degree polynomial. The

L_2/L_0 distribution is binned for both signal and background as in the $B^0 \to K_S^0\pi^0\gamma$ analysis. The shape of the $\cos(\theta_B^*)$ distribution for both signal and background are second-degree polynomials. In the case of perfect detector acceptance, the signal $\cos(\theta_B^*)$ distribution would be $1 - \cos^2(\theta_B^*)$; in practice the signal fit finds $1 - 0.012\cos(\theta_B^*) - 0.96\cos^2(\theta_B^*)$.

8.2.1 Determination of Fixed Parameters

A control sample of $B^0 \to K^{*0}\gamma$ with $K^{*0} \to K^+\pi^-$ was used to determine the signal shapes. Event selection is essentially the same as that described in Sec. 8.1 where applicable. The only difference is tighter PID criteria on the charged kaon (80–90% efficient, less than 5% fake rate). The K^{*0} mass was selected in the range 0.8–1.0 GeV/c^2 and its helicity angle θ_{K^*} was subject to $|\cos\theta_{K^*}| < 0.9$. The sample contained 7354 background events and 1692 signal events. The signal PDF parameters were obtained in a fit to this sample, and were subsequently fixed in the fit to data for $B \to K\phi\gamma$. Projection plots of the fit variables for the control sample are given in Fig. 8.5.

8.2.2 Fit Validation

To verify that the fit gives sensible results for the central value and uncertainty of the number of signal events, an ensemble of 1,000 simulated experiments each are generated for the neutral and charged modes. The background component is sampled from the PDFs (fit to MC) while the signal component is sampled from the

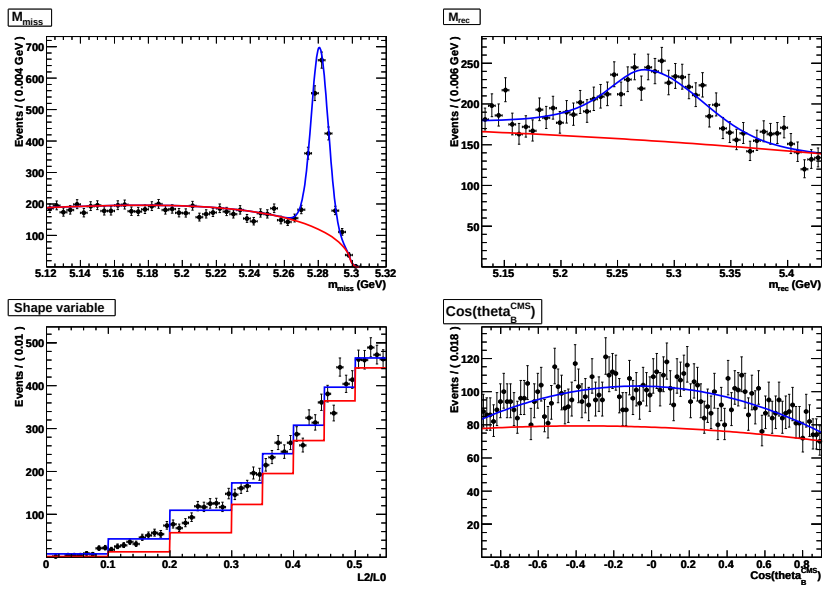

Figure 8.5: Fits to the $B^0 \rightarrow K^{*0}\gamma$ control sample, used to obtain the signal parametrization for $B \rightarrow K\phi\gamma$. The blue curve is the signal component, while the red is the background.

fully-reconstructed MC. The fit is performed on each experiment, and the results examined for evidence of a bias. In the neutral mode, an average of 20.19 signal events, $N_{\rm sig}$, were generated, and the mean of the ensemble was found to be 19.95 ± 0.20, a difference of $+0.26 \pm 0.20$. In the charged mode, 77.31 signal events were generated on average, with a mean fit of 76.80 ± 0.41 and a difference of 0.51 ± 0.42. These results are consistent with no bias. For each experiment, a pull is defined by the residual between the generated and measured $N_{\rm sig}$, divided by the uncertainty of $N_{\rm sig}$. The widths of the pull distributions are 1.073 ± 0.024 in the neutral mode and 1.032 ± 0.023 in the charged mode. These are consistent with 1, indicating that the uncertainties are correctly evaluated.

A second cross-check was performed to evaluate the effect of not including an explicit $B\overline{B}$ parameterization in the fit. A cocktail of non-peaking $B\overline{B}$ backgrounds was fit in MC using the same shapes as the continuum, but with different parameters. These PDFs were used to generate ensembles of experiments, each containing about 500 $B\overline{B}$ events for the charged mode and 80 for the neutral mode. Continuum events were also generated from PDFs, while signal events were extracted from the fully-simulated MC. When the ensembles were fit with only signal and background components, a bias on the number of signal events of -0.06 ± 0.20 was found in the neutral mode, and a bias of $+4.07 \pm 0.45$ in the charged mode. The signal yields are corrected to offset these biases.

8.3 Background Subtraction

Background from $B \to KK^+K^-\gamma$ decay is subtracted using information from the ϕ mass sidebands in data. The low and high sidebands are defined as $989 < m_\phi < 1009\,\mathrm{MeV}/c^2$ and $1029 < m_\phi < 1049\,\mathrm{MeV}/c^2$. Assuming that the branching fraction for this process is independent of $m(K^+K^-)$ within $\pm 30\,\mathrm{MeV}/c^2$ of the ϕ mass peak, the number of fitted signal events in the fit region $N_{\mathrm{sig,fit}}$ may be written:

$$N_{\mathrm{sig,fit}} = N_{\mathrm{sig}} + 1/3 N_{\mathrm{nonres}}, \tag{8.3}$$

where N_{sig} is the true number of $B \to K\phi\gamma$ events and N_{nonres} is the number of $B \to KK^+K^-\gamma$ that do not involve a ϕ. The factor of 1/3 corresponds to the fit region being 1/3 the size of the fit region plus the two sidebands defined above. The number of fitted signal events in both sidebands $N_{\mathrm{sb,fit}}$ can be written:

$$N_{\mathrm{sb,fit}} = \frac{\alpha}{1-\alpha} + 2/3 N_{\mathrm{nonres}}, \tag{8.4}$$

where α is the fraction of $B \to K\phi\gamma$ events that fall into the sideband region within $\pm 30\,\mathrm{MeV}/c^2$ of the ϕ peak. In the MC α is found to be 0.088. Solving Eqs. (8.3) and (8.4) for N_{sig}, one obtains:

$$N_{\mathrm{sig}} = \frac{1-\alpha}{1-3/2\alpha}(N_{\mathrm{sig,fit}} - 1/2 N_{\mathrm{sb,fit}}). \tag{8.5}$$

Applying Eq. (8.5) to the data gives additive corrections to the fit yield of $+0.4 \pm 1.6$ in the neutral mode and -1.0 ± 4.4 in the charged mode. These uncertainties are dominated by the statistical uncertainty of the fits to the sidebands.

The effects of background from $B \to K\phi\pi^0$ and $B \to K\phi\eta$ are estimated and corrected using samples of $B \to \phi K^*$ MC. This process has branching fractions of

$(9.5 \pm 0.8) \times 10^{-6}$ (neutral) and $(10.5 \pm 1.5) \times 10^{-6}$ (charged) [7]. Based on the MC efficiency, contamination of 0.72 neutral events and 2.62 charged events are expected. In an ensemble of experiments, embedding this amount of background leads to biases of 0.27 ± 0.16 neutral and 1.98 ± 0.32 charged events. These are subtracted from the fit yield in data.

Because there have been no branching fraction measurements of non-resonant $B \to K\phi\pi^0$ and $B \to K\phi\eta$ decays, the conservative assumption is used that contamination due to the former is no more than one-third that of $B \to \phi K^*$, and that the contamination due to the latter is no more than $B \to \phi K^*$. These lead to an estimated bias of 0.51 ± 0.16 neutral events and 2.86 ± 0.32 events. Because these latter sources of contamination are not well-constrained, the full bias is taken as a systematic uncertainty, without a correction.

8.4 Systematic Uncertainties

The systematic uncertainties break down into three parts: additive corrections and uncertainties that are associated with the yields, multiplicative corrections that are associated with the efficiency, and uncertainties on the CP asymmetry that do not cancel in the ratio.

8.4.1 Signal Yields

The corrections to the signal yields and their associated uncertainties are summarized in Table 8.2. They were discussed in Sec. 8.3.

Table 8.2: Additive systematic corrections in $B \to K\phi\gamma$.

Source	Neutral Mode	Charged Mode
$B\overline{B}$ background	$+0.06 \pm 0.20$	-4.1 ± 0.5
Nonresonant $B \to KK^+K^-\gamma$	$+0.4 \pm 1.6$	-1.0 ± 4.4
$B \to \phi K^*$	-0.27 ± 0.16	-1.98 ± 0.32
$B \to \phi K\pi^0/\eta$	± 0.5	± 2.9

There is an additional uncertainty associated with fixing the signal PDF parameters in the fit. This is evaluated by allowing each parameter to vary by its $\pm 1\sigma$ uncertainty, which is determined by the statistics of the $B^0 \to K^{*0}\gamma$ control sample, yielding an uncertainty of $^{+0.53}_{-0.45}$ neutral events and $^{+4.8}_{-4.2}$ charged events. The total additive uncertainty is $^{+1.8}_{-1.7}$ neutral-mode events and $^{+7.3}_{-6.9}$ charged-mode events.

8.4.2 Selection Efficiencies

The efficiencies quoted in Sec. 8.1.3 were determined in MC, and must be corrected for known reconstruction efficiency differences between data and MC.

Charged-particle tracking efficiencies are determined using $e^+e^- \to \tau^+\tau^-$ events in which one τ decays to a single lepton and a neutrino, while the other decays hadronically to three charged tracks and a neutrino. Selection criteria are applied to all but one of the tracks, and the frequency with which the final track passes the criteria determines a relative efficiency. Based on a dedicated study performed by the *BABAR* tracking group, an efficiency correction to the MC of -0.5% per track must be applied to tracks passing loose selection criteria (defined in Sec. 8.1.1). This applies to the charged kaon in the B^+ mode as well as to the looser kaon used in ϕ reconstruction. The correction comes with an uncertainty of 1.4% per track. For the

tighter kaon candidates used in the ϕ reconstruction, the correction is -0.8% with an uncertainty of 1.4%. Therefore, the efficiency correction factor for the charged mode in MC is 0.982 ± 0.042, while for the neutral mode it is 0.987 ± 0.028.

The tracks from the K_S^0 decay are handled separately. Events with K_S^0 candidates are selected in data and MC by requiring hadronic events with at least five charged tracks to have an oppositely-charged pair that form a common vertex. The K_S^0 candidate mass must be within $25\,\mathrm{MeV}/c^2$ of the PDG mass. Combinatoric backgrounds are reduced by requiring all candidate vertices to be at least 3 mm from the beam spot. Candidates are binned according to their transverse momentum (index i, four bins up to $4.0\,\mathrm{GeV}/c$), polar angle (index j, eight bins from 7° to 156°), and transverse flight length (index k, nine bins from 0.3 to 40 cm). The MC is assumed to be perfect with respect to tracking in the first flight length bin from 0.3–1.3 cm. The correction is then given by

$$C_{ijk} = (N_{ijk}^{\mathrm{data}}/N_{ijk}^{\mathrm{MC}})/(N_{ij1}^{\mathrm{data}}/N_{ij1}^{\mathrm{MC}}), \tag{8.6}$$

where $k = 1$ corresponds to the 0.3–1.3 cm bin. Correction tables are provided by the tracking group for common extra criteria, such as those applied in this analysis (a mass cut of $\pm 10\,\mathrm{MeV}/c^2$ and a flight length significance cut of 3σ). Based on the K_S^0 candidates in the $B^0 \to K_S^0\phi\gamma$ analysis, the overall efficiency correction factor is 0.975 ± 0.014. An additional small uncertainty in the efficiency comes from requiring the vertex fit probability to be greater than 0.001. The fraction of K_S^0 candidates selected in this analysis surviving the vertex probability requirement was compared in data and MC by fitting the K_S^0 mass distribution. The integral of the peak was

taken as the number of true K_S^0 candidates. The efficiency difference of 0.5% is taken as the as the uncertainty, to be added in quadrature with the above 1.4%.

The ϕ reconstruction efficiency is also affected by the mass and vertex probability criteria. The ϕ mass peak is fit in data and MC using the convolution of a Breit-Wigner and a Gaussian distribution. The width of the former is set to the PDG value, while that of the latter is determined in MC. The number of ϕ candidates in the peak is then compared in data and MC, before and after each cut. The efficiency difference of the vertex probability cut is 1.7%, while for the mass cut it is only 0.06% different. This is consistent for both the neutral and the charged mode samples.

Reconstruction of the ϕ is also affected by the PID requirements. This was quantified by fitting the ϕ mass in three cases:

- The K^+ passes the PID criteria (regardless of whether the K^- passes)
- The K^- passes the PID criteria
- Both K^+ and K^- pass the PID criteria.

The integral of the ϕ mass peak in each case is, respectively, N^+, N^-, and $N^\pm$. Assuming that the PID criteria are equally efficient for K^+ as K^-, the efficiency ε is:

$$\varepsilon = \frac{2N^\pm}{N^+ + N^-}. \tag{8.7}$$

In the neutral mode, the ratio $\varepsilon_{\text{data}}/\varepsilon_{\text{MC}}$ is 1.0115±0.0089, while in the charged mode it is 1.014 ± 0.0066. To be conservative, the charged-mode difference from unity is

taken as the systematic uncertainty per kaon track, leading to 2.8% uncertainty in the neutral mode and 4.2% in the charged mode.

Single photon detection efficiency is evaluated by the *BABAR* neutrals group in two ways. In the first method the rate of reconstructed τ decays to a charged pion and a neutrino is compared to that of τ decays to a charged ρ and a neutrino. The data and MC efficiencies are consistent within 3%. Half of this is taken as the single-photon uncertainty, which, when combined with the relative uncertainties of the τ branching fractions, yields a 1.8% uncertainty on the single-photon efficiency. This is valid at photon energies below 2.5 GeV, after which point merged π^0 mesons (that make only a single bump in the EMC) contaminate the sample. The data-MC agreement at higher energies is checked using samples of $e^+e^- \to \mu^+\mu^-\gamma$ events, in which the direction and energy of the photon can be inferred from the muon tracks and the initial beams. The rate at which the EMC detects such photons can be determined over an energy range from 1–7 GeV. A correction of 0.993 ± 0.007 is derived. This correction is applied, but with the 1.8% error from the π^0 study as the systematic uncertainty, because only about half of the $B \to K\phi\gamma$ photons have energy greater than 2.5 GeV.

The measured branching fraction is sensitive to how much of the hadronic mass spectrum falls within the range between threshold (1.5 GeV) and the 3.0 GeV upper limit. One extreme difference from the phase space model in MC would be if all of the $B \to K\phi\gamma$ events proceeded through the $K_2(1770)$ resonance, which has been observed to decay to ϕK. Based on the spectrum found in the data (Fig. 8.9 in Sec.8.5), no more than half could come through the $K_2(1770)$. An alternate spec-

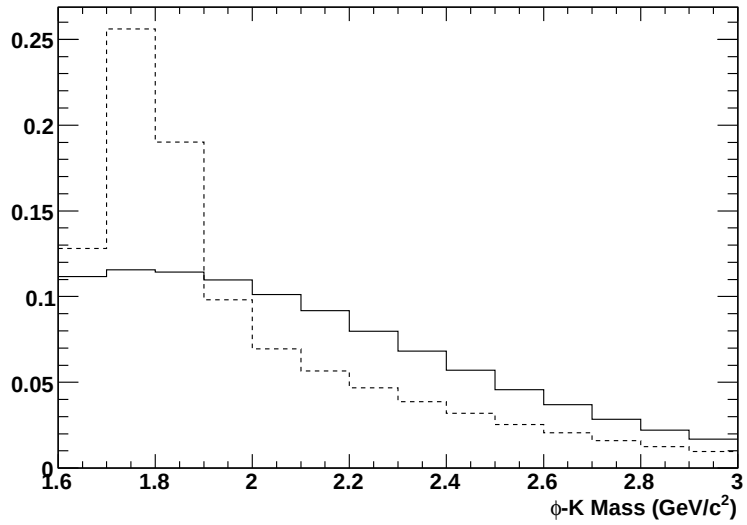

Figure 8.6: Comparison of the $m(\phi K)$ spectrum used in signal MC (solid) and an alternate spectrum as described in the text (dashed). Both histograms have been normalized to 1.

trum is constructed in which half is phase space and half comes from the $K_2(1770)$ (Fig. 8.6). After re-weighting the MC to correspond to this spectrum, the neutral-mode efficiency only changes by 0.4% (relative), while the charged mode changes by 2.6%. These differences are taken as the systematic uncertainty associated with the fragmentation model.

Finally, there are uncertainties associated with the efficiency of the cut on L_2/L_0, and the π^0/η veto of the primary photon. The effect of the L_2/L_0 cut was evaluated on a large sample of $B^+ \to \tilde{D}^+\pi^0$, where $\tilde{D}^+$ can be D^+, D^{*+}, D^{**+}. The requirement $L_2/L_0 < 0.55$ is different by 1.2% between data and MC. For the π^0/η veto, a control photon of 2.5 GeV, generated uniformly with respect to angle in the CM frame, was combined with all other photons in the event. The π^0 and η

Table 8.3: Summary of the systematic efficiency corrections in $B \to K\phi\gamma$.

Source	Neutral Correction	Charged Correction
Kaon Tracking	0.987	0.982
K_S^0 Efficiency	0.975	1
Single Photon Efficiency	0.993	0.993
Total Efficiency Correction	0.956	0.975

Table 8.4: Summary of the multiplicative systematic uncertainties in $B \to K\phi\gamma$.

Source	Uncertainty (%)	
	$B^0 \to K_S^0\phi\gamma$	$B^+ \to K^+\phi\gamma$
Kaon Tracking	2.8	4.2
K_S^0 Efficiency	1.5	0
ϕ Efficiency	1.7	1.7
Particle ID	2.8	4.2
Single Photon Efficiency	1.8	1.8
Hadronic Fragmentation Model	0.4	2.6
L_2/L_0 Cut	1.2	1.2
π^0/η Veto	1.0	1.0
Efficiency Uncertainty	5.2	7.1
$B\overline{B}$ Counting	1.1	1.1

veto efficiencies for these control photons was compared in data and MC, and the difference found to be 1%.

The remaining uncertainty on the branching fraction measurements is the 1.1% $B\overline{B}$ counting uncertainty (Sec. 4.3).

A summary of the multiplicative efficiency corrections is given in Table 8.3. The systematic uncertainties on the efficiency are summarized in Table 8.4. The final, corrected efficiencies and their systematic uncertainties are $(15.3 \pm 0.8)\%$ for the neutral mode and $(21.9 \pm 1.6)\%$ for the charged mode.

8.4.3 Charge Asymmetry

Most of the uncertainties discussed so far cancel in the ratio taken to calculate A_{CP}. One that does not is associated with the fixed signal PDF parameters. Varying these by $\pm 1\sigma$ yields an A_{CP} uncertainty of 2.2%. In order to bound the uncertainty on any possible charge dependence of track reconstruction efficiencies in the *BABAR* detector, an effective A_{CP} floating parameter is included in the background likelihood function. The asymmetry is found to be zero within an uncertainty of 1.8%. The peaking backgrounds cannot be separated from the signal in the A_{CP} measurement, so their contribution to the signal asymmetry is bounded by the following procedures. Earlier analyses of $B^+ \to \phi K^{*+}$ [66, 67] show that the charge asymmetry is zero to within 15%. Because contamination from this source is small, its effect on A_{CP} is negligible. For the other peaking backgrounds, A_{CP} is varied by $\pm 58\%$, which is the root-mean-square width of a flat distribution between -1 and $+1$. This is multiplied by the expected fractional contamination in the data to obtain the systematic uncertainty. For nonresonant $B^+ \to \phi K^+(\pi^0/\eta)$ this results in 1.8% uncertainty, while for $B^+ \to K^+K^+K^-\gamma$ it is 3.5%. Adding all of these in quadrature yields a total systematic uncertainty of 4.8%.

8.5 Results

After applying the systematic corrections discussed previously, the fit to data yields 8 ± 6 (stat) ± 2 (syst) $B^0 \to K^0_S\phi\gamma$ candidates and 85 ± 15 (stat) ± 7 (syst) $B^+ \to K^+\phi\gamma$ candidates. The charge asymmetry in the latter sample is measured

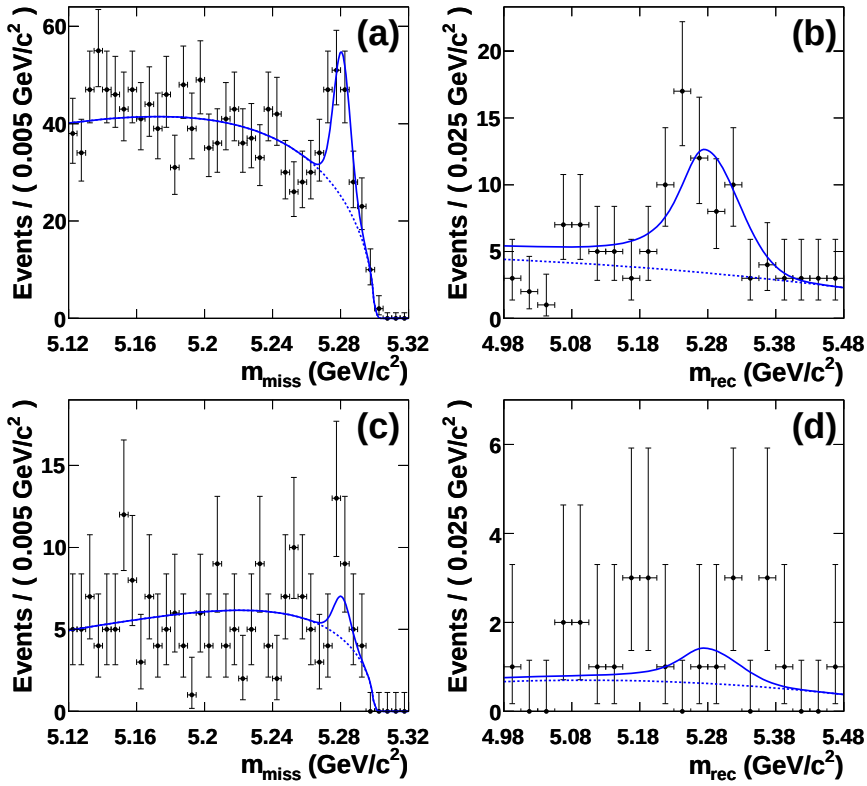

Figure 8.7: Missing mass (a) and reconstructed mass (b) fits for the charged mode and the neutral mode (c,d). The dotted curves show the background contribution while the solid curves show the sum of signal and background.

to be

$$A_{CP} = (-26 \pm 14\ (\text{stat}) \pm 5\ (\text{syst}))\%.$$

Projections of the fit PDF in m_{Miss} and m_{Rec} are given in Fig. 8.7. The signal is enhanced in these plots by requiring $L_2/L_0 < 0.48$ and $|\cos(\theta_B^*)| < 0.8$. In the m_{Miss} plots, we also require $5.05 < m_{\text{Rec}} < 5.4\,\text{GeV}/c^2$, while for the m_{Rec} plots we require $5.27 < m_{\text{Miss}}$.

The branching fractions $\mathcal{B}$ are calculated assuming equal production of charged

and neutral B mesons by the $\Upsilon(4S)$ resonance:

$$\mathcal{B} = \frac{N_{\text{sig}}}{N_{B\overline{B}} \cdot \varepsilon \cdot b}, \tag{8.8}$$

where $N_{B\overline{B}}$ is the number of $B\overline{B}$ pairs, ε is the total reconstruction and selection efficiency, and b accounts for the ϕ and K_S^0 branching fractions. In the charged mode $b = \mathcal{B}(\phi \to K^+K^-)$, while in the neutral mode $b = [\mathcal{B}(\phi \to K^+K^-)][\frac{1}{2}\mathcal{B}(K_S^0 \to \pi^+\pi^-)]$. The measured branching fractions are

$$\mathcal{B}(B^0 \to K^0\phi\gamma) = (1.3 \pm 1.0 \text{ (stat)} \pm 0.3 \text{ (syst)}) \times 10^{-6}$$

and

$$\mathcal{B}(B^+ \to K^+\phi\gamma) = (3.5 \pm 0.6 \text{ (stat)} \pm 0.4 \text{ (syst)}) \times 10^{-6}.$$

The consistency of the branching fractions with the hypothesis of isospin symmetry is evaluated with an ensemble of 1,000 simulated experiments. The number of signal events is given in each mode by the average branching fraction, 2.8×10^{-6}. Based on the distribution of the fitted differences in branching fractions, there is an 8.9% probability to measure a difference in branching fractions at least as large as that observed in the data.

Because there is no statistically significant signal in the neutral mode, an upper limit is determined using the likelihood function. The value of the likelihood as a function of branching fraction is found by varying the number of signal events and refitting the data at each point. Systematic uncertainties are included by smearing the resulting likelihood curve with a Gaussian distribution of width equal to the systematic uncertainty (Fig. 8.8). The 90% confidence level upper limit $\mathcal{B}_{\text{UL}}$ is

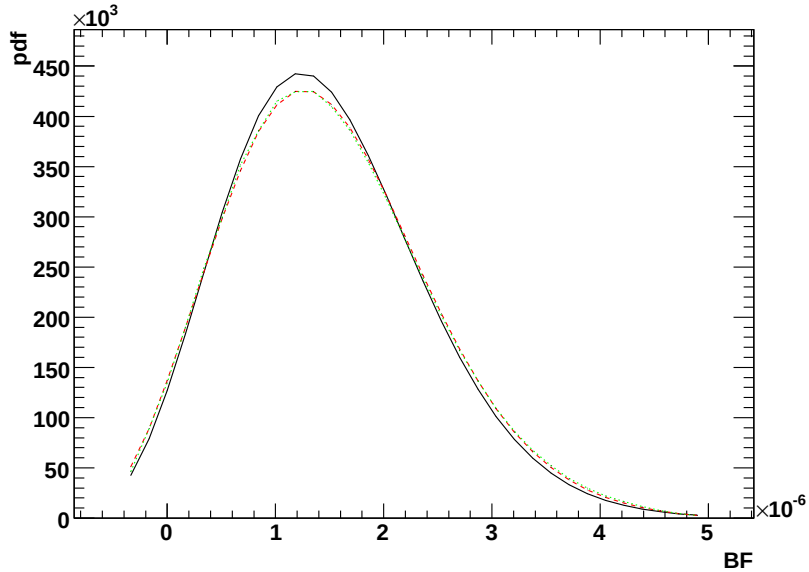

Figure 8.8: Scan of the likelihood as a function of the branching fraction for $B^0 \to K_S^0 \phi\gamma$. The solid line is without systematic uncertainties. The dashed line includes them.

given by

$$\int_0^{\mathcal{B}_{\rm UL}} \mathcal{L}(\mathcal{B}) d\mathcal{B} / \int_0^1 \mathcal{L}(\mathcal{B}) d\mathcal{B} = 90\%. \tag{8.9}$$

The upper limit $\mathcal{B}_{\rm UL} = 2.7 \times 10^{-6}$ corresponds to 16 signal events.

Figure 8.9 shows the efficiency-corrected ϕ-K invariant mass distributions, using the sPlot technique to isolate the signal [62]. This method uses the likelihood function to apply a weight to each event, corresponding to its probability to be signal. The solid histogram corresponds to the MC phase space model, normalized to the data histogram.

These results are consistent the Belle measurement of the charged-mode branching fraction, and set a more stringent upper limit on that of the neutral mode. This

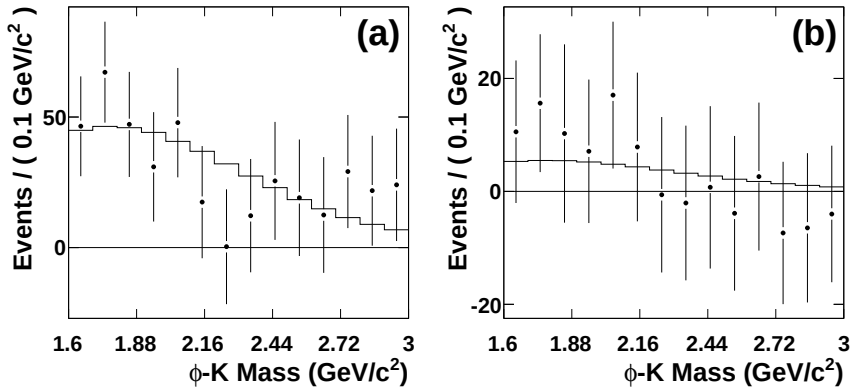

Figure 8.9: The background-subtracted and efficiency-corrected ϕ-K mass distributions (points with uncertainties) for the charged mode (a) and the neutral mode (b). The signal MC model for the mass spectrum is shown as a histogram without uncertainties and is normalized to the data histogram.

is the first measurement of the charge asymmetry of $B^+ \to K^+\phi\gamma$. The results were published in Physical Review D in 2007 [68].

Chapter 9

Conclusions

Flavor-changing neutral current decays like $b \to s\gamma$ are some of the most sensitive processes that may distinguish the standard model from alternative theories. Because they only proceed through a loop diagram at leading order, they are particularly sensitive to the content of that loop. New particles or couplings not present in the standard model could lead to discrepancies from that model. In this dissertation I have presented two measurements that probe different aspects of the $b \to s\gamma$ interaction: an examination of the photon polarization through its effects on time-dependent *CP* violation in $B^0 \to K_S^0\pi^0\gamma$, and measurements of the $B \to K\phi\gamma$ branching fraction and charge asymmetry.

Time-dependent *CP* violation in $B^0 \to K_S^0\pi^0\gamma$ decays provides a tool to study the photon polarization. Because the standard model predicts highly-polarized photons, very little *CP* violation due to interference between B mixing and decay is expected ($|S| \lesssim 0.1$). The time-integrated *CP* asymmetry C is also expected to be small, less than 1% in the standard model. In this work, using the final *BABAR*

dataset of 467×10^6 $B\overline{B}$ decays, we found

$$S_{K^*\gamma} = -0.03 \pm 0.29 \text{ (stat)} \pm 0.03 \text{ (syst)},$$

$$C_{K^*\gamma} = -0.14 \pm 0.16 \text{ (stat)} \pm 0.03 \text{ (syst)},$$

$$S_{K^0_S\pi^0\gamma} = -0.78 \pm 0.59 \text{ (stat)} \pm 0.09 \text{ (syst)},$$

$$C_{K^0_S\pi^0\gamma} = -0.36 \pm 0.33 \text{ (stat)} \pm 0.04 \text{ (syst)}.$$

These results are consistent with the standard model expectations, within the experimental uncertainties. They are more precise than *BABAR*'s previous measurements and the corresponding analysis by the Belle collaboration, which uses 535×10^6 $B\overline{B}$ decays [55]. The *BABAR* and Belle measurements are in good agreement.

A super B factory [69] would make significant progress toward a precision test of the standard model in this mode. A factor of 100 times more data would reduce the statistical uncertainties down to the level of the standard model asymmetry, which is also about equal to the systematic uncertainties. To reduce the systematic effects, the alignment of the vertex detector must be precisely characterized, the Δt model must be well-determined, and the B backgrounds must be better understood. The significant increase in luminosity would help to mitigate these challenges.

A related process, $B \to K\phi\gamma$, was also studied in this work. The branching fractions of $B^+ \to K^+\phi\gamma$ and $B^0 \to K^0\pi^0\gamma$ were measured with 228×10^6 $B\overline{B}$ decays in *BABAR* data:

$$\mathcal{B}(B^+ \to K^+\phi\gamma) = (3.5 \pm 0.6 \text{ (stat)} \pm 0.4 \text{ (syst)}) \times 10^{-6}$$

$$\mathcal{B}(B^0 \to K^0\phi\gamma) = (1.3 \pm 1.0 \text{ (stat)} \pm 0.3 \text{ (syst)}) \times 10^{-6}.$$

A significant signal was not observed in the B^0 mode, so an upper limit was set:

$$\mathcal{B}(B^0 \to K^0\phi\gamma) < 2.7 \times 10^{-6},$$

at 90% confidence. The branching fraction of the charged B decay is consistent with an earlier measurement by the Belle collaboration based on 96×10^6 $B\overline{B}$ decays [64]. The *BABAR* limit on the neutral-mode branching fraction is lower than the limit obtained in the Belle analysis. I have also presented the first measurement of the rate asymmetry between B^+ and B^- decays to the $K^\pm\phi\gamma$ final state,

$$A_{CP} = (-26 \pm 14\ (\text{stat}) \pm 5\ (\text{syst}))\%.$$

This is consistent with the standard model expectation of $|A_{CP}| < 1\%$.

These measurements constitute a step toward further studies of the $B \to K\phi\gamma$ process. Once the neutral mode is established, a study of time-dependent *CP* violation in $B^0 \to K^0_S\phi\gamma$ decays will give another window to the photon polarization and possible new *CP*-violating phases. The $\phi \to K^+K^-$ decay pinpoints the B^0 decay vertex, making this mode experimentally easier than $B^0 \to K^0_S\pi^0\gamma$. However, to be feasible, $\mathcal{O}(100)$ signal events are necessary, requiring at least $2\,\text{ab}^{-1}$ of data. Both the charged and neutral modes can be used in a study of angular distributions of the decay products as another tool to probe the photon polarization [21, 22]. The angular studies require on the order of hundreds of signal events, which could become feasible for the charged mode at a B factory with a data sample of $\mathcal{O}(1\,\text{ab}^{-1})$. Both the angular and time-dependent measurements are well within reach of a super B factory, which would produce on the order of 100 times more data than the current generation of B factories.

Although there is currently no evidence of physics beyond the standard model based on this work, statistical uncertainties remain the limiting factor in measurements of $b \to s\gamma$ decays. Continued study of these decay modes will provide important cross-checks on new phenomena that may be found at the Large Hadron Collider or elsewhere.

Bibliography

[1] T. Aoyama, M. Hayakawa, T. Kinoshita, and M. Nio, Phys. Rev. Lett. **99**, 110406 (2007).

[2] D. Hanneke, S. Fogwell, and G. Gabrielse, Phys. Rev. Lett. **100**, 120801 (2008).

[3] S. L. Glashow, Nucl. Phys. **22**, 579 (1961).

[4] S. Weinberg, Phys. Rev. Lett. **19**, 1264 (1967).

[5] A. Salam, Originally printed in Svartholm: Elementary Particle Theory, Proceedings Of The Nobel Symposium Held 1968 At Lerum, Sweden, Stockholm 1968, 367-377.

[6] P. W. Higgs, Phys. Rev. Lett. **13**, 508 (1964).

[7] Particle Data Group, W. M. Yao *et al.*, J. Phys. G **33**, 1 (2006).

[8] N. Cabibbo, Phys. Rev. Lett. **10**, 531 (1963).

[9] M. Kobayashi and T. Maskawa, Prog. Theor. Phys. **49**, 652 (1973).

[10] L. Wolfenstein, Phys. Rev. Lett. **51**, 1945 (1983).

[11] B. Grinstein, R. P. Springer, and M. B. Wise, Phys. Lett. B **202**, 138 (1988).

[12] G. Buchalla, A. J. Buras, and M. E. Lautenbacher, Rev. Mod. Phys. **68**, 1125 (1996).

[13] M. Misiak *et al.*, Phys. Rev. Lett. **98**, 022002 (2007).

[14] Heavy Flavor Averaging Group (HFAG), E. Barberio *et al.*, (2007), arXiv:0704.3575[hep-ex].

[15] J. M. Soares, Nucl. Phys. B **367**, 575 (1991).

[16] K. Kiers, A. Soni, and G. H. Wu, Phys. Rev. D **62**, 116004 (2000).

[17] A. Ali and A. Y. Parkhomenko, Eur. Phys. J. C **23**, 89 (2002).

[18] M. Beneke, T. Feldmann, and D. Seidel, Nucl. Phys. B **612**, 25 (2001).

[19] S. W. Bosch and G. Buchalla, Nucl. Phys. B **621**, 459 (2002).

[20] Y. Y. Keum, M. Matsumori, and A. I. Sanda, Phys. Rev. D **72**, 014013 (2005).

[21] D. Atwood, T. Gershon, M. Hazumi, and A. Soni, (2007), hep-ph/0701021.

[22] V. D. Orlovsky and V. I. Shevchenko, Phys. Rev. D **77**, 093003 (2008).

[23] D. Atwood, M. Gronau, and A. Soni, Phys. Rev. Lett. **79**, 185 (1997).

[24] M. Matsumori and A. I. Sanda, Phys. Rev. D **73**, 114022 (2006).

[25] B. Grinstein, Y. Grossman, Z. Ligeti, and D. Pirjol, Phys. Rev. D **71**, 011504 (2005).

[26] B. Grinstein and D. Pirjol, Phys. Rev. D **73**, 014013 (2006).

[27] P. Ball and R. Zwicky, Phys. Lett. B **642**, 478 (2006).

[28] M. A. Shifman, A. I. Vainshtein, and V. I. Zakharov, Nucl. Phys. B **147**, 448 (1979).

[29] R. N. Mohapatra and J. C. Pati, Phys. Rev. D **11**, 566 (1975).

[30] R. N. Mohapatra and J. C. Pati, Phys. Rev. D **11**, 2558 (1975).

[31] G. Senjanovic and R. N. Mohapatra, Phys. Rev. D **12**, 1502 (1975).

[32] G. Senjanovic, Nucl. Phys. B **153**, 334 (1979).

[33] J. C. Pati and A. Salam, Phys. Rev. D **10**, 275 (1974).

[34] D. Cocolicchio, G. Costa, G. L. Fogli, J. H. Kim, and A. Masiero, Phys. Rev. D **40**, 1477 (1989).

[35] G. M. Asatryan and A. N. Ioannisyan, Sov. J. Nucl. Phys. **51**, 858 (1990).

[36] K. Fujikawa and A. Yamada, Phys. Rev. D **49**, 5890 (1994).

[37] K. S. Babu, K. Fujikawa, and A. Yamada, Phys. Lett. B **333**, 196 (1994).

[38] P. L. Cho and M. Misiak, Phys. Rev. D **49**, 5894 (1994).

[39] CLEO Collaboration, R. Ammar *et al.*, Phys. Rev. Lett. **71**, 674 (1993).

[40] G. Beall, M. Bander, and A. Soni, Phys. Rev. Lett. **48**, 848 (1982).

[41] L. Wolfenstein, Phys. Rev. D **29**, 2130 (1984).

[42] C.-K. Chua, X.-G. He, and W.-S. Hou, Phys. Rev. D **60**, 014003 (1999).

[43] *BABAR* Collaboration, B. Aubert *et al.*, Nucl. Instrum. Meth. A **479**, 1 (2002).

[44] P. Billoir, Nucl. Instrum. Meth. A **225**, 352 (1984).

[45] D. N. Brown *et al.*, *BABAR* Analysis Document #1628 (2007).

[46] *BABAR* Collaboration, B. Aubert *et al.*, Phys. Rev. Lett. **99**, 021603 (2007).

[47] *BABAR* Collaboration, B. Aubert *et al.*, Phys. Rev. D **67**, 032002 (2003).

[48] G. C. Fox and S. Wolfram, Phys. Rev. Lett. **41**, 1581 (1978).

[49] D. J. Lange, Nucl. Instrum. Meth. A **462**, 152 (2001).

[50] GEANT4 Collaboration, S. Agostinelli *et al.*, Nucl. Instrum. Meth. A **506**, 250 (2003).

[51] W. D. Hulsbergen, Nucl. Instrum. Meth. A **552**, 566 (2005).

[52] *BABAR* Collaboration, B. Aubert *et al.*, Phys. Rev. Lett. **93**, 131805 (2004).

[53] *BABAR* Collaboration, B. Aubert *et al.*, Phys. Rev. Lett. **93**, 201801 (2004).

[54] *BABAR* Collaboration, B. Aubert *et al.*, Phys. Rev. D **72**, 051103 (2005).

[55] Belle Collaboration, Y. Ushiroda *et al.*, Phys. Rev. **D74**, 111104 (2006).

[56] D. Atwood, T. Gershon, M. Hazumi, and A. Soni, Phys. Rev. D **71**, 076003 (2005).

[57] A. L. Kagan and M. Neubert, Eur. Phys. J. C **7**, 5 (1999).

[58] ARGUS Collaboration, H. Albrecht *et al.*, Z. Phys. C **48**, 543 (1990).

[59] *BABAR* Collaboration, B. Aubert *et al.*, Phys. Rev. D **77**, 012003 (2008).

[60] O. Long, M. Baak, R. N. Cahn, and D. Kirkby, Phys. Rev. D **68**, 034010 (2003).

[61] *BABAR* Collaboration, B. Aubert *et al.*, Phys. Rev. Lett. **99**, 171803 (2007).

[62] M. Pivk and F. R. Le Diberder, Nucl. Instrum. Meth. A **555**, 356 (2005).

[63] *BABAR* Collaboration, B. Aubert *et al.*, Phys. Rev. D **78**, 071102 (2008).

[64] Belle Collaboration, A. Drutskoy *et al.*, Phys. Rev. Lett. **92**, 051801 (2004).

[65] *BABAR* Collaboration, B. Aubert *et al.*, Phys. Rev. D **72**, 052004 (2005).

[66] *BABAR* Collaboration, B. Aubert *et al.*, Phys. Rev. Lett. **91**, 171802 (2003).

[67] Belle Collaboration, K. F. Chen *et al.*, Phys. Rev. Lett. **94**, 221804 (2005).

[68] *BABAR* Collaboration, B. Aubert *et al.*, Phys. Rev. D **75**, 051102 (2007).

[69] M. Bona *et al.*, SLAC-R-856 (2007).